ATOM TRANSFER RADICAL POLYMERIZATION FROM PLASMACHEMICAL NANOFILMS

MORSCH, SUZANNE

ATOM TRANSFER RADICAL POLYMERIZATION FROM PLASMACHEMICAL NANOFILMS

Suzanne Morsch

Surface tethered bottle-brush co-polymers are prepared by ATRP grafting of the macroinitiator brush backbone onto plasmachemical deposited poly(vinylbenzyl chloride) initiator nanofilms, followed by ATRP growth of the side chains (bristles). Lateral force scanning probe microscopy demonstrates that poly(glycidyl methacrylate)-graft-poly(sodium 4-styrenesulfonate) bottle-brush decorated surfaces give rise to an enhancement in lubrication.

Patterned polymer brushes are fabricated using molecular scratchcard lithography, where a functional top nanolayer (acting as a resist) is selectively removed using a scanning probe tip to expose underlying ATRP initiator sites. The lateral spreading of grafted polymer brush patterns across the adjacent functional resist surface is reversibly actuated by solvent exposure.

Macroporous poly(vinylbenzyl chloride) scaffolds are used for ATRP initiation to generate polymer brushes and thereby actuate pore size. These functionalised macroporous scaffolds are fabricated by a decoupled two-step approach comprising plasmachemical deposition of the host material followed by spontaneous emulsion formation using amphiphilic species.

Finally, charge nanopatterning onto polymer film surfaces is accomplished by using an SPM probe tip to create localised corona discharge electrification. The efficacy of surface charging is shown to correlate strongly to the polymer substrate hydrophilicity. Localised plasma generation using a scanning probe microscope tip is then demonstrated to actuate the movement of ATRP surface grafted polyelectrolyte and polyzwitterionic brushes. The raising or retraction of polymer brushes can be controlled by varying the SPM tip polarity.

ATOM TRANSFER RADICAL POLYMERIZATION FROM PLASMACHEMICAL NANOFILMS

Suzanne Morsch

PhD Thesis

Department of Chemistry

Durham University

2012

TABLE OF CONTENTS

CHAPTER 2 TAILORING THE DENSITY OF SURFACE TETHERED BOTTLE-BRUSHES

CHAPTER 3 NANOPATTERNED POLYMER BRUSHES

CHAPTER 4 A COMBINED PLASMACHEMICAL AND EMULSION TEMPLATING APPROACH FOR ACTUATED MACROPOROUS SCAFFOLDS

CHAPTER 5 PART 1: NANOPLASMA SURFACE ELECTRIFICATION

DECLARATION

The work described in this thesis was carried out in the Department of Chemistry at Durham University between October 2007 and December 2011. It is the original work of the author except where otherwise acknowledged, and has not been previously submitted for a degree in this or any other university.

STATEMENT OF COPYRIGHT

LIST OF PUBLICATIONS AND PRESENTATIONS

Work in this thesis has either been presented or published or as follows:

"Surface Actuation of Smart Nanoshutters" S. Morsch, W. C. E. Schofield, J. P. S. Badyal, *Langmuir* **2010**, *26*, 12342.

"Surface Actuation of Smart Nanoshutters" Postgraduate Research Symposium presentation; Department of Chemistry, Durham University, 2011.

"Tailoring the Density of Surface-Tethered Bottlebrushes" S. Morsch, W. C. E. Schofield, J. P. S. Badyal, *Langmuir* **2011***, 27,* 14151.

"Surface Tethered Nano Bottle-Brushes" J. P. S. Badyal and S. Morsch GB Pat. Appl. No. 1112369.2 filed 19th July 2011.

"Nanoplasma Surface Electrification" S. Morsch, P. S. Brown, J. P. S. Badyal, *J. Mater. Chem.* **2012**, *22*, 3922.

"A Combined Plasmachemical and Emulsion Templating Approach for Actuated Macroporous Scaffolds" S. Morsch, T. J. Wood, W. C. E. Schofield, J. P. S. Badyal, *Adv. Funct. Mater.* **2012***, 22*, 313.

"Functional Porous Materials" J. P. S. Badyal and S. Morsch GB Pat. Appl. No. 1112404.7 filed 19th July 2011.

ACKNOWLEDGEMENTS

I would like to thank Professor J. P. S. Badyal for his support, encouragement and patience over the course of my PhD. I would also particularly like to thank Dr. Wayne Schofield for his invaluable advice throughout, and all the members of the surface science group (past and present) for their helpful input and for providing welcome amusement and distraction over the past four years. I also wish to thank Professor S. J. Biswas and members of the Nanotribology Lab at the IISc for welcoming me to their University and endeavouring to assist me in my experiments there.

Further thanks go to my friends and family for their emotional and financial support, especially Chris.

For My Parents

CHAPTER 1

SURFACE MODIFICATION AND ANALYSIS TECHNIQUES

1.1 AIMS AND SCOPE OF THESIS

Whilst plasma deposition of organic films has been well-established as a substrate-independent and solventless surface modification technique,[1] the mechanically robust nanofilms generated can be considered ill-defined at a macromolecular level. This is a consequence of molecular fragmentation occurring in the glow discharge, resulting in highly cross-linked, randomly terminated polymer chains covalently anchored to the substrate.[2,3]

In contrast, surface-initiated atom transfer radical polymerization (ATRP) is a widely adopted controlled polymerization technique that produces molecularly well-defined surface-tethered polymer brushes.[4] However, pre-treatment of substrates is generally required for immobilisation of halogen-bearing ATRP initiator species prior to polymerization. These pre-treatments frequently involve substrate-specific chemistry and can yield polymer brush layers lacking long term stability e.g., due to the detachment of underlying initiator species via oxidation.

ATRP has been initiated from plasma deposited films to effectively combine the mechanically robust nature of plasma deposited nanolayers with the inherent control over macromolecular architecture afforded by ATRP.[5] In a previous proof-of-concept study ATRP grafting onto pulsed plasma deposited poly(vinylbenzyl chloride) films was reported to result in controlled surface-confined growth of polymer brushes.[5] This methodology has the potential to modify any substrate with well-defined polymer brushes. In this thesis, its use has been extended to different monomers (e.g., polyelectrolytes) and substrate morphologies (e.g., porous scaffolds, nanopatterned regions) in a series of studies to demonstrate its widespread applicability. These include the design of graft co-polymers for biomimetic aqueous lubrication, nanolithography for the fabrication of three-dimensional structures, surface modification of porous scaffolds and generation of stimulus responsive brushes. Taken as a whole, this work was designed to demonstrate the versatility of, and comparable outcomes achievable with, plasma deposited films in comparison to more commonly used methods for ATRP initiator immobilisation, e.g., self-assembled monolayers.

1.2 ATOM TRANSFER RADICAL POLYMERIZATION (ATRP)

Polymer brushes of well-defined molecular weight offer a promising route towards the goal of tailored surface functionality, of key importance in fields such as the stabilisation of nanoparticles,[6,7] the development of stimuli responsive materials,[8,9] pore size adjustment for highly selective membranes,[10,11,12] and bioconjugation.[13,14] To this end, controlled polymerization techniques such as atom transfer radical polymerization (ATRP) offer a means to produce surface-tethered polymer brushes with predetermined, narrowly distributed molecular weights.[15,16]

1.2.1 Controlled Radical Polymerization

The well-defined chain growth achieved by controlled radical polymerization techniques is derived from a dynamic equilibrium between propagating radicals and dormant species (the persistent radical effect). During polymerization, fast and reversible deactivation of propagating radicals minimises uncontrolled chain growth and termination processes, yielding polymer brushes with narrow molecular weight distributions, Scheme 1.1.

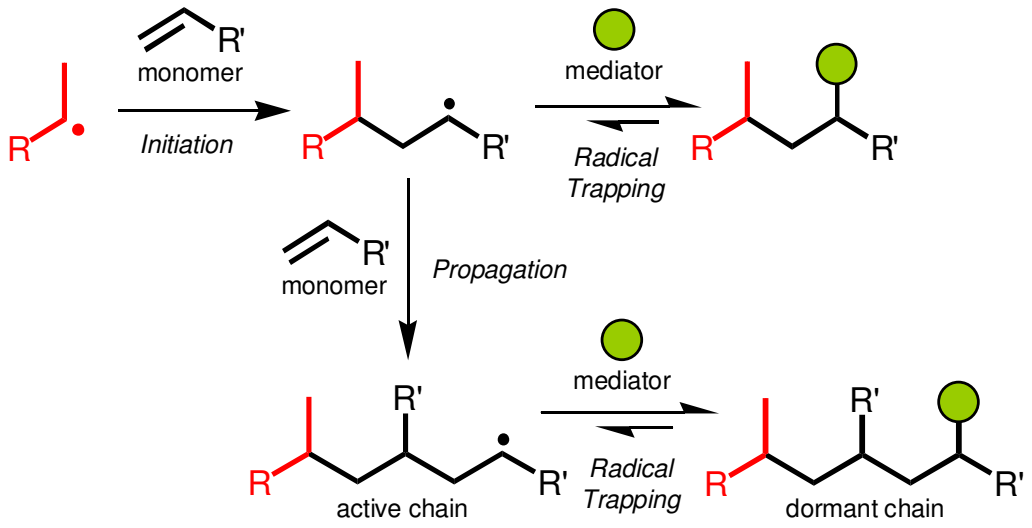

Scheme 1.1: The mechanism used to achieve the persistent radical effect in controlled/living radical polymerization.

Numerous controlled radical polymerization techniques have been developed which differ according to the radical-trapping mechanism used to achieve a dynamic equilibrium between dormant and active species.[17] One approach relies on degenerative transfer mechanisms, exploiting rapid chain transfer across an added mediating species to facilitate activation/deactivation processes. Specific examples of this methodology include reversible addition-fragmentation polymerization,[18,19,20] iodide transfer polymerization,[21] and telluride-mediated polymerization.[22] Alternative controlled radical polymerization techniques include nitroxide mediated polymerization,[23,24,25] and cobalt mediated radical polymerization.[26] For these methods, the dormant species is a stable organic radical that is activated either thermally or spontaneously in the presence of light. A prerequisite for all the aforementioned techniques is stoichiometric addition of the mediating species, because every propagating chain must be capped by a mediator following initiation with a conventional free radical initiator.

An alternative controlled radical polymerization technique, atom transfer radical polymerization (ATRP), operates through rapid halogen atom transfer between propagating polymer chain ends and a transition metal catalyst system of the general formula MLX/MLX_2, where M represents a transition metal amenable to one electron redox reactions, L are ligand(s), and X denotes the transferable halogen atom, Scheme 1.2.[27] In the case of ATRP, initiation is achieved by halide abstraction from an alkyl halide, so that sub-stoichiometric amounts of (commercially available) catalytic mediator species may be added in order to achieve control.[15,16] In addition, ATRP is particularly attractive in view of the mild reaction conditions employed and its applicability to a wide range of monomer funtionalities.[4,28]

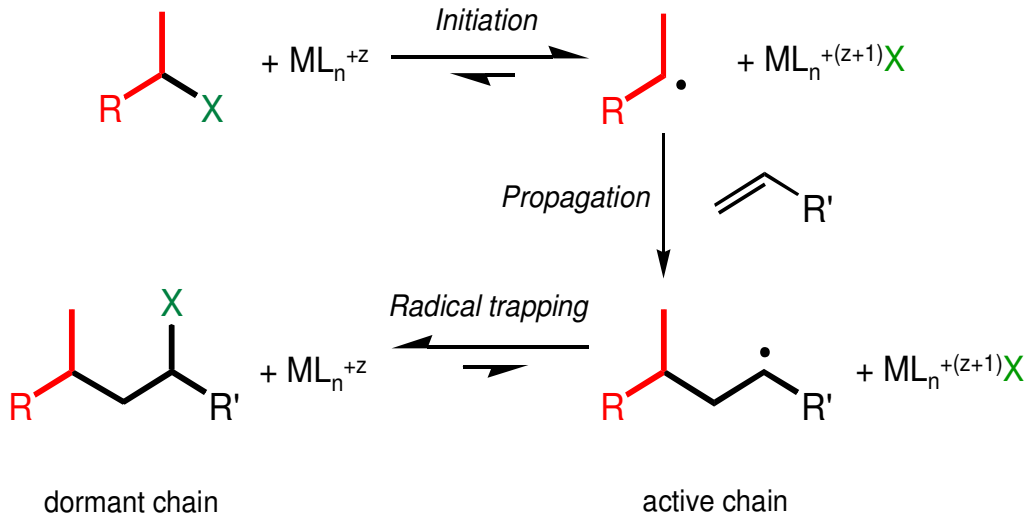

Scheme 1.2: The ATRP mechanism, where M represents a transition metal amenable to one electron redox reactions, L are ligand(s), and X denotes the transferable halogen atom. R and R' represent carboradical stabilising groups.

1.2.2 Surface Tethered Polymer Brushes

ATRP has been used to graft a diverse range of polymer brush layers (including poly(methacrylates), poly(acrylates), poly(styrene) derivatives, and polyelectrolytes[15,16]) onto a variety of materials including metals,[29] polymers,[30] clays,[31] cellulose,[32] glass[33] and gels.[34] Common approaches adopted for modifying surfaces with ATRP polymer brushes consist of either "grafting to" (where pre-formed polymer brushes are coupled to a substrate) or "grafting from" (where polymerization is initiated from surface sites). For the former case, grafting densities (and thus film thicknesses achievable) are necessarily limited by steric considerations accompanying polymer attachment.[15] In contrast, the alternative of grafting from initiator sites can readily produce densely packed polymer chains covalently tethered to the substrate.[35]

For surface initiated ATRP, the prerequisite is a surface bound species bearing a transferable halogen atom to facilitate initiation of polymerization. This has most commonly been accomplished using self assembled monolayers (SAMs) of thiol or silane molecules attached to gold or silicon substrates respectively.[36,37,38,39] However, there are inherent disadvantages associated with SAMs which include long term instability towards oxidation in

the case of thiol-gold systems,[40] moisture sensitivity of silanes,[41,42,43] and the need for multiple step initiator syntheses. Alternative approaches have encompassed electrografting,[44,45] spin coating,[46] plasma modification,[47,48] electrochemical reduction,[49,50] Langmuir-Blodgett films,[51] co-polymerization with halogen containing monomers,[52] wet chemical conversion of surface functional groups,[53,54,55] and UV induced coupling.[56,57] For all of these cases, generation of the initiator site depends on substrate-specific chemistries requiring multiple reaction steps. These drawbacks can potentially be overcome by using pulsed plasmachemical deposition of ATRP initiating nanolayers. The combination of pulsed plasmachemical deposition and surface initiated ATRP circumvents any issues relating to substrate specificity, and therefore has potential for precise functionalisation of any substrate with polymer brushes.[5]

1.3 PULSED PLASMACHEMICAL DEPOSITION

Pulsed plasmachemical deposition entails the fabrication of well-defined polymeric coatings from the plasma state of an organic precursor. This represents a single-step, substrate-independent and solventless surface modification technique.[1] Furthermore, deposited film thicknesses can be confined to the nanometre regime, and surface functional group density tuned by careful selection of plasma deposition parameters.

1.3.1 Plasma Forms

The plasma state refers to ionised gas; it is a pseudo stable state of matter consisting of gaseous ions, electrons, and neutral species in ground and excited states, with a net space charge of zero. The charged species within plasma impart electrical conductivity, giving rise to the collective behaviour by which plasma is defined; a response to externally applied electromagnetic fields.[58]

Plasma forms are sub-categorised by temperature, and this dictates the degree of ionisation. Thermal or ‘natural’ plasma is produced under conditions of intense heat, which facilitates the ionisation of molecules and atoms within a gas. Stars, lightning and fusion plasmas are examples of

thermal plasma, in which all species (neutrals, ions and electrons) are in thermal equilibrium.[64] Non-equilibrium plasma (commonly referred to as 'cold' plasma) is characterised by a lower degree of ionisation, where electron temperature exceeds that of the surrounding ions and neutral species, which remain close to the ambient.[58] The extensive use of cold plasma for surface modification encompasses plasma etching,[59] surface activation,[60] and plasmachemical deposition.[61]

1.3.2 Non-Equilibrium Plasma Discharge

This widespread use of cold plasma is due, in part, to its straightforward generation in the laboratory, achieved by the application of an electric field to low pressure gas.[2,3,62,64] Plasma ignition occurs as a result of the acceleration (and the subsequent collisions) of a finite number of free electrons by the externally applied electric field (free electrons are ubiquitous, being generated by natural ionisation sources such as cosmic rays and background radioactivity).[63,64] Electrons gaining sufficient kinetic energy through acceleration undergo inelastic collisions with surrounding gaseous atoms or molecules, resulting in the formation of ions or excited species. Ionisation occurs when the energy transferred during a collision exceeds the ionisation energy of the species, whereas collisions imparting insufficient energy for ionisation produce metastable states. These metastable states may, in turn, relax via luminescence or undergo further collisions, during which they may be ionised more easily than the corresponding ground state, or else induce ionisation in a different atom or molecule (the Penning effect),[64] Scheme 1.3. At the breakdown voltage, a cascade of secondary electrons is produced by predominantly ionising collisions, and the resulting electric multiplication maintains the plasma discharge.

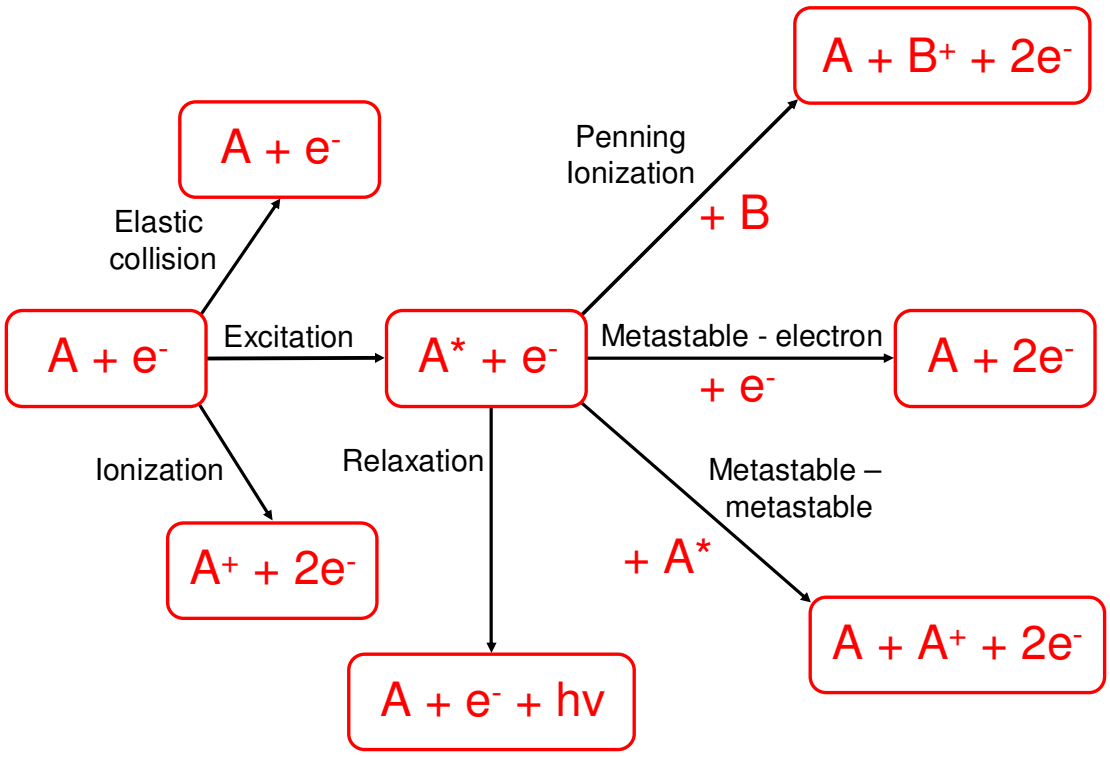

Scheme 1.3: The processes resulting in the formation of radicals, ions and excited species during plasma discharge, following the collision of A, (representing a gaseous atom or molecular species) and e^- (an accelerated electron).

1.3.3 Plasmachemical Deposition

Plasma discharge from organic precursor vapour generates a range of chemically reactive species (radicals, ions, electrons, and excited species), which contribute to the deposition of an organic thin film onto any surface in contact with the plasma. Plasma deposition therefore provides a means for surface modification of materials without affecting bulk properties,[64] and has previously been exploited to manipulate interfacial properties such as wettability,[65,66,67] protein resistance,[68,69,70] adhesion,[71,72] and biocompatibility.[73,74,75] Furthermore, the technique ensures covalent bonding to the substrate via surface free radical sites created by the electrical discharge, generating mechanically robust films.

Yasuda identified that plasmachemical deposition of organic thin films can occur via two mechanisms, namely plasma-state polymerization and plasma-induced polymerization.[64] The former (plasma-state polymerization)

involves the aforementioned plasma species (radicals, ions, excited species, atoms and molecules) which react and contribute to film formation.[2,64] The latter (plasma-induced polymerization) applies when an unsaturated polymerizable bond is present in the precursor (e.g., a vinyl group). In this instance, polymer deposition additionally proceeds in a manner mechanistically comparable to conventional radical polymerization *initiated* by the plasma. Both mechanisms are active during deposition of films from vinyl precursor plasma, and these are characterised by the loss of the carbon-carbon double bond, alongside improved retention of other functional groups (when compared to films deposited from the plasma state of their saturated analogues).

Nonetheless, plasmachemical deposited films are typified by a highly cross-linked structure, consisting of randomly terminated short and branched chains and containing a variety of functional groups.[2,3] This is because polymerizable plasma precursors (monomers) are relatively complex organic molecules which can dissociate during plasma discharge (because typical ionisation energies exceed the energy of bond dissociation).[76] Precursor fragmentation is dependent on the energy supplied to the plasma during deposition, which thereby determines the structural integrity of the generated plasmachemical thin film. The composite plasma process parameter W/FM (where W = power, F = precursor flow rate and M = precursor molecular weight) defines the energy input per unit mass of the precursor and is widely recognised as the determining factor for precursor structural retention, which is maximised at lower W/FM ratios through minimised fragmentation.[2,3,64]

1.3.4 Pulsed Plasmachemical Deposition

Modulating the plasma discharge reduces the average power input over time (W/FM ratio), and yields enhanced structural integrity within the deposited thin film.[77] Furthermore, for a given W/FM ratio, pulsed plasma discharge frequently produces further improvements in precursor structural retention when compared to continuous wave deposition. This is ascribed to an increased contribution of conventional polymerization mechanisms active during the plasma off-period.[64] Extremely high levels of surface functionality have been attained using this pulsed plasma deposition approach. Examples

successfully devised in the past include amine,[78] anhydride,[79] epoxide,[72] carboxylic acid,[80] cyano,[81] halide,[5] hydroxyl,[82] furfuryl,[83] and perfluoroalkyl[84] functionalised surfaces. Effectively, any surface that relies on a specific chemistry for its performance can, in principle, be generated by pulsed plasmachemical deposition. This includes halide functionalised films such as poly(vinylbenzyl chloride) for ATRP initiation.[5]

The characterisation of plasma-deposited films and ATRP grafted polymer brush layers must be achieved using surface specific analysis techniques, such as x-ray photoelectron spectroscopy, infrared spectroscopy, microscopy, contact angle analysis and spectrophotometry.

1.4 X-RAY PHOTOELECTRON SPECTROSCOPY (XPS)

X-ray photoelectron spectroscopy (XPS) is a highly surface sensitive technique yielding quantitative elemental analysis pertaining to the uppermost nanometres of a sample.[85,86,87]

The sensitivity of XPS derives from the elementally unique binding energies associated with electrons residing in core orbitals. X-ray photons are of sufficient energy (short wavelength) to overcome the binding energy of these core electrons, which are ejected from atoms by the photoelectric effect upon irradiation, Scheme 1.4. These ejected electrons have characteristic kinetic energies, (KE) which can be related to their binding energy (BE) using Equation 1.1.[85,86,87]

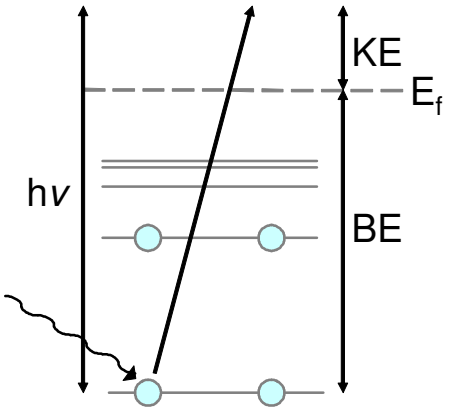

Scheme 1.4: Jablonski diagram of the ejection of an electron by the photoelectric effect.

As $h\nu = BE + KE$ (Equation 1.1)

Therefore $BE = h\nu - KE$

Where h = Planck constant

ν = the frequency of the incident radiation

BE = the binding energy of the ejected electron

KE = the kinetic energy of the ejected electron

XPS analysis yields inherently surface sensitive data as a consequence of the short inelastic mean free path of electrons (the mean distance travelled by electrons prior to losing energy to surroundings via inelastic collisions). The inelastic mean free path of electrons is weakly substrate dependent, yielding a universal curve of energy dependence. The photoelectrons generated by XPS have kinetic energies in the range of 5-2000 eV, corresponding to a mean free path length of just 5-20 Å within a solid, so that their escape depth is limited to the uppermost nanometers of the sample.[88,89]

In addition to photoelectrons, Auger electrons are also emitted following X-ray irradiation, producing characteristic peaks in the XPS spectrum. Auger emission occurs because electrons originating in higher energy levels fill the hole left in a core energy level by the emission of a photoelectron. This process releases energy, which may be dissipated by either photon emission (fluorescence) or by emission of an Auger electron, Scheme 1.5.[90]

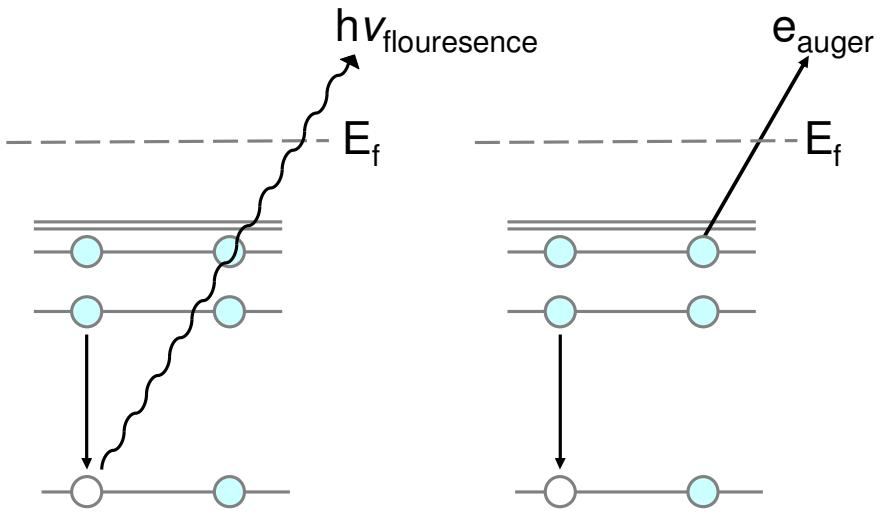

Scheme 1.5: Jablonski diagrams of fluorescence and the emission of an Auger electron following emission of a photoelectron.

XPS spectra therefore consist of intense signals corresponding to photoelectron emission and characteristic Auger electron peaks against a continuous background resulting from electron emission following inelastic collisions. Photoelectron peak intensity corresponds to the atomic cross section associated with emission, and the concentration of the element. Elemental composition is therefore calculated by measuring the area beneath photoelectron peaks, and applying instrument sensitivity factors derived from substances with known elemental composition.[85]

1.5 FOURIER TRANSFORM INFRARED SPECTROSCOPY (FTIR)

Transitions between vibrational energy levels of molecules correspond to the energy of infrared photons. Thus, the bending or stretching motions of covalent bonds that correspond to a change in dipole moment are excited by specific infrared frequencies, and produce distinctive absorption features in a spectrum. The positions of absorption bands correspond to the spring constant for the bond involved (i.e., the strength of the bond and reduced mass of vibrating atoms) and its polarity, so that infrared spectra enable the identification of functional groups.[91,92,93]

Conventional dispersive infrared spectroscopy involves sequential measurement of infrared absorption at each frequency across the spectral range (500 – 4000 cm^{-1}).[94] In Fourier transform infrared spectroscopy (FTIR) the sensitivity and rapidity of data acquisition is enhanced by simultaneous measurement of absorption across all wavelengths in the IR frequency range. The improved acquisition speed enables numerous spectra to be averaged, reducing random noise, and, in contrast to dispersive infrared spectroscopy, resolution is not limited by the use of prisms or grating required to split the infrared beam.[92,95]

FTIR operates via a Michelson inferometer with a moveable mirror, Scheme 1.6. During FTIR, light from an infrared source is split into two beams, which are then reflected by a fixed and moveable mirror. The two beams recombine and pass through the sample prior to detection, producing interference patterns dependent on the difference in path length between the two beams (i.e., the position of the movable mirror) and infrared absorption by the sample. An inferogram is obtained as a function of path length by scanning the moveable mirror, and the Fourier transform of such an inferogram yields the absorption spectrum as a function of wave number.[92,95]

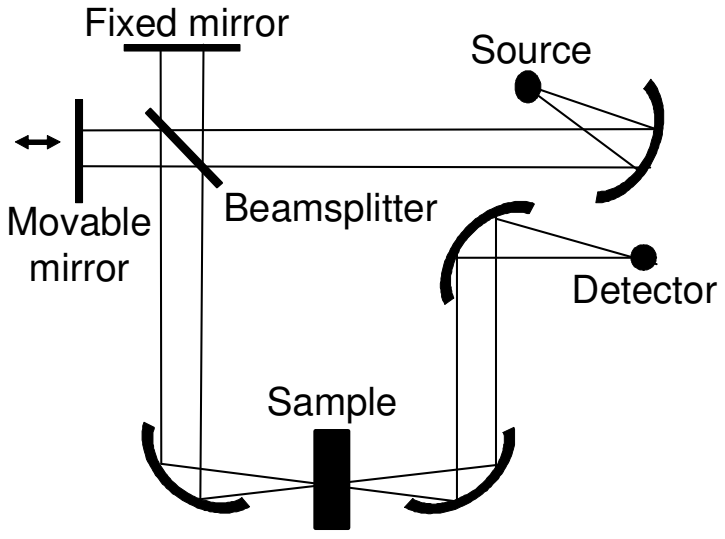

Scheme 1.6: The Michelson inferometer used in FTIR.

FTIR spectroscopy is most commonly performed in transmission mode, where the sample of interest is deposited onto an infrared-transparent potassium bromide or sodium chloride disk.[94] The infrared beam is passed

through the disk and sample, and the emergent beam differs in energy at wavelengths absorbed by molecular vibrations. Subtraction of background absorption then provides the infrared spectrum of the sample. However, in the case of surface tethered films, reaction conditions are frequently incompatible with sodium chloride or potassium bromide disk substrates. In these cases, reflection-absorption infrared spectroscopy (RAIRS) or attenuated total reflection infrared (ATR-IR) are more practicable techniques.

Sample preparation for RAIRS involves deposition of a thin film onto an underlying reflective substrate such as silicon or gold. The infrared beam (I_o) is directed towards the sample at a grazing angle, and a fraction is reflected from the interface (I_R), whilst the remainder is transmitted through the thin film (I_T), and then reflected from the underlying substrate surface, Scheme 1.7. Having passed twice through the deposited material, (thus increasing the path length and signal in comparison to transmission mode) the emergent beam (I_A) differs in energy at wavelengths absorbed by molecular vibrations within the film. Subtraction of the bare substrate spectrum yields the infrared spectrum of the thin film.

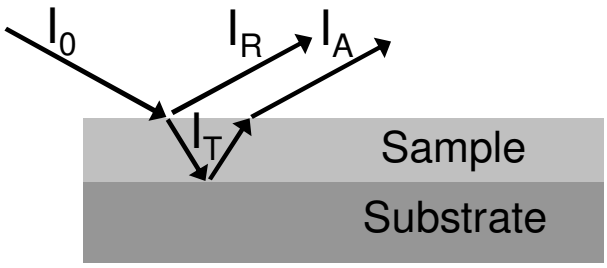

Scheme 1.7: Specular reflectance of the FTIR beam incidental upon a thin film deposited on a reflective substance.

Alternatively, for polymer layers too thick or strongly absorbing for analysis using RAIRS, attenuated total reflection infrared (ATR-IR) spectroscopy is applicable. During ATR-IR, the sample is pressed into intimate contact with an infrared transparent crystal of high refractive index

(e.g., KRS-5 or diamond). Due to the large difference between the refractive index of the crystal and the sample, IR radiation entering the crystal is completely reflected at the crystal–substrate boundary and propagates through the crystal, creating a standing wave at the crystal-substrate interface, Scheme 1.8. Absorption occurs because this standing wave penetrates into the sample to a depth dependent upon incident wavelength (typically of the order of 2.5 to 25 μm in the mid IR). Subtraction of background absorbances (of the crystal in air) from those of the emergent beam (I_A) generates the sample IR spectrum.[62,96,97,98]

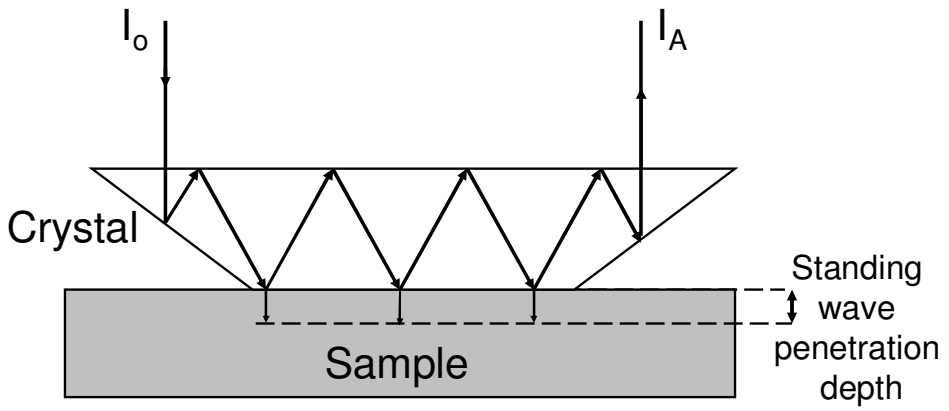

Scheme 1.8: Total internal reflection of the FTIR beam (I_o) within the ATR crystal, and the resultant standing wave penetrating the sample.

1.6 ATOMIC FORCE MICROSCOPY (AFM)

The atomic force microscope (AFM) is a powerful analytical tool capable of producing topographical images with atomic resolution,[99] and providing information about adhesive,[100] electrostatic,[101] magnetic,[102] and tribological properties.[103]

AFM measurements are performed using a probe that comprises a flexible cantilever supporting a sharp tip (< 50 nm radius of curvature). Analysis entails bringing the probe into close proximity to a sample, whereupon intermolecular forces between the tip and the sample surface result in cantilever deflection. This is detected using optical interferometry,[104] capacitive sensing,[105] or most commonly, a laser spot reflected from the top surface of the cantilever into a segmented photodiode.[106] Since

intermolecular forces are distance dependent, the force acting upon the probe (and thus the degree of cantilever deflection), varies with tip-to-sample separation. For image acquisition, a predetermined tip-to-sample distance (i.e., cantilever deflection) is maintained via a feedback mechanism whereby the underlying sample position is precisely controlled by piezoelectric elements (which facilitate movements in the xyz planes), whilst the probe is simultaneously scanned in a raster pattern across the surface. The piezoelectric z signal required to adjust sample height at each point is plotted in order to produce a topographical image, Scheme 1.9.[107,108]

AFM has been utilised in a plethora of surface studies with substrates including conductors,[109] organic thin films,[110] biomaterials,[111] polymers,[112] and ceramics.[113] Various operational modes have been developed which can be selected according to the sample and properties being examined.

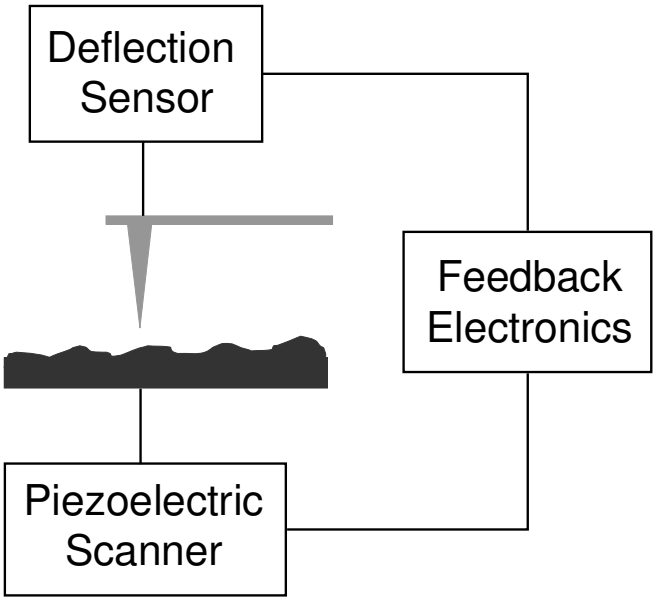

Scheme 1.9: The components of the atomic force microscope used to control and detect tip-to-sample distance.

1.6.1 Contact Mode

As the AFM probe approaches a substrate surface, the nature of intermolecular forces acting upon the tip varies from attractive to repulsive with decreasing tip-to-sample distance,[114] Scheme 1.10. During contact mode imaging, the tip-to-sample separation is selected and maintained so that hard sphere repulsion forces act upon the probe tip, and deflection of the cantilever is directly proportional to changes in surface height.[115] Limitations of contact mode imaging stem from the applied force required to bring the tip and sample into the repulsive regime, which is sufficient to deform and damage soft substrates such as biological samples and polymers.[116,117]

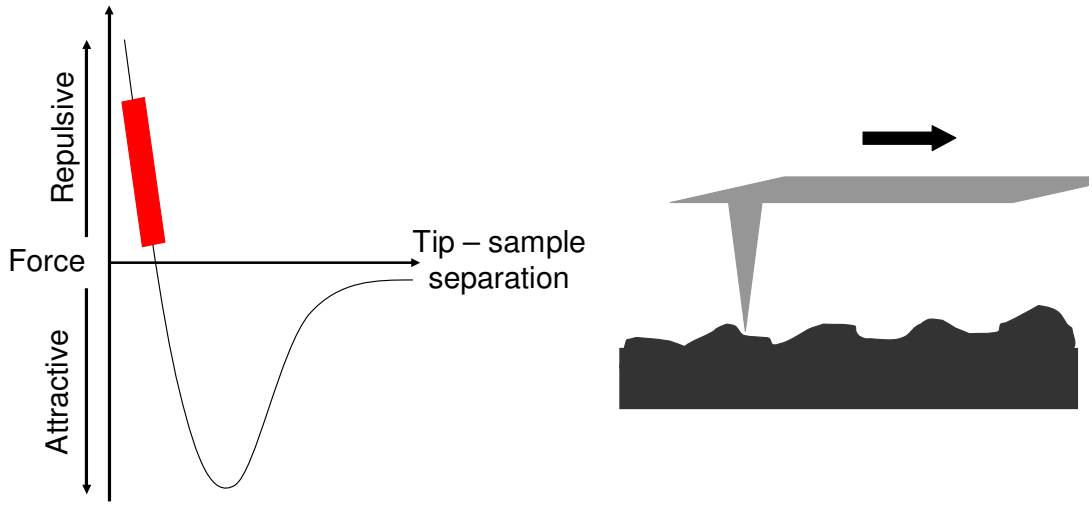

Scheme 1.10: Forces acting upon the AFM probe tip as a function of tip-to-sample separation (left) and probe movement over the substrate surface (right). The repulsive forces active during contact mode are highlighted.

1.6.2 Non-contact Mode

In non-contact mode, a tip-to-substrate separation is maintained such that only weakly attractive intermolecular forces (Van der Waals, dipole-dipole) are active upon the probe, Scheme 1.11. In order to increase sensitivity towards such weak forces, a transducer drives the probe to vibrate slightly above its resonance frequency, and the amplitude of the oscillating probe is determined from the periodic cantilever deflection.[108] As the tip approaches a sample, attractive forces reduce the effective spring constant of the probe,

thereby lowering the frequency of vibration.[114] A set point *frequency* is thus selected and maintained so that the tip is held above the surface in the attractive regime. Whilst damage to soft samples is eliminated during non-contact mode operation, the adsorption of water and gas molecules frequently result in the formation of a meniscus between the tip and surface, which can dampen probe oscillation and result in a dragging force opposing tip motion, generating imaging artefacts.[118]

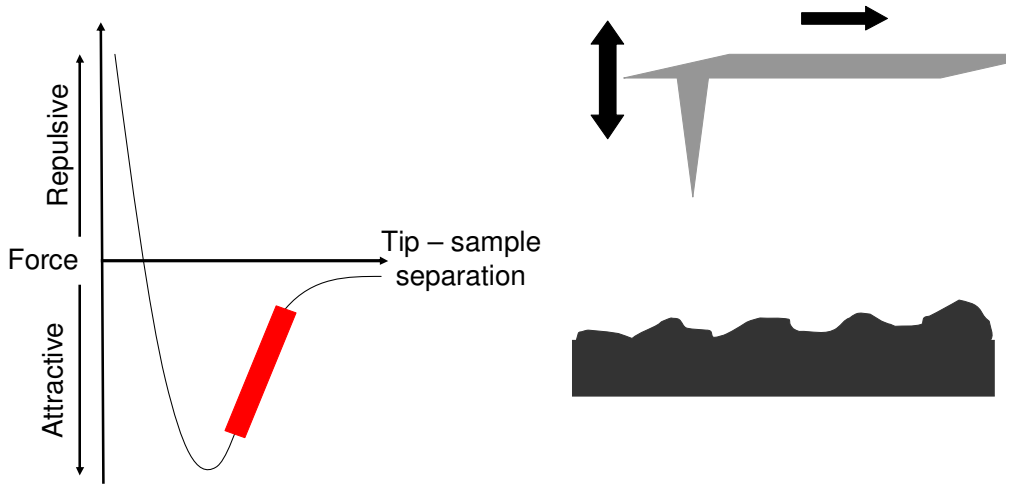

Scheme 1.11: Forces acting upon the AFM probe as a function of probe tip-to-sample separation (left) and probe movement over the substrate surface (right). The attractive forces active during non-contact mode are highlighted.

1.6.3 Intermittent Contact (Tapping) Mode

Intermittent contact (tapping) mode operation of the AFM also involves oscillation of the AFM probe close to its resonance frequency. In this case, the amplitude of oscillation (the spring constant of the probe) is selected to drive the probe tip alternately between the long range attractive and short range repulsive interaction regimes with the surface (it 'taps' the surface), Scheme 1.12. Each contact with the surface results in a loss of energy, thereby dampening tip oscillation in comparison to the free amplitude in air. In contrast to non-contact mode, the amplitude of tip oscillation is sufficient to overcome adhesive forces at the surface and, furthermore, less force is

imparted in comparison to contact mode, enabling the examination of soft samples without deformation.[117,119]

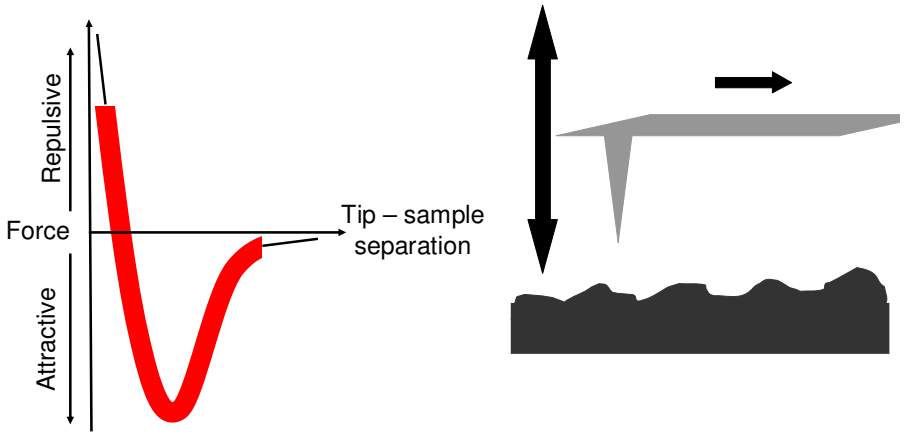

Scheme 1.12: Forces acting upon the AFM probe as a function of probe tip-to-sample separation with attractive and repulsive forces active during intermittent contact mode highlighted (left) and probe movement over the substrate surface (right).

1.6.4 Phase Imaging

Phase imaging detects the phase lag of cantilever oscillation relative to the signal sent to the transducer, and is sensitive to material properties such as friction and static charge on the surface.[120] Phase imaging is frequently carried out in conjunction with intermittent contact mode to provide complementary information about the forces acting upon the probe.

1.7 FLUORESCENCE MICROSCOPY

Examination of materials by fluorescence microscopy is ordinarily achieved following the attachment of a fluorophore to impart photoluminescent properties and yield microscale topographic or sub-surface images. Since fluorophores frequently exhibit highly specific binding chemistry, fluorescence microscopy also provides a means to distinguish between regions of differing chemical reactivity.[121]

Photoluminescence occurs following molecular absorption of photons with excitation energy corresponding to the formation of metastable excited

states. The subsequent relaxation of these metastable states is accompanied by the emission of photons. Specifically, fluorescence occurs following excitation from the ground singlet state, $S_{0,}$ to a vibrational sublevel of the excited singlet state S_1. Non - radiative decay brings the material down to the lowest vibrational sublevel of the excited state, followed by energy loss back to the ground state S_0, which results in photon emission ($h\nu_b$) of lower energy than the excitation radiation ($h\nu_a$),[122] Scheme 1.13.

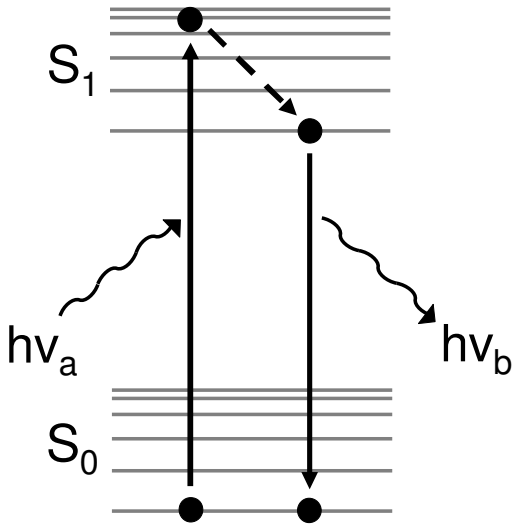

Scheme 1.13: Jablonski diagram for fluorescence; S_0 and S_1 are ground and excited singlet states respectively, hv_a a photon of the excitation wavelength, and hv_b a photon at the emission wavelength.

For fluorescence microscopy, the sample is irradiated using a wavelength corresponding to the absorption maximum of the fluorophore or material (hv_a), while the emitted wavelength (hv_b) is recorded. This involves passing excitation light (from a lamp, laser or light emitting diode) through an excitation filter to select the appropriate excitation wavelength, and focusing on the sample. The emitted light is recorded using nearby optics and focused through a second filter to remove unwanted wavelengths. Finally the signal is focused onto a photodetector which processes the signal to produce a spatial distribution map of fluorescence intensity.[123]

1.8 SCANNING ELECTRON MICROSCOPY (SEM)

Scanning electron microscopy (SEM) can provide topographical images of high resolution (1 - 5 nm) and depth of field. SEM operates using a beam of high energy electrons (0.5 - 40 keV) focused onto the sample surface. The electrons impart sufficient energy to overcome the ionisation potential of surface atoms, instigating the emission of secondary electrons from core orbitals. These secondary electrons are of a much lower energy (typically < 50 eV) than those comprising the incident beam. Acceleration and collection of secondary electrons is achieved via a positively biased grid held in close proximity to the sample surface. The high resolution and depth of field associated with SEM is a consequence of the small spot size (0.4 – 2 nm) of the focused electron beam, and the limited escape depth of generated secondary electrons; due to their low kinetic energy (and consequent short electron mean free path) these originate from the uppermost nanometres of the sample surface. The generated microscopy images are distribution maps of secondary electron emission, obtained as the focused electron beam is scanned in a raster pattern over the area of interest.[124]

1.9 CONTACT ANGLE ANALYSIS

Measurement of the equilibrium contact angle formed between a sessile water droplet and a solid is an exceptionally surface sensitive characterisation technique, because the wettability of a solid is dependent on both the localised surface energy and roughness. The contact angle θ is calculated by drawing a tangent at the three phase contact point, Scheme 1.14.[125,126]

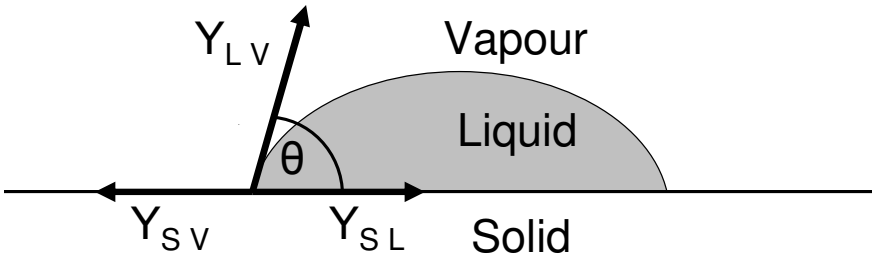

Scheme 1.14: The three phase contact point comprising the equilibrium contact angle formed by a liquid on a solid surface.

Consideration of the balanced tangential forces at the three phase contact point gives rise to Young's equation, which connects the equilibrium contact angle to the three interfacial tensions, Equation 1.2.

$$Y_{SV} = Y_{SL} + Y_{LV} \cos\theta \qquad \text{(Equation 1.2)}$$

Y_{SV}, Y_{SL} and Y_{LV} describe vectors corresponding to interfacial tension at the solid-vapour, solid-liquid and liquid-vapour interfaces respectively. Interfacial tension may be considered as the amount of energy required to form a unit area of the interface. For a given liquid, the liquid-solid and solid-vapour interfacial surface tension (and therefore the contact angle) is primarily dependent upon the functional groups present on the solid surface and its roughness (the effective contact area).[126,127]

1.10 SPECTRAL REFLECTANCE

Spectral reflectance of thin films provides a means to determine the optical constants (refractive index, absorption coefficient) and thickness of polymer films.

Whenever light crosses the interface between materials, a fraction is reflected, dependent on the incident angle of the light, and the difference between the refractive indices of the two materials.[128] When a thin film on a substrate is exposed to monochromatic light, reflection occurs from both the air/film and film/substrate interfaces, Scheme 1.15. The emergent beam's

(I_{RB}) intensity is dependent on the extinction coefficient of the thin film and combines with the beam reflected at the air-substrate interface (I_{RA}) to interfere either constructively or destructively, depending on the difference in path length which, for a given angle of incidence, is determined by both the refractive index and thickness of the film.

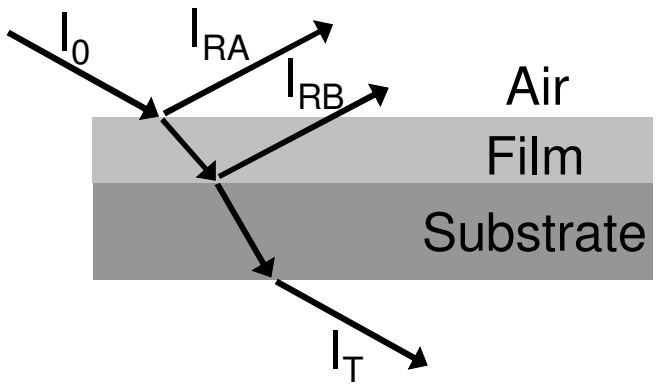

Scheme 1.15: Reflection and transmission of monochromatic incident light at air-film and film-substrate phase boundaries.

A periodically varying interference pattern can be obtained by measuring reflectance following exposure to monochromatic light through a range of wavelengths (400 – 1000 cm^{-1}), Figure 1.1.[129] This can then be fitted using a Cauchy dispersion model for the optical constants (refractive indices and extinction coefficients) to yield the film thickness.[130]

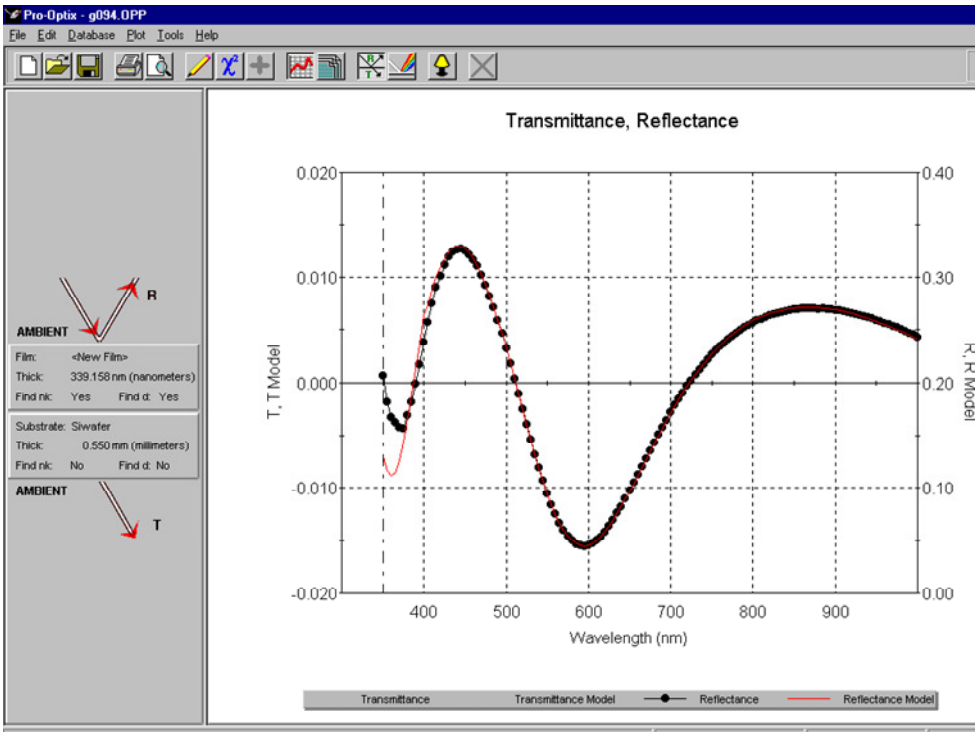

Figure 1.1: Reflectance interference pattern generated by 339 nm thick poly(methyl methacrylate) film on silicon wafer (black) and the model generated by the fitting procedure (red).

The Cauchy equation describes how refractive index varies as a function of wavelength over the visible range, and is commonly used in spectroscopic ellipsometry of organic thin films.[131] It takes the general form of Equation 1.3.

$$n(\lambda) = A + B/\lambda^2 + C/\lambda^4 \qquad \text{(Equation 1.3)}$$

In the case of spectral reflectance, a model interference pattern can be generated by the instrument software according to the Cauchy model, using initial estimated values for film thickness, Cauchy constants A and B of the refractive index, and the extinction coefficient, k. For a thin film of unknown optical constants, values of 1.5, 0.02, 0.01 are ordinarily entered as starting points for A, B and the extinction coefficient respectively (i.e., the extinction coefficient is assumed to be very low for dielectric thin films). A Levenberg-Marquardt algorithm is used to rapidly generate and compare model data to the interference pattern generated by the thin film, and fit the parameters

(thickness and optical constants) using a least squares method. Figure 1.1 shows the spectral reflectance interference pattern (black) and best fit (red) generated for 339 nm poly(methyl methacrylate) on silicon wafer. Figure 1.2 shows the calculated variation of refractive index (n, blue) and extinction coefficient (k, black) over spectral range used to generate that fit. Whilst instrument software performs the fitting procedure, user expertise is required to ensure that the values generated are reasonable.

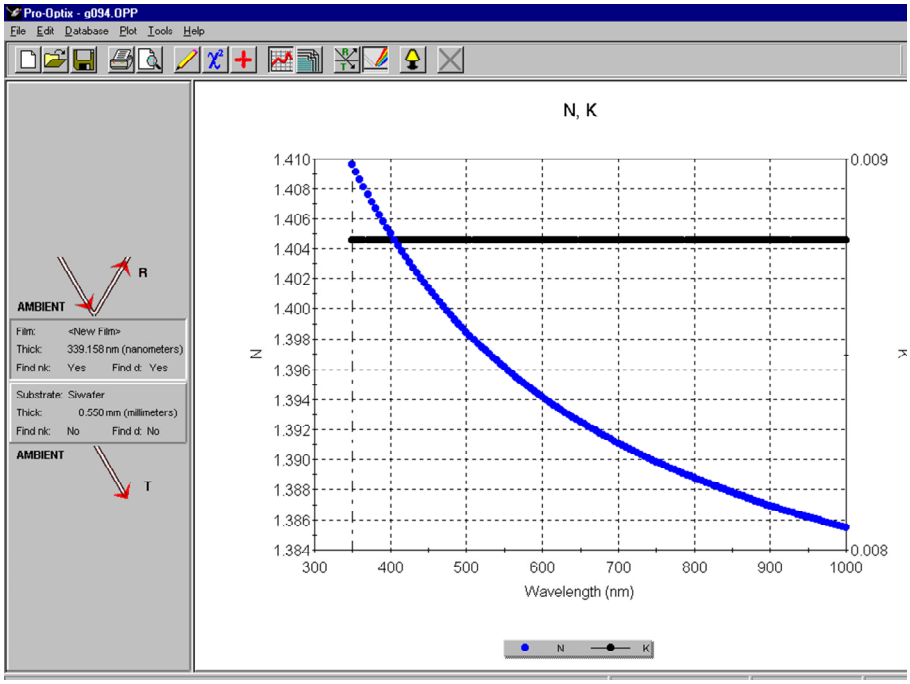

Figure 1.2: Variation of refractive index (n, blue) and absorption coefficient (k, black) fitted to the data shown in Figure 1.1.

Spectral reflectance cannot be used to accurately measure film thicknesses of less than 10 nm (because there is not enough of an oscillation in the generated data to fit). For the work described in this thesis however, spectral reflectance is only applied to thicker polymer films because ATRP is performed from pulsed plasma deposited poly(vinylbenzyl chloride) layers throughout (typically 50-100 nm thick), and the resulting polymer layers are treated as one film during the fitting procedure. The ATRP grafting rates reported therefore correspond to *increases* in the total film thickness as a function of grafting time.

1.11 REFERENCES

(1) Badyal, J. P. S. *Chem. Br.* **2001**, *37*, 45.

(2) Shi, F. F. *Surf. Coat. Technol*. **1996**, *82*, 1.

(3) Johnston E. E.; Ratner, B. D. *J. Electron Spectrosc. Relat. Phenom.* **1996**, *81*, 303.

(4) Pyun, J.; Kowalewski, T.; Matyjaszewski, K. *Macromol. Rapid Commun*. **2003**, *24*, 1043.

(5) Teare, D. O. H.; Barwick, D. C.; Schofield, W. C. E.; Garrod, R. P.; Ward, L. J.; Badyal, J. P. S. *Langmuir* **2005**, *21*, 11425.

(6) Lattuada, M.; Hatton, T. A. *Langmuir* **2007**, *23*, 2158.

(7) Fan, Q.-L.; Neoh, K.-G.; Kang, E.-T.; Shuter, B.; Wang, S. C. *Biomaterials* **2007**, *28*, 5426.

(8) Cui, Y.; Tao, C.; Zheng, S.; He, Q.; Ai, S.; Li, J. *Macromol. Rapid Commun.* **2005**, *26*, 1552.

(9) Xu, F. J.; Zhong, S. P.; Yung, L. Y. L.; Kang, E. T.; Neoh, K. G. *Biomacromolecules* **2004**, *5*, 2392.

(10) Ejaz, M.; Tsujii, Y.; Fukuda, T. *Polymer* **2001**, *42*, 6811.

(11) Friebe, A.; Ulbricht, M. *Langmuir* **2007**, *23*, 10316.

(12) Schepelina, O.; Zharov, I. *Langmuir* **2006**, *22*, 10523.

(13) Robinson, K. L.; de Paz-Banez, M. V.; Wang, X. S.; Armes, S. P. *Macromolecules* **2001**, *34*, 5799.

(14) Lee, B. S.; Lee, J. K.; Kim, W.-J.; Jung, Y. H.; Sim, S. J.; Lee, J.; Choi, I. S. *Biomacromolecules* **2007**, *8*, 744.

(15) Edmondson, S.; Osborne, V. L.; Huck, W. T. S. *Chem. Soc. Rev.* **2004**, *33*, 14.

(16) Bontempo, D.; Tirelli, N.; Feldman, K.; Masci, G.; Crescenzi, V.; Hubbell, J. A. *Adv. Mater.* **2002**, *14*, 1239.

(17) Odian, G. G. *Principles of Polymerization*, John Wiley & Sons: New York, 2004.

(18) Chong, Y. K.; Krstina, J.; Le, T. P. T.; Moad, G.; Postma, A.; Rizzardo, E.; Thang, S. H. *Macromolecules* **2003**, *36*, 2256.

(19) Mayadunne, R. T. A.; Rizzardo, E.; Chiefari, J.; Chong, Y. K.; Moad, G.; Thang, S. H. *Macromolecules* **1999**, *32*, 6977.

(20) Schilli, C. M.; Zhang, M.; Rizzardo, E.; Thang, S. H.; Chong, Y. K.; Edwards, K.; Karlsson, G.; Muller, A. H. E. *Macromolecules* **2004**, *37*, 7861.

(21) Goto, A.; Ohno, K.; Fukuda, T. *Macromolecules* **1998**, *31*, 2809.

(22) Kwak, Y.; Tezuka, M.; Goto, A.; Fukuda, T.; Yamago, S. *Macromolecules* **2007**, *40*, 1881.

(23) Guillaneuf, Y.; Gigmes, D.; Marque, S. R. A.; Tordo, P.; Bertin, D. *Macromol. Chem. Phys.* **2006**, *207*, 1278.

(24) Bartholome, C.; Beyou, E.; Bourgeat-Lami, E.; Chaumont, P.; Lefebvre, F.; Zydowicz, N. *Macromolecules* **2005**, *38,* 1099.

(25) Enright, T. E.; Cunningham, M. F.; Keoshkerian, B. *Macromol. Rapid Commun.* **2005**, *26*, 221.

(26) Kaneyoshi, H.; Matyjaszewski, K. *Macromolecules* **2005**, *38*, 8163.

(27) Wang, J.-S.; Matyjaszewski, K. *J. Am. Chem. Soc.* **1995**,*117*, 5614.

(28) Pyun, J.; Kowalewski, T.; Matyjaszewski, K. *Macromol. Rapid Commun*. **2003**, *24*, 1043.

(29) Kim, J.-B.; Bruening, M. L.; Baker, G. L. *J. Am. Chem. Soc.* **2000**, *122*, 7616.

(30) Li, L.; Yan, G.; Wu, J.; Yu, X.; Guo, Q.; Kang, E. *Appl. Surf. Sci.* **2008**, *254*, 7331.

(31) Yang, Y.; Wu, D.; Li, C.; Liu, L.; Cheng, X.; Zhao, H. *Polymer* **2006**, *47*, 7374.

(32) Carlmark, A.; Malmström, E. E. *Biomacromolecules* **2003**, *4*, 1740.

(33) Hamelinck, P. J.; Huck, W. T. S. *J. Mater. Chem.* **2005**, *15*, 381.

(34) Huang, X.; Wirth, M. J. *Macromolecules* **1999**, *32*, 1694.

(35) Kato, K.; Uchida, E.; Kang, E.-T.; Uyama, Y.; Ikada, Y. *Prog. Polym. Sci*. **2003**, *28*, 209.

(36) Li, D.; Sheng, X.; Zhao, B. *J. Am. Chem. Soc.* **2005**, *127*, 6248.

(37) Zhao, B.; Haasch, R. T.; MacLaren S. *J. Am. Chem. Soc.* **2004**, *126*, 6124.

(38) von Werne, T.; Patten, T. E. *J. Am. Chem. Soc.* **2001**, *123,* 7497.

(39) Mulvihill, M. J.; Rupert, B. L.; He, R.; Hochbaum, A.; Arnold, J.; Yang, P. *J. Am. Chem. Soc.* **2005**, *127*, 16040.

(40) Lee, M.-T.; Hsueh, C.-C.; Freund, M. S.; Ferguson, G. S. *Langmuir* **1998**, *14,* 6419.

(41) Hancer, M. *Prog. Org. Coat.* **2008**, *63*, 395.

(42) Ulman, A. *Chem. Rev.* **1996**, *96*, 1533.

(43) Wang, M.; Liechti, K. M.; Wang, Q.; White, J. M. *Langmuir* **2005**, *21*, 1848.

(44) Claes, M.; Voccia, S.; Detrembleur, C.; Jérôme, C.; Gilbert, B.; Leclère, Ph.; Geskin, V. M.; Gouttebaron, R.; Hecq, M.; Lazzaroni, R.; Jérôme R. *Macromolecules* **2003**, *36*, 5926.

(45) Ignatova, M.; Voccia, S.; Gilbert, B.; Markova, N.; Cossement, D.; Gouttebaron, R.; Jérôme, R.; Jérôme, C. *Langmuir* **2006**, *22*, 255.

(46) Huang, J.; Murata, H.; Koepsel, R. R.; Russell, A. J.; Matyjaszewski, K. *Biomacromolecules* **2007**, *8*, 1396.

(47) Lego, B.; Skene, W. G.; Giasson, S. *Langmuir* **2008**, *24*, 379.

(48) Sun, X.; Liu, J.; Lee, M. L. *Anal. Chem*. **2008**, *80*, 856.

(49) Matrab, T.; Save, M.; Charleux, B.; Pinson, J.; Cabet-deliry, E.; Adenier, A.; Chehimi, M. M.; Delamar, M. *Surf. Sci*. **2007**, *601,* 2357.

(50) Matrab, T.; Chehimi, M. M.; Boudou, J. P.; Benedic, F.; Wang, J.; Naguib, N. N.; Carlisle*,* J. A. *Diamond Relat. Mater.* **2006**, *15,* 639.

(51) Ejaz, M.; Yamamoto, S.; Ohno, K.; Tsujii, Y.; Fukuda, T. *Macromolecules* **1998**, *31,* 5934.

(52) Wu, Y.; Huang, Y.; Ma, H. *J. Am. Chem. Soc.* **2007**, *129*, 7226.

(53) Kong, H.; Gao, C.; Yan, D. *J. Am. Chem. Soc*. **2004**, *126*, 412.

(54) Qin, S.; Qin, D.; Ford, W. T.; Resasco, D. E.; Herrera J. E. *J. Am. Chem. Soc*. **2004**, *126*, 170.

(55) Holzinger, D.; Kickelbick, G. *Chem. Mater*. **2003**, *15,* 4944.

(56) Xu, F. J.; Cai, Q. J.; Kang, E. T.; Neoh, K. G.; Zhu, C. X. *Organomettalics* **2005**, *24*, 1768.

(57) Xu, F. J.; Kang, E. T.; Neoh, K. G. *J. Mater. Chem.* **2006**, *16*, 2948.

(58) Chapman, B. N. *Glow Discharge Processes: Sputtering and Plasma Etching*; John Wiley & Sons, Inc.: New York, 1980.

(59) Xie, L.; Jiao, L.; Dai, H. *J. Am. Chem. Soc.* **2010**, *132*, 14751.

(60) Liston, E. M.; Martinu, L.; Wertheimer, M. R. *J. Adhes. Sci. Technol.*

1993, *7*, 1091.

(61) Hung, L. S.; Zheng, L. R.; Mason, M. G. *Appl. Phys. Lett.* **2001**, *78*, 673.

(62) Garbassi, F.; Morra, M.; Occhiello, E. *Polymer Surfaces: From Physics to Technology*; John Wiley & Sons, Ltd.: Chichester, U.K., 1998.

(63) Raĭzer, Y. P. *Gas Discharge Physics*; Springer-Verlag: Berlin, Germany, 1997.

(64) Yasuda, H. *Plasma Polymerization*; Academic Press: Orlando, FL, 1985.

(65) Garrod, R. P.; Harris, L. G.; Schofield, W. C. E.; McGettrick, J.; Ward, L. J.; Teare, D. O. H.; Badyal, J. P. S. *Langmuir* **2007**, *23,* 689

(66) Coulson, S. R.; Woodward, I.; Badyal, J. P. S.; Brewer S. A.; Willis, C. *J. Phys. Chem. B* **2000**, *104*, 8836.

(67) Herbert, P. A. F.; O'Neill, L.; Jaroszynska-Wolinska, J. *Chem. Mater.* **2009**, *21*, 4401.

(68) Teare, D. O. H.; Barwick, D. C.; Schofield, W. C. E.; Garrod, R. P.; Beeby, A.; Badyal, J. P. S. *J. Phys. Chem. B* **2005**, *109,* 22407.

(69) Teare, D. O. H.; Schofield, W. C. E.; Garrod, R. P.; Badyal, J. P. S. *J. Phys. Chem. B.* **2005**, 109, 20923.

(70) Bouaidat, S.; Berendsen, C.; Thomsen, P.; Petersen, S. G.; Wolff, A.; Jonsmann, J. *Lab Chip* **2004**, *4*, 632.

(71) Yeo, L. P.; Yan, Y. H.; Lam, Y. C.; Chan-Park, M. B. *Langmuir* **2006**, *22,* 10196.

(72) Tarducci, C.; Kinmond, E. J.; Badyal, J. P. S.; Brewer, S. A.; Willis, C. *Chem. Mater*. **2000**, *12*, 1884.

(73) Thierry, B.; Jasieniak, M.; de Smet, L. C. P. M.; Vasilev, K.; Griesser, H. J. *Langmuir* **2008**, *24,* 10187.

(74) Oehr, C. *Nucl. Inst. Methods Phys. Res. B* **2003**, *208*, 40.

(75) Schofield, W. C. E.; McGettrick, J.; Bradley, T. J.; Badyal, J. P. S.; Przyborski, S. *J. Am. Chem. Soc*. **2006**, *128*, 2280.

(76) Zou, X. P.; Kang, E. T.; Neoh, K. G.; Zhang, Y.; Tan, K. L.; Cui, C. Q.; Lim, T. B. *Polym. Adv. Technol.* **2001**, *12*, 583.

(77) Hynes, A. M.; Shenton, M. J.; Badyal, J. P. S. *Macromolecules* **1996**, *29,* 4220.

(78) Øye, G.; Roucoules, V.; Oates, L. J.; Cameron, A. M.; Cameron, N. R.; Steel, P. G.; Badyal, J. P. S.; Davis, B. G.; Coe, D. M.; Cox, R. A. *J. Phys. Chem. B* **2003**, *107*, 3496.

(79) Teare, D. O. H.; Schofield, W. C. E.; Roucoules, V.; Badyal, J. P. S. *Langmuir* **2003**, *19*, 2398.

(80) Hutton, S. J.; Crowther, J. M.; Badyal, J. P. S. *Chem. Mater.* **2000**, *12*, 2282.

(81) Tarducci, C.; Schofield, W. C. E.; Badyal, J. P. S.; Brewer, S.; Willis, C. *Chem. Mater.* **2001**, *13*, 1800.

(82) Tarducci, C.; Schofield, W. C. E.; Badyal, J. P. S.; Brewer, S. A.; Willis, C. *Chem. Mater.* **2002**, *14*, 2541.

(83) Tarducci, C.; Badyal, J. P. S.; Brewer, S. A.; Willis, C. *Chem. Commun.* **2005**, 406.

(84) Coulson, S. R.; Woodward, I. S.; Badyal, J. P. S.; Brewer, S. A.; Willis, C. *Langmuir* **2000**, *16*, 6287.

(85) Moulder, J. F.; Stickle, W. F.; Sobol, P. E.; Bomben, K. D. *Handbook of X-Ray Photoelectron Spectroscopy: A Reference Book of Standard Spectra for Identification and Interpretation of XPS data*; Perkin-Elmer Corp.: Eden Prarie, MN, 1992.

(86) Beamson, G.; Briggs, D. *High-Resolution XPS of Organic Polymers, The Scienta ESCA 300 Database*; John Wiley & Sons, Ltd: Chichester, 1992.

(87) Banwell, C. N.; McCash, E. M. *Fundamentals of Molecular Spectroscopy*, 4th ed, McGraw-Hill: London, 1994.

(88) Zhang, Z.; Ding, Z.; Koshikawa, T.; Iyasu, T.; Shimizu, R.; Yoshikawa, H.; Fukushima, S.; Tanaka, A. *Surf. Sci.* **2005**, *592*, 18.

(89) Hippert, F.; Geissler, E.; Hodeau, J. L.; Lelièvre-Berna, E.; Regnard; J.-R. *Neutron and X-ray Spectroscopy*; Springer: Dordrecht, Netherlands, 2006.

(90) Hollas, J. M. *Modern Spectroscopy*, 4th ed; John Wiley & Sons Ltd.: Chichester, U.K., 2004; Chapter 8.

(91) Clayden, J.; Greeves, N.; Warren, S.; Worthers, P. *Organic Chemistry;* Oxford University Press: Oxford, U.K., 2001.

(92) Williams, D. H.; Fleming, I. *Spectroscopic Methods in Organic Chemistry*, 5th ed; McGraw-Hill, London, U.K., 1995.

(93) Lin-Vien, D.; Colthrup, N. B.; Fateley, W. G.; Grasselli, J. G. *The Handbook of Infrared and Raman Characteristic Frequencies of Organic Molecules*; Academic Press: Boston, 1991.

(94) Stuart, B. H. *Infrared Spectroscopy: Fundamentals and Applications*; John Wiley & Sons Ltd.: Chichester, U.K., 2004.

(95) Kemp, W. *Organic Spectroscopy*, 3rd ed; Palgrave Macmillan: Basingstoke, U.K., 1991.

(96) McQuillan, A. J. *Adv. Mater.* **2001**, *13*, 1034.

(97) Lefèvre, G. *Adv. Colloid Interface Sci.* **2004**, *107*, 109.

(98) Hind, A. R.; Bhargava, S. K.; McKinnon A. *Adv. Colloid Interface Sci.* **2001**, *93*, 91.

(99) Tortonese, M.; Barrett, R. C.; Quate, C. F. *Appl. Phys. Lett.* **1993**, *62*, 834.

(100) Asay, D. B.; Kim S. H. *J. Chem. Phys.* **2006**, *124*, 174712.

(101) Jaquith, M. J.; Anthony, J. E.; Marohn, J. A. *J. Mater. Chem.* **2009**, *19*, 6116.

(102) Cui, H.; Kalinin, S. V.; Yang, X.; Lowndes, D. H. *Nano Lett.* **2004**, *4*, 2157.

(103) Overney, R. M.; Meyer, E.; Frommer, J.; Brodbeck, D. Lüthi, R.; Howald, L.; Güntherodt, H.-J.; Fujihira, M.; Takano, H.; Gotoh Y. *Nature* **1992**, *359*, 133.

(104) Meyer, G.; Amer, N. M. *Appl. Phys. Lett.* **1988**, *53*, 1045.

(105) Neubauer, G.; Cohen, S. R.; McClelland, G. M.; Horne, D.; Mate, C. M. *Rev. Sci. Instrum.* **1990**, *61*, 2296.

(106) Meyer, G.; Amer, N. M. *Appl. Phys. Lett.* **1988**, *53*, 1045.

(107) Binnig, G.; Quate, C. F.; Gerber, C. *Phys. Rev. Lett.* **1986**, *56*, 930.

(108) Martin, Y.; Williams C. C.; Wickramasinghe, H. K. *J. Appl. Phys.* **1987**, *61*, 4723.

(109) Nakajima, K.; Kageshima, M.; Ara, N.; Yoshimura, M.; Kawazu, A.

Appl. Phys. Lett. **1993**, *62*, 1892.

(110) Nichols, J. A.; Gundlach, D. J.; Jackson, T. N. *Appl. Phys. Lett*. **2003**, *83*, 2366.

(111) Yan, H.; Park, S. H.; Finkelstein, G.; Reif, J. H.; LaBean, T. H. *Science* **2003***, 301*, 1882.

(112) Kiriy, A.; Gorodyska, G.; Minko, S.; Tsitsilianis, C.; Jaeger, W.; Stamm, M. *J. Am. Chem. Soc.* **2003**, *125*, 11202.

(113) Ducheyne, P.; Qiu, Q. *Biomaterials* **1999**, *20*, 2287.

(114) Capella, B.; Dietler, G. *Surf. Sci. Rep.* **1999**, *34*, 1.

(115) Jalili, N.; Laxminarayana, K. *Mechatronics* **2004**,*14*, 907.

(116) Weisenhorn, A. L.; Khorsandi, M.; Kasas, S.; Gotzos, V.; Butt, H.-J. *Nanotechnology* **1993**, *4*, 106.

(117) Sommer, F.; Duc, T. M.; Pirri, R.; Meunier, G.; Quet, C. *Langmuir* **1995**, *11*, 440.

(118) Dinte, B. P.; Watson, G. S.; Dobson, J. F.; Myhra, S. *Ultramicroscopy* **1996**, *63*, 115.

(119) Yang, C.-W.; Hwang, I.-S.; Chen, Y. F.; Chang, C. S.; Tsai, D. P. *Nanotechnology* **2007**, *18*, 084009.

(120) Schmitz, I.; Schreiner, M.; Friedbacher, G.; Grasserbauer, M. *Appl. Surf. Sci.* **1997**, *115*, 190.

(121) Brown, P. S.; Wood, T. J.; Schofield, W. C. E.; Badyal, J. P. S. *ACS Appl. Mater. Interfaces* **2011**, *3*, 1204.

(122) McQuarrie, D. A.; Simon, J. D. *Physical Chemistry: A Molecular Approach;* University Science Books: Sausalito, CA, 1997.

(123) Müller, M. *Introduction to Confocal Fluorescence Microscopy*, 2nd ed.; SPIE Press: Washington, DC, 2006.

(124) O'Connor, D. J.; Sexton, B. A.; Smart, R. S. C. *Surface Analysis Methods in Materials Science*, 2nd Ed.; Springer-Verlag: Berlin, Germany, 2002.

(125) Starov, V. M.; Velarde, M. G.; Radke, C. J. *Wetting and Spreading Dynamics*, CRC Press, Taylor and Francis Group: Boca Raton, Florida, 2007.

(126) De Grennes, P.-G.; Brochard-Wyart, F.; Quéré, D. *Capillarity and Wetting Phenomena:* Drops, Bubbles, Pearls, Waves; Springer: New York, 2004.

(127) Kwok, D. Y.; Leung, A.; Lam, C. N. C.; Li, A.; Wu, R; Neumann, A. W. *J. Colloid Interface Sci*. **1998**, *206*, 44.

(128) Chin, S. L. *Fundamentals of Laser Optoelectronics*; World Scientific: Singapore, 1989; Chapter 3.

(129) Zayim, E. O.; Baydogan, N. D. *Sol. Energy Mater. Sol. Cells* **2006**, *90*, 402.

(130) Tabet, M. F.; McGahan, W. A. *Thin Solid Films* **2000**, *370*, 122.

(131) Synowicki, R. A. *Thin Solid Films* **1998***, 313*, 394.

CHAPTER 2

TAILORING THE DENSITY OF SURFACE TETHERED BOTTLE-BRUSHES

2.1 INTRODUCTION

Well-defined linear polymer brushes bearing a large number of covalently bound polymer side chains are commonly referred to as molecular bottle-brushes. These have attracted significant attention in view of their novel properties, which include stimuli-responsive action[1] and supersoft rheological behaviour,[2] for potential applications such as sensors,[3] nanoscopic templates,[4,5,6,7] photonic crystals[8] and molecular tensile machines.[9] Furthermore, bottle-brush polymers dispersed in solution have been shown to display extremely low friction behaviour attributable to intra- and inter-molecular repulsion between the densely crowded bristle segments.[10,11] Based upon this premise, covalent tethering of well-defined polymer bottle-brushes to solid surfaces would be expected to confer improved lubricity as a consequence of exacerbated steric crowding.

There are three distinct methodologies for the synthesis of molecular bottle-brushes. First, there are 'grafting *to'* approaches which entail coupling pre-formed macromolecular side chains to polymeric backbones.[12,13,14] These suffer from an inherently limited density of side chain attachment, owing to steric constraints. Second, there are 'grafting *through'* methods which comprise the polymerization of macromonomers (pre-formed oligomers bearing a polymerizable group and a side chain already intact). These tend to undergo a loss of polymerization control with increasing side chain length leading to poor polydispersity.[15,16,17] Finally, there are 'grafting *from'* methods which involve controlled polymerization of side chains from initiation sites located along the length of a well defined polymer backbone. Using this method, intrinsic control over backbone and side chain sizes is achievable, leading to the synthesis of complex bottle-brush structures.[7,18,19,20] However in all of these cases, studies have focused on the solution phase synthesis or substrate-specific systems (e.g., PTFE[21]) rather than targeting substrate-independent surface tethering of the polymer bottle-brushes.

Atom transfer radical polymerization (ATRP) is widely used for controlled / living polymerization because of the mild reaction conditions involved and its applicability to a wide range of monomer functionalities.[22,23] This technique is frequently adapted for the synthesis of well defined co-

polymers, for instance the formation of block co-polymers using successive ATRP polymerizations in conjunction with the serial reactivation of 'living' halide-capped chain ends.[24,25,26] Another variant comprises well-defined linear polymer brushes bearing a large number of covalently bound polymer side chains which are referred to as molecular bottle-brushes. ATRP initiated from surface sites is well documented for producing densely grafted polymer / co-polymer brush layers.[27,28,29,30,31] However, the grafting *from* approach for attaching polymer bottle-brushes onto surfaces is more challenging due to the inherent steric crowding of the backbone polymers, which hinder the growth of side chains (bristles). Such steric crowding is symptomatic of densely packed ATRP initiator sites prepared using self-assembled monolayers (SAMs).[32,33,34,35,36] Previous attempts aimed at surface functionalisation with bottle-brushes have been limited to using grafting *through* methods yielding poorly defined bristles,[37,38] or just physisorption of pre-formed bottle-brushes from solution.[39,40,41,42] There was also an earlier attempt to employ the grafting *from* approach using successive surface initiated ATRP polymerizations of the backbone and then side chain segments by using mixed SAMs to lower initiator density at the substrate surface (to provide sufficient spacing between grafts for the subsequent growth of side chains); however, no conclusive evidence was presented for the tethering of well defined bottle-brushes to the surface.[43] Furthermore, there are inherent disadvantages associated with SAMs which include long term instability towards oxidation in the case of thiol – gold systems,[44,45] moisture sensitivity of silanes,[46,47,48] and the requirement for multiple step syntheses to prepare appropriate SAM initiator molecules. All of the aforementioned drawbacks can potentially be overcome by plasmachemical deposition to create ATRP initiator layers in a single step. For example, pulsed plasma deposited poly(vinylbenzyl chloride) initiator layers have been successfully employed for the ATRP growth of well-defined polymer brushes onto a variety of solid substrates.[49] This approach ensures covalent attachment to the substrate via reactive sites created at the interface by electrical discharge during the onset of nanolayer deposition (Si-C bonds will be responsible for adhesion in silicon and glass substrates,[50] M-C bonds in metals[51] and free radicals created by the electrical discharge in polymers.[52])

Moreover, the density of functional groups presented at the surface can be customised by careful tuning of the electrical discharge parameters.

In this study, controlled ATRP surface grafting of poly(glycidyl methacrylate) brush layers is demonstrated using plasma deposited poly(vinylbenzyl chloride) nanofilms. These are then derivatised with bromoacetic acid to introduce ATRP initiation sites along the polymer brush backbone needed for the subsequent ATRP grafting of poly(sodium 4-styrenesulfonate) side chains (bristles) to yield bottle-brushes, Scheme 2.1.

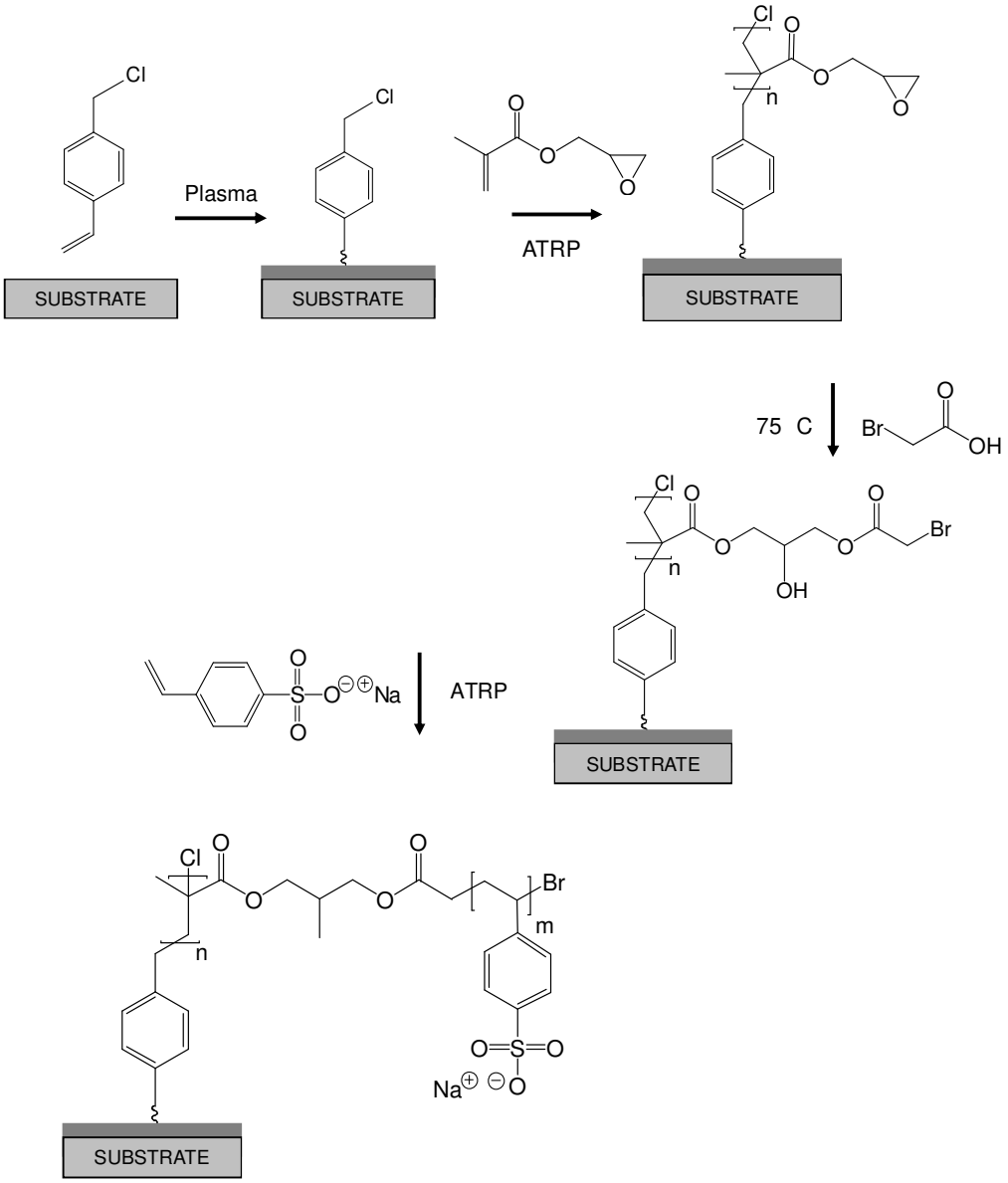

Scheme 2.1: Idealised scheme of bottle-brush polymer grafting reactions. Poly(glycidyl methacrylate) brushes are grafted by ATRP onto plasma deposited poly(vinylbenzyl chloride) initiator layers, followed by esterification of poly(glycidyl methacrylate) with bromoacetic acid to form tethered macroinitiator sites for the subsequent ATRP of poly(sodium 4-styrenesulfonate) side chain 'bristles'.

2.2 EXPERIMENTAL

2.2.1 Plasma Deposition of ATRP Initiator Layers

Plasma depositions were performed inside a cylindrical glass reactor (5.5 cm diameter, 475 cm^3 volume) located within a Faraday cage, and evacuated using a 30 L min^{-1} rotary pump via a liquid nitrogen cold trap (base pressure less than 2 x 10^{-3} mbar and leak rate better than 6 x 10^{-9} mol per second[53]). A copper coil wound around the reactor (4 mm diameter, 10 turns, and located 10 cm away from the gas inlet) was connected to a 13.56 MHz radio frequency (RF) power supply via an L-C matching network. A signal generator was used to trigger the RF power supply. Prior to film deposition, the whole apparatus was thoroughly scrubbed using detergent and hot water, rinsed with propan-2-ol, and oven dried. Substrate preparation (silicon wafer pieces) comprised successive sonication in propan-2-ol and cyclohexane for 15 min prior to insertion into the centre of the chamber. Further cleaning entailed running a 50 W continuous wave air plasma at 0.2 mbar for 30 min prior to film deposition. The vinylbenzyl chloride (+97%, Aldrich) precursor was loaded into a sealable glass tube, degassed via several freeze-pump-thaw cycles, and then attached to the reactor. Monomer vapour was then allowed to purge the apparatus at a pressure of 0.2 mbar for 3 min prior to electrical discharge ignition. Pulsed plasma deposition was performed using a duty cycle on-period of 100 μs and a duty cycle off-period of 4 ms in conjunction with a peak power of 30 W. Continuous wave plasma deposition was carried out at 30 W. Upon plasma extinction, the precursor vapour continued to pass through the system for a further 3 min, and then the chamber was evacuated back down to base pressure.

2.2.2 Bottle-Brush Synthesis

For surface grafting of the poly(glycidyl methacrylate) backbone, plasma deposited poly(vinylbenzyl chloride) initiator functionalised substrates were placed inside a sealable glass tube containing 5 mmol copper (I) bromide (+98 %, Aldrich), 1 mmol copper (II) bromide (+99 %, Aldrich), 12 mmol 2,2'-bipyridyl (+99 %, Aldrich), 0.05 mol glycidyl methacrylate (+97 %, Aldrich), and 4 mL *N,N*-dimethylformamide (+99.9 %, Fisher), Scheme 2.1. The mixture was thoroughly degassed using freeze-pump-thaw cycles and then

immersed in an oil bath maintained at 80 °C for a range of grafting times (1.0 - 3.5 h). Final cleaning and removal of any physisorbed polymer was achieved by Soxhlet extraction using hot toluene for a minimum of 16 h.

Bromine-containing macroinitiator films were derived from surface tethered ATRP grafted poly(glycidyl methacrylate) brushes via esterification with bromoacetic acid (+99.9 % Aldrich) vapour using a glass reactor placed inside a temperature controlled oven. Bromoacetic acid was loaded into a sealable glass tube, degassed via several freeze-pump-thaw cycles, and then attached to the reactor. The system was evacuated to 4 x 10^{-3} mbar and heated to 75 °C. Next, bromoacetic acid vapour was purged through for 5 min, and then the reaction chamber was isolated from the pump for 4 h to allow reaction, followed by cooling to room temperature and evacuation to base pressure. In order to ensure complete removal of any unreacted bromoacetic acid, the substrates were thoroughly rinsed in high purity water and *N,N*-dimethylformamide (+99.9 %, Fisher).

ATRP grafting of poly(sodium 4-styrenesulfonate) was performed under aqueous conditions, due to the limited solubility of the monomer. A higher copper(II) : copper(I) ratio was required in order to enhance halide capping efficiency, and thereby maintain control.[54] Any trapped gases were removed from 1.0 g sodium 4-styrenesulfonate (+90 % Aldrich) dissolved in 3 mL of high purity water using a minimum of four freeze-pump-thaw cycles. The catalyst system consisted of 0.05 mmol copper (I) bromide, 0.04 mmol copper (II) bromide, and 0.18 mmol 2,2'-bipyridyl; these were added to the solution while it was frozen, together with the plasma deposited poly(vinylbenzyl chloride) or macroinitiator functionalised substrates. The reaction vessel was then immersed into an oil bath set to 50 °C for a predetermined grafting time. The substrate was then thoroughly rinsed in high purity water to remove any physisorbed polymer and allowed to dry in air.

2.2.3 Film Characterisation

Film thicknesses were measured using a spectrophotometer (nkd-6000, Aquila Instruments Ltd.). Transmittance-reflectance curves (350 - 1000 nm wavelength range) were acquired for each sample and fitted to a Cauchy material model using a modified Levenberg-Marquardt algorithm.[55]

Surface elemental compositions were obtained by X-ray photoelectron spectroscopy (XPS) using a VG ESCALAB II electron spectrometer equipped with a non-monochromated Mg $K\alpha_{1,2}$ X-ray source (1253.6 eV) and a concentric hemispherical analyser. Photoemitted electrons were collected at a take-off angle of 30° from the substrate normal, with electron detection in the constant analyser energy mode (CAE, pass energy = 20 eV). Experimentally determined instrument sensitivity factors were taken as C(1s): O(1s): Cl(2p): Br(3d): S(2p): Na(1s) equals 1.00 : 0.46 : 0.29 : 0.29 : 0.52 : 0.05.

Infrared spectra were acquired using a FTIR spectrometer (Perkin-Elmer Spectrum One) fitted with a liquid nitrogen cooled MCT detector operating at 4 cm^{-1} resolution across the 700 - 4000 cm^{-1} range. The instrument included a variable angle reflection-absorption accessory (Specac) set to a grazing angle of 66° for silicon wafer substrates and adjusted for p-polarisation.

2.2.4 Nanotribology

Lateral force microscopy was performed in contact mode using a Nanoscope IV (Digital Instruments) in combination with a fluid cell containing high purity water (BS 3978 Grade 1, water purification system Sartorius Arium 611, with a total organic content of <1 parts per billion and resistivity greater than 18 MΩ cm), and using a triangular Si_3N_4 contact mode SPM probe tip (Spring constant 0.24 N m^{-1}, Bruker Nano Inc.). To ensure consistent results, the same probe tip was used for all measurements. Normal loads were calculated using the nominal force constant provided by the manufacturer in conjunction with force-distance profiles, and varied by means of the contact mode set point. Lateral force microscopy data was collected over 1 µm x 1 µm regions using a scan angle of 90° and a scan rate of 3 Hz, giving rise to a tip movement speed of 6 µm s^{-1}. Sliding (dynamic) friction data was measured in Volts, and is reported as half of the difference between trace and retrace signals for the central 800 nm region of each scan line (thus excluding any scanning tip trace-retrace turnaround contributions attributable to static friction[56]). This data is directly proportional to friction,[57,58] and was not converted to absolute friction force values because the lateral spring constant was not known. The dependency of lateral spring constants upon their

measurement methods precludes direct comparison to similar studies.[11,59,60,61,62] Even if the method used to determine the lateral spring constant was completely reliable, friction coefficients are still highly dependent on the measurement system employed, and the parameters involved (scan rate, contact area, counter surface etc).[63,64,65] Hence, for the purpose of the present study, the tribological experiments were undertaken by utilising an internal reference – namely the ATRP grafted poly(sodium 4-styrenesulfonate) brushes tethered to pulsed plasma deposited poly(vinylbenzyl chloride) layer. Each reading was taken as the mean of 128 scan lines. The same tip was used for each comparative set of tribology measurements; all the scanning probe friction measurements were repeated several times and showed no variation (including at higher normal loads). This indicates that the tip shape was not modified to any significant extent.

2.3 RESULTS

2.3.1 Plasma Deposition of Poly(vinylbenzyl chloride) ATRP Initiator Layers

Pulsed plasma deposition of poly(vinylbenzyl chloride) yielded a linear film deposition rate of 193 ± 34 nm min^{-1} and water contact angle values of 80 ± 1 ° demonstrating the reproducibility of the technique, Figure 2.1. XPS analysis of the pulsed plasma deposited poly(vinylbenzyl chloride) films gave elemental compositions corresponding to the expected theoretical values based on the vinylbenzyl chloride monomer, thus indicating good structural retention of the benzyl chloride functionality, Table 2.1. In addition, the absence of any Si(2p) XPS signal confirmed pinhole free coverage of the underlying silicon wafer substrate.[66] Further evidence for the structural integrity of pulsed plasma deposited poly(vinylbenzyl chloride) films was obtained by infrared spectroscopy, where the fingerprint features closely match those measured for the monomer, Figure 2.2. These include halide functionality (required for subsequent ATRP initiation) at 1263 cm^{-1} (CH_2 wag mode for CH_2-Cl), and para-substituted benzene ring stretches at 1495 cm^{-1} and 1603 cm^{-1}.[49,67] In addition, the observed loss of the vinyl double bond stretch at 1629 cm^{-1} is consistent with polymerization. In the case of continuous wave plasma deposited poly(vinylbenzyl chloride) films, greater structural disruption was evident from the slightly lower chlorine content detected by XPS, and the much weaker infrared absorbances for the characteristic benzyl chloride functionalities, Table 2.1 and Figure 2.2.

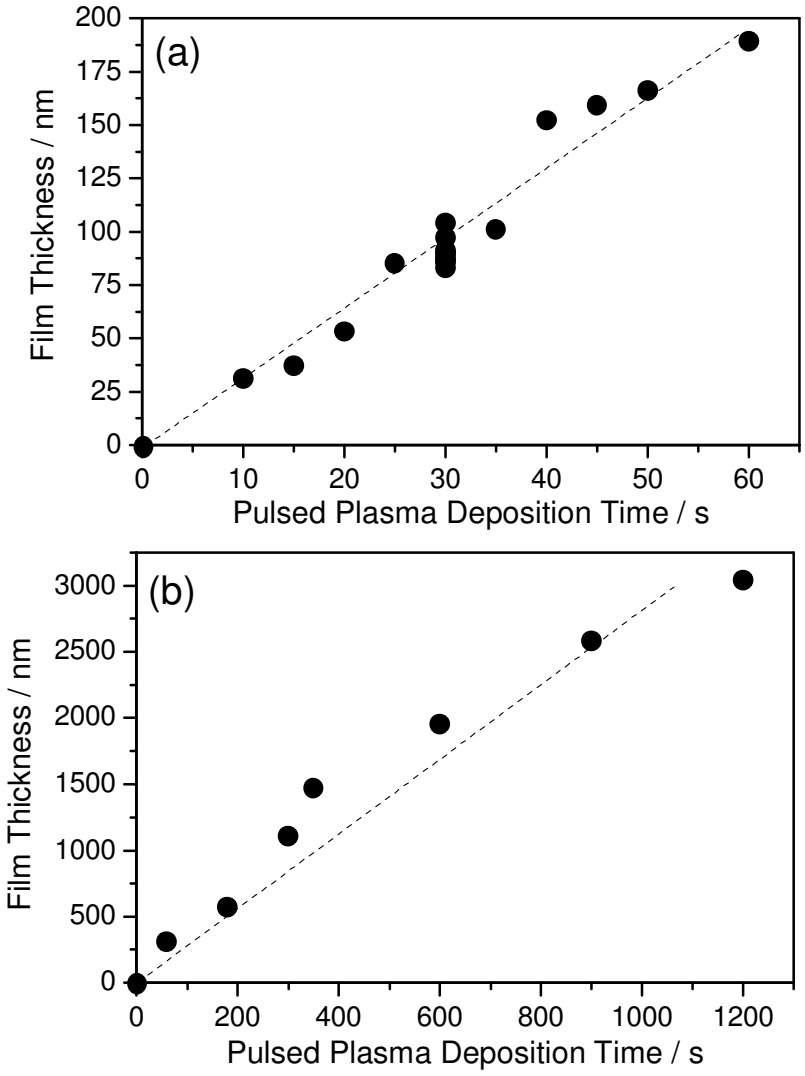

Figure 2.1: Film thickness of pulsed plasma deposited poly(vinylbenzyl chloride) as a function of deposition period in the range (a) of 10 – 60 s; and (b) 60 – 1200 s.

Table 2.1: XPS elemental compositions of plasma deposited poly(vinylbenzyl chloride) films, and ATRP grafted polymer brushes and bottle-brushes (error values are one standard deviation).

Surface		***XPS Elemental Composition***					
		C %	***O %***	***Cl %***	***S %***	***Br %***	***Na %***
Plasma deposited poly(vinylbenzyl chloride)	*Theoretical*[*]	90	0	10	0	0	0
	Pulsed	90 ± 1	0	10 ± 1	0	0	0
	Continuous Wave	91 ± 1	0	9 ± 1	0	0	0
ATRP grafted poly(glycidyl methacrylate)	*Theoretical**	70	30	0	0	0	0
	Pulsed	69 ± 2	31 ± 2	0	0	0	0
	Continuous Wave	72 ± 4	28 ± 4	0	0	0	0
ATRP grafted poly(sodium 4-styrenesulfonate)	*Theoretical**	61	23	0	8	0	8
	Pulsed	68 ± 2	24 ± 1	0	7 ± 1	0	2 ± 1
ATRP grafted poly(glycidyl methacrylate) reacted with bromoacetic acid	*Theoretical**	60	33	0	0	7	0
	Pulsed	70 ± 1	25 ± 1	0	0	4 ± 1	0
	Continuous Wave	70 ± 6	26 ± 4	0	0	4 ± 2	0
ATRP grafted poly(glycidyl methacrylate)-poly(sodium 4-styrenesulfonate)	*Pulsed*	85 ± 6	13 ± 5	0	2 ± 1	0	0
	Continuous Wave	73 ± 3	23 ± 2	0	3 ± 1	0	0

[*] Theoretical compositions are based on the % number of atoms within an ideal structure, e.g., the poly(vinylbenzyl chloride) repeat unit consists of 9 C and 1 Cl atom therefore the theoretical composition is 90 % C and 10 % Cl, Scheme 2.1.

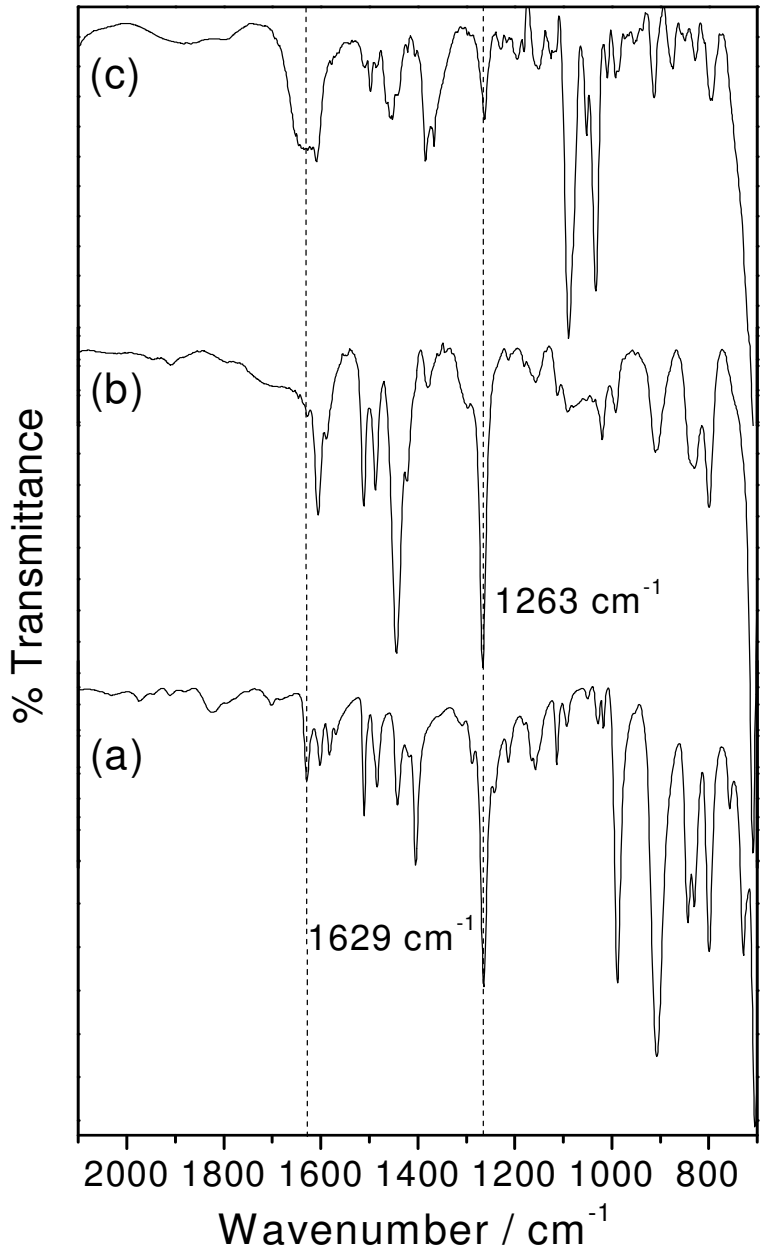

Figure 2.2: Infrared spectra of: (a) the vinylbenzyl chloride monomer; (b) 124 nm thick pulsed plasma deposited poly(vinylbenzyl chloride) layer; and (c) 69 nm thick continuous wave plasma deposited poly(vinylbenzyl chloride) layer.

2.3.2 ATRP Grafting of Poly(glycidyl methacrylate) and Poly(sodium 4-styrenesulfonate)

ATRP grafted poly(glycidyl methacrylate) brushes grown from the structurally well defined pulsed plasma deposited poly(vinylbenzyl chloride) ATRP initiator films yielded XPS elemental compositions in close agreement to those calculated for poly(glycidyl methacrylate), Table 2.1 and Scheme 2.1. Absence of a Cl(2p) XPS signal from the underlying initiator layer verified complete coverage by polymer brushes. Characteristic infrared absorbances measured for both glycidyl methacrylate monomer and ATRP grafted poly(glycidyl methacrylate) layers include the ester C=O stretch at 1726 cm^{-1} (1714 cm^{-1} for the monomer, due to conjugation with the vinyl group) and the C-O stretch at 1152 cm^{-1}, Figure 2.3.[67,68] Loss of the monomer vinyl absorptions at 1637 cm^{-1} (C=C stretch) and 941 cm^{-1} (vinyl CH_2 wag) provided further evidence of ATRP having taken place. The static water contact angle of ATRP grafted poly(glycidyl methacrylate) brushes was 72 ± 3°.[69] The controlled nature of surface initiated ATRP was confirmed by monitoring the linear increase of poly(glycidyl methacrylate) film thickness versus grafting time, yielding a deposition rate of 70 ± 12 nm h^{-1}, Figure 2.4. At longer reaction times (>3.5 h) the growth rate declined, and further increases in thickness beyond 300 nm could not be obtained, signifying termination. Whilst this grafting rate exceeds those typically reported in the literature for surface initiated ATRP of poly(glycidyl methacrylate) in organic solvents, direct comparison of polymerization rates is problematic given the number of variables that affect ATRP kinetics (i.e., solvent(s), polymerization temperature, activity of the catalyst system (itself dependent on the ligands, transferable halide and ratio of activator to deactivator complexes) and, in the case of surface initiated ATRP, the initiator density[70,71]).

Nonetheless, one report of glycidyl methacrylate ATRP grafting under reasonably comparable conditions (bipyridine ligand, *N,N*-dimethylformamide solvent, CuBr:$CuBr_2$ ratio 4:1 rather than 5:1 used in the present study, and performed at room temperature rather than 80 °C) reported a deposition rate of <1 nm h^{-1} using dry *N,N*-dimethylformamide solvent and approximately 5 nm h^{-1} using a 2:1 *N,N*-dimethylformamide:water solvent mixture.[72] Another example performed at 85 °C (using a CuCl/$CuCl_2$ based catalyst and 1:1 *N,N*-

dimethylformamide:water solvent) reported grafting rates of 10 nm h^{-1}.[73] As *N,N*-dimethylformamide is hygroscopic, and was not strictly dry in the present study, some water is to be expected in the polymerization solution. However, even taking this into account, it can be seen that the polymerization is extremely fast in comparison to literature values.

Furthermore, the maximum brush layer thickness achieved (300 nm) greatly exceeds those previously reported for ATRP of poly(glycidyl methacrylate) prior to termination (100-150 nm).[71,74] Moreover, 300 nm thickness corresponds to a *minimum* molecular weight of approximately 190,000 g mol^{-1} (calculated from bond lengths and assuming chains are fully stretched, therefore clearly an underestimation) whereas bulk or solution phase ATRP of glycidyl methacrylate typically produces polymers of much lower molecular weight.[75]

Because ATRP grafting was expected to proceed more slowly, and termination contributions ordinarily limit the achievable thickness to a greater extent, control experiments were undertaken to ensure the reported thickness readings were not a result of poly(vinylbenzyl chloride) initiator layer swelling. This entailed exposure of 60-100 nm thick pulsed plasma deposited poly(vinylbenzyl chloride) ATRP initiator layers to solutions of glycidyl methacrylate in *N,N*-dimethylformamide at 80 °C for 4 h, followed by Soxhlet cleaning in hot toluene for 16 h (i.e., ATRP conditions with the omission of catalytic copper species). No thickness increase was measured for the dry polymer layer, proving that monomer or solvent swelling does not result in deceptively high thickness readings. Furthermore, no poly(glycidyl methacrylate) was detected by infrared spectroscopy for these samples, thus eliminating the possibility of initiation occurring from residual radicals trapped within the plasma deposited layer, and also eliminating auto polymerization as an alternative mechanism for the reported observations.[76]

Another possible explanation for the fast grafting rate may lie in the polymeric nature of the initiator layers. Huck et al reported rapid ATRP of extremely thick (up to 800 nm) poly[oligo(ethylene glycol) methacrylate] brushes from silane initiators immobilised on PDMS, where the grafting rate was found to increase six-fold in comparison to identical polymerizations performed on silicon.[77] It was proposed that this enhanced rate may be

ascribed to increased initiator group availability on PDMS, due to substrate deformation.[77] Furthermore, it has been shown that free radical polymerization of poly(styrene) and poly(2-vinyl pyridine) from polyamide substrates can produce very thick brush layers as a result of initiation from within the polymer substrate whilst it is swollen by the polymerization solution.[78] Further control experiments therefore consisted of poly(gylcidyl methacrylate) ATRP grafting onto pulsed plasma deposited poly(vinylbenzyl chloride) layers of varying thickness (60 – 150 nm) for 4 h. The measured thickness increases were 222 ± 13 nm with no correlation to the initiator layer thickness. This indicates that initiation does not occur throughout the poly(vinylbenzyl chloride) layer, although ATRP could be initiated from the uppermost tens of nm of the film.

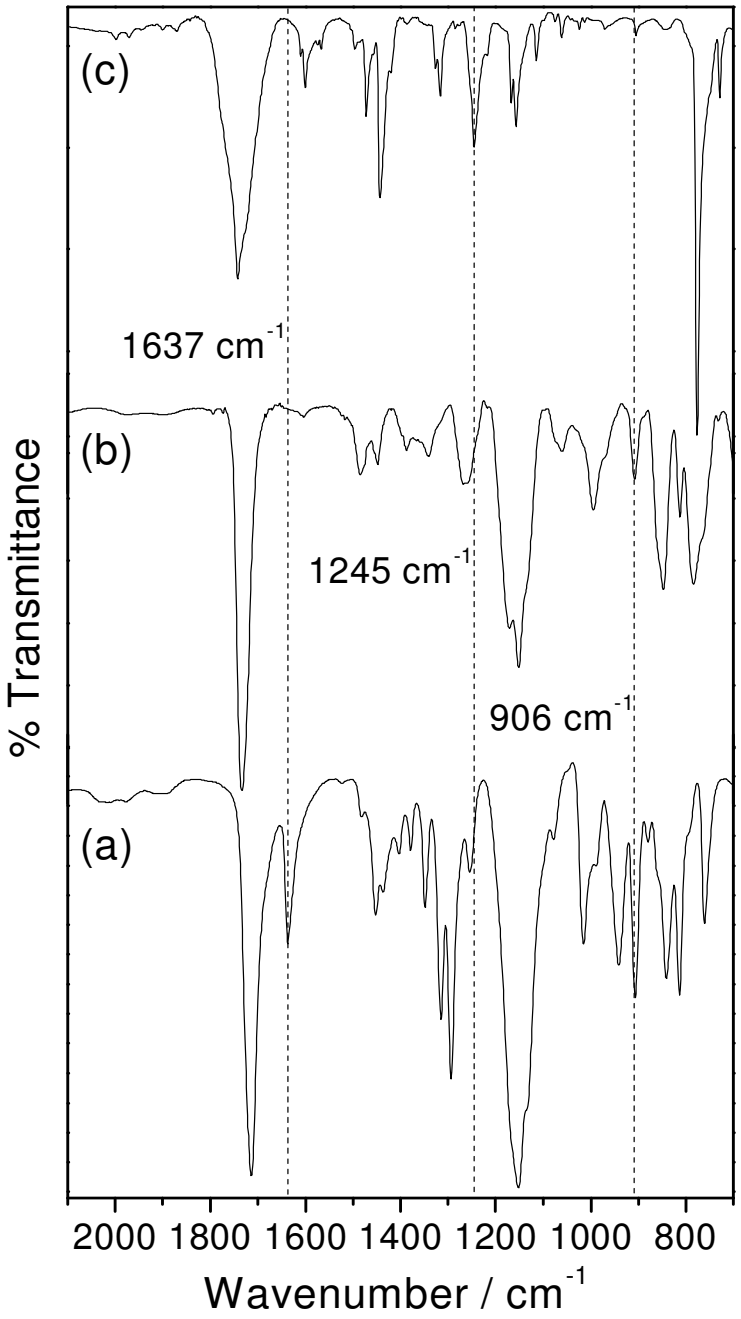

Figure 2.3: Infrared spectra of: (a) the glycidyl methacrylate monomer; (b) ATRP grafted poly(glycidyl methacrylate) grown from pulsed plasma deposited poly(vinylbenzyl chloride) initiator layer; and (c) following 4 h exposure of (b) to bromoacetic acid at 75 °C.

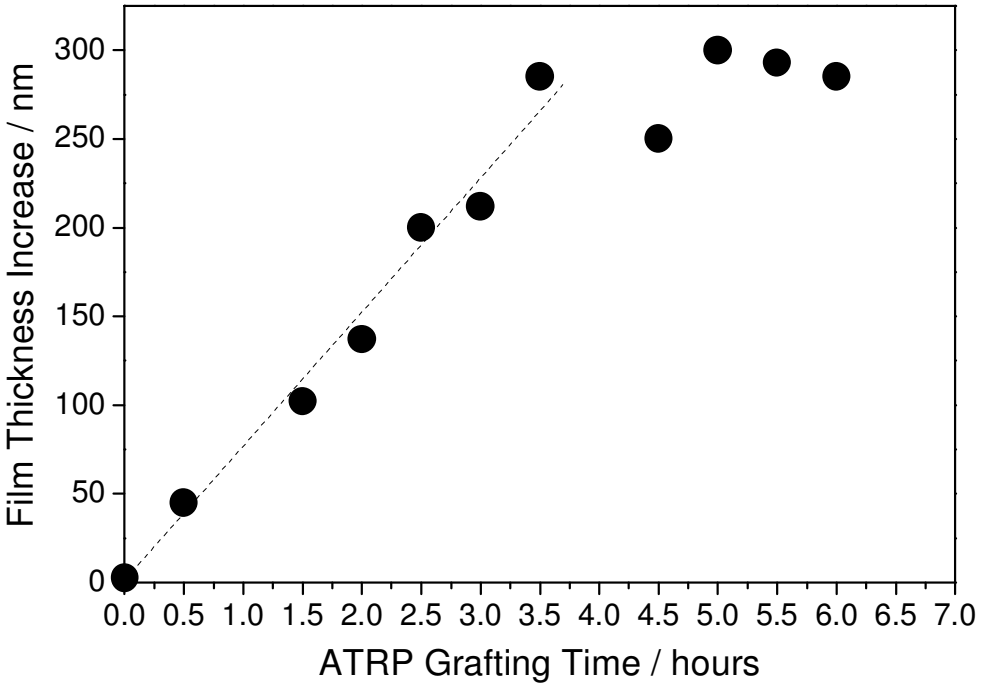

Figure 2.4: Variation of poly(glycidyl methacrylate) film thickness as a function of ATRP grafting time onto pulsed plasma deposited poly(vinylbenzyl chloride) initiator layer.

The XPS elemental compositions and characteristic infrared absorbances of ATRP grafted poly(glycidyl methacrylate) onto continuous wave plasma deposited poly(vinylbenzyl chloride) films were found to be consistent with those measured for the corresponding pulsed plasma deposited poly(vinylbenzyl chloride) ATRP initiator layers, Table 2.1. However, polymer brush film thicknesses following 2 h ATRP grafting onto continuous wave and pulsed plasma deposited layers were 26 ± 5 nm and 137 ± 5 nm respectively, and this is consistent with the poor structural integrity of continuous wave versus pulsed plasma deposited layers.[79]

Similarly, XPS analysis of ATRP grafted poly(sodium 4-styrenesulfonate) grown onto pulsed plasma poly(vinylbenzyl chloride) initiator layers yielded elemental compositions in close agreement with calculated theoretical values, Table 2.1. Absence of a Cl(2p) signal indicated complete coverage of the substrate. The quantity of sodium counter ions measured was found to be much lower than the quantity of sulphur and can be attributed to conversion of the sulfonate groups to form the sulfonic acid.[80,81] ATRP grafted

polymer brush thickness versus time displayed a linear growth rate of 30 ± 2 nm h^{-1}, Figure 2.5. Grafting times exceeding 90 min culminated in a loss of control, which can be attributed to the oxidative breakdown of catalytic species (something which is commonly found for aqueous phase ATRP[82]). Infrared spectroscopy of the ATRP grafted poly(sodium 4-styrenesulfonate) layers revealed fingerprint features matching those associated with the monomer, Figure 2.6. These include absorbances at 1140 cm^{-1}, 1188 cm^{-1} and 1234 cm^{-1} (antisymmetric SO_2 stretches) and 1058 cm^{-1} (symmetric SO_2 stretch).[67] The monomer vinyl C=C stretch absorption at 1638 cm^{-1} disappeared following ATRP polymerization.

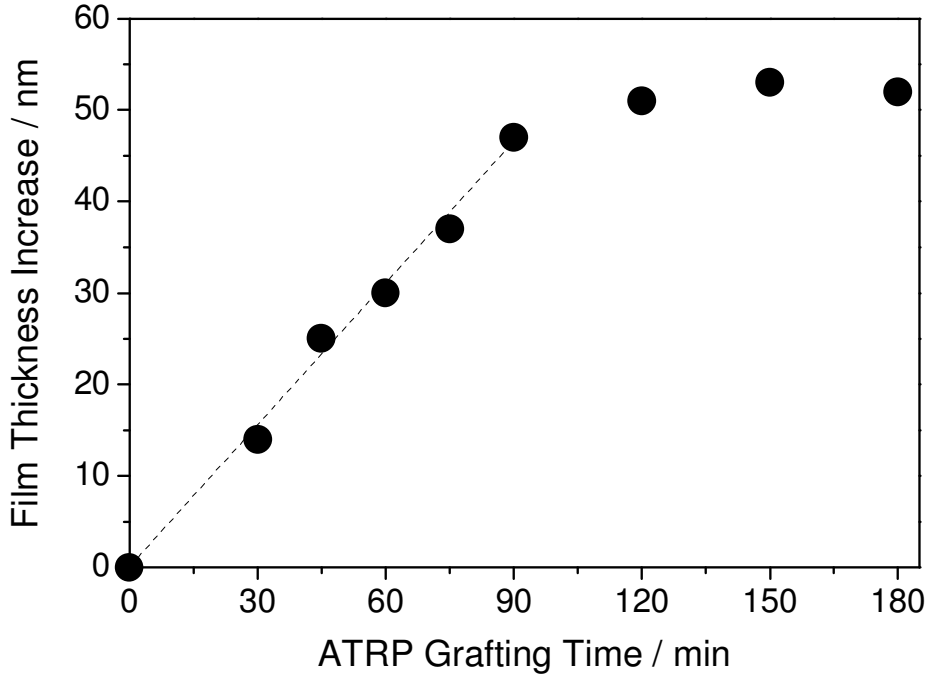

Figure 2.5: Poly(sodium 4-styrenesulfonate) film thickness as a function of ATRP grafting time onto pulsed plasma deposited poly(vinylbenzyl chloride) initiator layer.

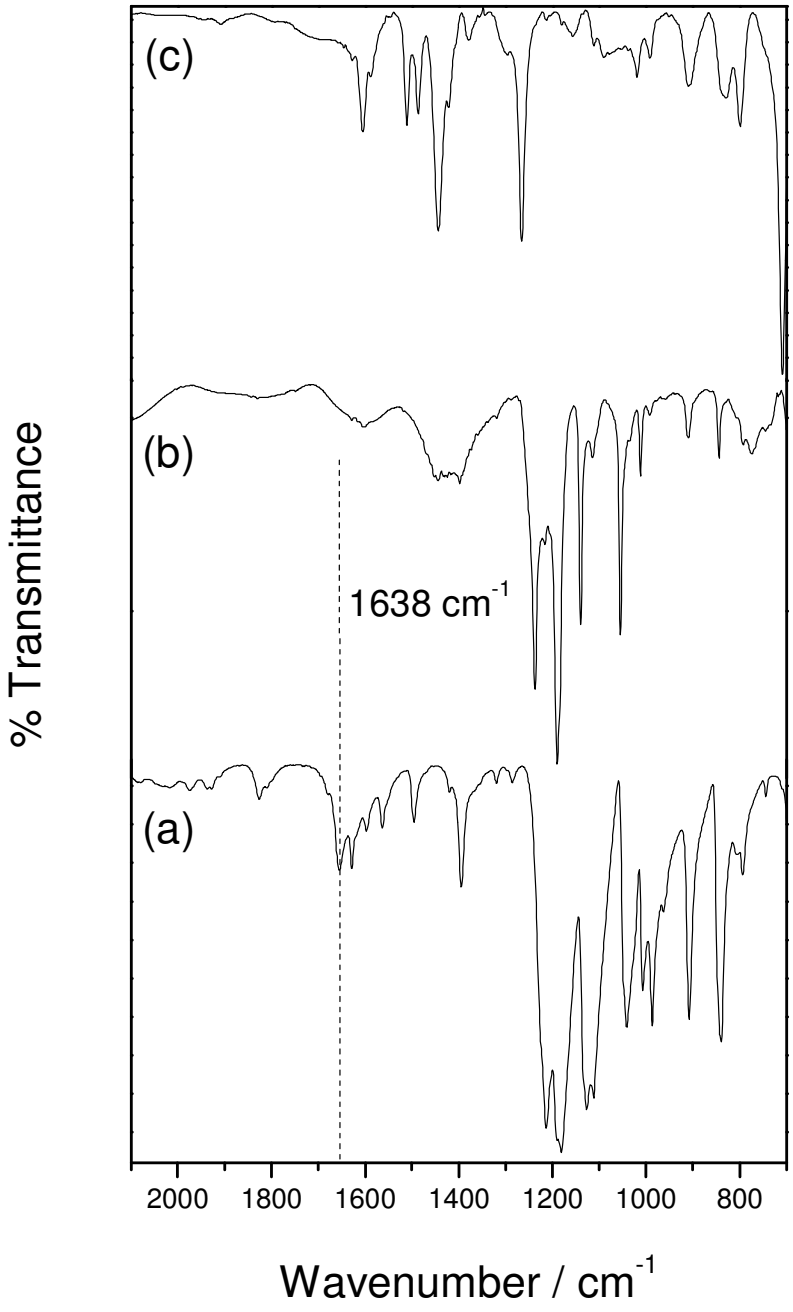

Figure 2.6: Infrared spectra of: (a) the sodium 4-styrenesulfonate monomer; (b) ATRP grafted poly(sodium 4-styrenesulfonate) onto pulsed plasma deposited poly(vinylbenzyl chloride) initiator layer; and (c) pulsed plasma deposited poly(vinylbenzyl chloride) ATRP initiator layer.

2.3.3 Bottle-Brush Fabrication

Poly(glycidyl methacrylate) brushes grafted from plasma deposited poly(vinylbenzyl chloride) layers were exposed to bromoacetic acid in order to introduce ATRP macroinitiator sites along the poly(glycidyl methacrylate) brush backbone, Scheme 2.1. Bromine incorporation was verified by XPS elemental analysis, Table 2.1. Additional evidence for the reaction between pendant epoxide groups of poly(glycidyl methacrylate) and bromoacetic acid was found by infrared spectroscopy, Figure 2.3. Absorbances associated with the epoxide functionality at 1254 cm^{-1} (epoxide ring breathing), 906 cm^{-1} (antisymmetric ring deformation) and 841 cm^{-1} (symmetrical ring deformation) [67,68] were all attenuated and an additional absorbance at 1245 cm^{-1} attributed to the CH_2 wag on CH_2-Br was evident.[67] Furthermore, broadening of the ester C=O stretch absorption at 1726 cm^{-1} confirmed the presence of expected multiple ester environments in the resultant macroinitiator film.[67] The process depicted in Scheme 2.1 is idealised, and incomplete reaction of the epoxide groups with bromoacetic acid must be taken into account when considering the macroinitiator layers. Disappearance of the epoxide infrared absorbance at 906 cm^{-1} has previously been cited as evidence for the complete reaction of poly(glycidyl methacrylate)[74] and this peak is largely attenuated in the macroinitiator infrared spectrum, indicating a successful, but incomplete reaction, Figure 2.3.

In order to provide adequate space for the growth of side chain 'bristles', the macroinitiator graft density was lowered by initiating ATRP of poly(glycidyl methacrylate) from continuous wave plasma deposited poly(vinylbenzyl chloride), which had a lower surface concentration of chlorine atoms, and then exposing the polymer brushes to bromoacetic acid. ATRP grafting of poly(sodium 4-styrenesulfonate) side chains from these macroinitiator layers was confirmed by infrared spectroscopy, Figure 2.7 and Scheme 2.1. The relative intensity of the ester carbonyl stretch at 1726 cm^{-1} from the brush backbone compared to the symmetric SO_2 stretch at 1058 cm^{-1} was reduced with increasing poly(sodium 4-styrenesulfonate) grafting time, indicating the growth of poly(sodium 4-styrenesulfonate) bristles. Further confirmation was obtained by monitoring the increase of film thickness versus ATRP grafting time of poly(sodium 4-styrenesulfonate) side chains, Figure

2.8. Ideally, bottle brush growth would involve grafting of side chain 'bristles' from each repeat unit of the poly(glycidyl methacrylate) backbone, as depicted in Scheme 2.1. However, incomplete reaction of the epoxide groups with bromoacetic acid was observed and grafting of side chains is clearly only possible from successfully reacted repeat units. In addition, the degree of ATRP initiation from generated macroinitiators should also be taken into account. Whilst bromine atoms attached to radical-stabilising ester groups are well known to be efficient ATRP initiators,[83,84,85,86] it is possible that steric restraints may limit the achievable density of grafted poly(sodium 4-styrenesulfonate) side chains. Precise molecular characterisation of the grafted co-polymer brushes is extremely challenging, particularly in the case of plasma deposited initiator layers where detachment of polymer brushes is not possible. Instead, a series of control experiments were undertaken to ascertain that graft co-polymerization had taken place.

In order to prove that ATRP grafting of poly(sodium 4-styrenesulfonate) side chains from the derivatised poly(glycidyl methacrylate) brushes had occurred, corresponding ATRP grafted poly(glycidyl methacrylate) brushes were reacted with acetic acid vapour as a substitute for bromoacetic acid (same derivatisation chemistry but absent halogen initiator atom). Subsequent exposure to ATRP conditions for sodium 4-styrenesulfonate lasting 120 min resulted in no measurable increase in film thickness, thus eliminating the alternative explanation that reactivation of poly(glycidyl methacrylate) chain ends would lead to formation of block co-polymers and account for the observed changes in film thickness and infrared spectra.

Further control experiments involved macroinitiators consisting of bromoacetic acid derivatised poly(glycidyl methacrylate) brushes grafted onto *pulsed* plasma deposited poly(vinylbenzyl chloride) initiator layers, which yielded identical bromine content by XPS analysis, Table 2.1. However, ATRP grafting of poly(sodium 4-styrenesulfonate) for 120 min resulted in an attenuated increase in film thickness (5 nm vs. 24 nm) and a lower amount of sulphur when compared to macroinitiators based on continuous wave plasma deposited poly(vinylbenzyl chloride) nanofilms, Table 2.1.

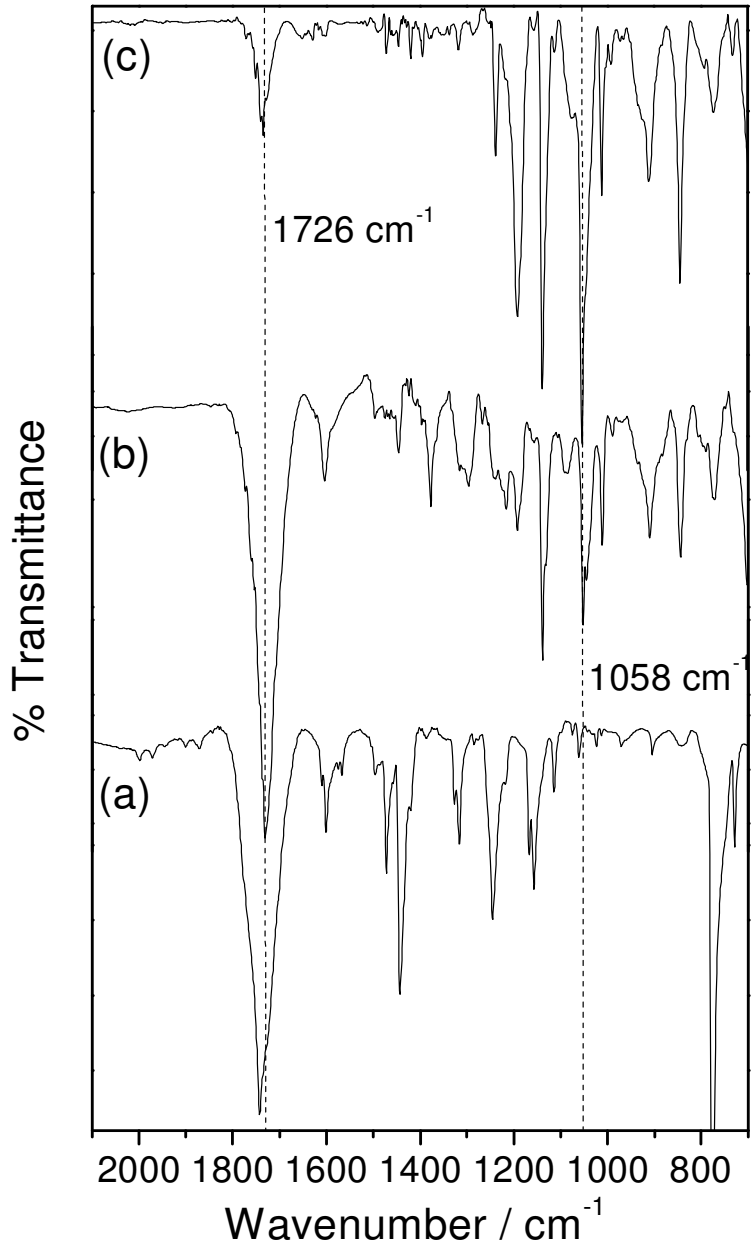

Figure 2.7: Infrared spectra of poly(glycidyl methacrylate) brushes grafted by ATRP onto continuous wave plasma deposited poly(vinylbenzyl chloride) ATRP initiator layer, followed by derivatisation with bromoacetic acid to yield the macroinitiator layer. These were then employed for ATRP grafting of sodium 4-styrenesulfonate side chains (bristles) for: (a) 0 min; (b) 30 min; and (c) 60 min.

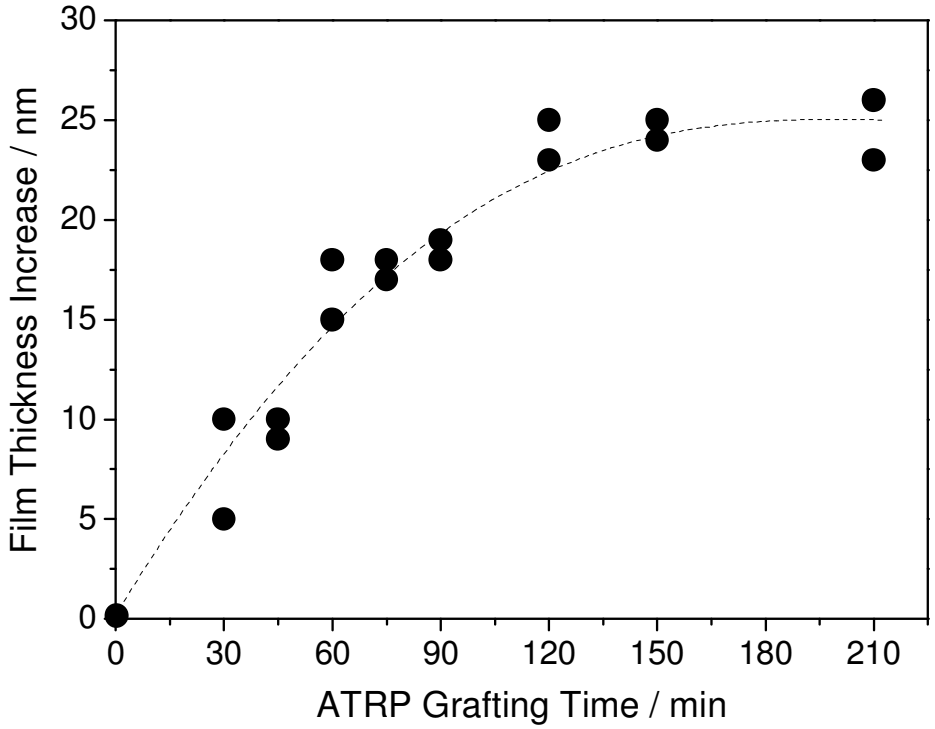

Figure 2.8: Change in polymer film thickness as a function of poly(sodium 4-styrenesulfonate) ATRP grafting time for macroinitiator layers produced by bromoacetic acid derivatisation of poly(glycidyl methacrylate) brushes grafted onto continuous wave plasma deposited poly(vinylbenzyl chloride) films.

2.3.4 Nanotribology

Friction between a sliding SPM probe tip and the polymer brush layers was measured in an aqueous environment as a function of normal load, Figure 2.9. Homogeneous 1 µm x 1 µm regions (rms roughness < 2 nm) were selected for data collection. The plasma deposited poly(vinylbenzyl chloride) layers exhibit a sharp rise in friction at around 130 nN normal load; which is indicative of polymer chain displacement and wear.[87,88] Furthermore, the bottle-brush layers consistently gave lower friction readings compared to poly(glycidyl methacrylate) and poly(sodium 4-styrenesulfonate) brush layers (grafted from the pulsed plasma deposited poly(vinylbenzyl chloride) initiator film). This enhancement can be attributed to steric repulsion and water solvation of the bottle-brushes leading to a resistance towards penetration (and hence improved lubrication).[89,90,91] These tribological experiments were devised in such a way that they use an internal reference – namely the ATRP grafted poly(sodium 4-styrenesulfonate) *brushes* on a pulsed plasma

deposited poly(vinylbenzyl chloride) layer. Therefore, any minor contribution due to negatively charged Coulombic repulsion[92,93] arising from the lowering of pH by dissolution of atmospheric CO_2 into the pure water medium will be present for both the surface ATRP grafted poly(sodium 4-styrenesulfonate) *brushes* and also surface ATRP grafted poly(glycidyl methacrylate)-graft-poly(sodium 4-styrenesulfonate) *bottle-brushes*. By taking this possibility into consideration, the tribology measurements show that the grafted poly(sodium 4-styrenesulfonate) bristles contained in the bottle-brushes display lower friction compared to their linear surface grafted poly(sodium 4-styrenesulfonate) *brush* counterparts.

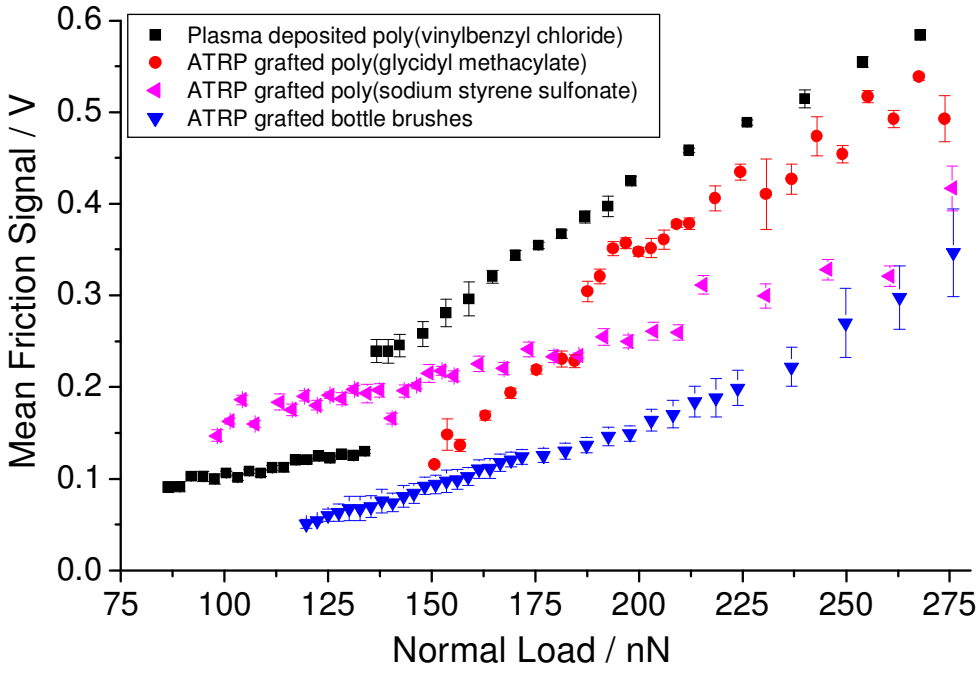

Figure 2.9: Friction signals obtained by lateral force microscopy as a function of normal load for: continuous wave plasma deposited poly(vinylbenzyl chloride) film; ATRP grafted poly(glycidyl methacrylate) on pulsed plasma deposited poly(vinylbenzyl chloride layer); 50 nm thick ATRP grafted poly(sodium 4-styrenesulfonate) brush layer on pulsed plasma deposited poly(vinylbenzyl chloride layer); and 50 nm thick ATRP grafted poly(glycidyl methacrylate)-graft-poly(sodium 4-styrenesulfonate) bottle-brush layer on continuous wave plasma deposited poly(vinylbenzyl chloride layer).

In the case of polymers sliding against solid surfaces, it has been proposed that the variation in friction with shear rate is due to a transition from coiled to stretched conformations,[94] and it is therefore expected that friction for densely grafted polymer brush layers (which already exist in extended conformations under good solvent conditions) will exhibit a low dependence on shear rate. Surface force balance experiments measuring sliding friction between polymer brush layers found only weak velocity dependence[95] and this was also the case for scanning probe friction studies comparing physisorbed versus surface immobilised polyelectrolytes.[96,97] Hence, given that the present bottle-brushes are covalently tethered to the substrate, any variations in friction due to shear rate can be expected to be relatively small.

2.4 DISCUSSION

Pulsed plasma deposited poly(vinylbenzyl chloride) has previously been shown to be a highly effective ATRP initiator.[49] This can be attributed to the stabilised benzyl radicals, which allow chloride abstraction from the benzyl chloride surface functionality to occur easily during ATRP initiation (since benzyl radicals are stabilised by the aromatic ring).[98] Therefore, the structural integrity of benzyl chloride groups within the plasma deposited film governs the effective surface density of ATRP initiation sites. This is evident for the densely crowded poly(glycidyl methacrylate) and poly(sodium 4-styrenesulfonate) brush layers produced by ATRP for the structurally well defined pulsed plasma deposited poly(vinylbenzyl chloride) films. These grow in a controlled fashion with polymer brush thickness increasing linearly, Figures 2.4 and 2.5. In order to lower the surface density of grafted polymer brushes to provide space for side chain (bristle) growth, continuous wave plasma deposited poly(vinylbenzyl chloride) films were shown by infrared and XPS analysis to contain a lower density of intact benzyl chloride initiator groups as a consequence of decreased structural integrity. This difference in density of benzyl chloride initiator sites between continuous wave and pulsed plasma deposited poly(vinylbenzyl chloride) can be explained on the basis of their respective film growth mechanisms. During pulsed plasma deposition, electric discharge modulation consists of a short plasma duty cycle on-period (microseconds) to generate active sites in the gas phase as well as at the growing film surface via VUV irradiation, ion and electron bombardment, followed by conventional carbon-carbon double bond polymerization processes proceeding throughout each accompanying extended pulse off-period (milliseconds) in the absence of any UV, ion, or electron-induced damage to the growing film.[79,99] Such conventional polymerization pathways are strongly perturbed during continuous wave plasma conditions, where the multitude of reactions for radicals, ions and excited species contained within the electrical discharge play a greater role leading to structural disruption. Furthermore, the average power supplied to the vinylbenzyl chloride precursor vapour during continuous wave plasma discharge (30 W) was significantly greater in comparison to pulsed plasma deposition (0.7 W).

As a consequence, the thickness of the ATRP grafted poly(glycidyl methacrylate) layers measured for the continuous wave deposited poly(vinylbenzyl chloride) films is considerably lowered in comparison to those prepared using pulsed plasma conditions. Given the identical ATRP conditions, the grafted poly(glycidyl methacrylate) brushes can be considered to be comparable in length between the pulsed and continuous wave plasma deposited initiator nanofilms, and therefore the lower film thickness in the latter case can be attributed to the collapsed conformation of poly(glycidyl methacrylate) chains, stemming from the lower surface initiator site density.

Subsequent exposure to bromoacetic acid of the aforementioned surface tethered poly(glycidyl methacrylate) brushes yields well-defined surface immobilised macroinitiator species. This approach follows previously reported solution phase macroinitiator brush syntheses as precursors for bottle-brushes based on the esterification of pendant hydroxyl groups of poly(hydroxyethyl methacrylate) backbone polymers.[6,20,100] In the present study, the epoxide functionalities contained within poly(glycidyl methacrylate) brushes provide a more reactive handle for esterification with bromoacetic acid vapour, Scheme 2.1, Table 2.1, and Figure 2.3.

Characterisation of surface immobilised bottle-brush polymers is challenging. One approach is to analyse polymers formed in solution alongside the sample via the introduction of sacrificial initiator species. However, this fails to address the issues unique to surface tethering such as steric crowding.[43] In the present study, the sulfonate groups of poly(sodium 4-styrenesulfonate) side chains (bristles), provide strong characteristic infrared absorbances which follow the increase in film thickness, Figures 2.7 and 2.8. The absence of both these trends when initiator bromide groups were not present along the poly(glycidyl methacrylate) brush backbone (via esterification with acetic acid instead of bromoacetic acid, Scheme 2.1) verifies that poly(sodium 4-styrenesulfonate) chains (bristles) form only when initiator sites are present along the polymer brush.

In the present study, the surface tethered bottle-brushes investigated are found to display even lower friction when compared to their constituent linear polymer brush counterparts. This behaviour can be attributed to the former being more compact (and hydrated) as described in earlier reports

relating to enhanced lubrication by similar hydrophilic bottle-brush polymers which had been physisorbed onto substrates,[10] and also low asymmetric friction measurements observed for polyelectrolyte brushes.[101,102] Grafting of side chains from the polymer backbone to form bottle-brush structures can be expected to increase macromolecular rigidity,[103,104] in particular in the case of polyelectrolyte brushes, where, in comparison to neutral hydrophilic brushes, surface grafted polyelectrolyte brushes are stretched due to the osmotic pressure provided by condensed counter-ions.[105,106,107] The dry heights of the poly(sodium 4-styrenesulfonate) brush and bottle-brush layers used for the scanning probe friction measurements were both kept the same (50 nm, Figure 2.9). XPS analysis shows a lower amount of sulphur at the surface for poly(sodium 4-styrenesulfonate) bottle-brush bristles compared to brush layers (3 ± 1 % versus 7 ± 1 % respectively, Table 2.1); which indicates a lower counter-ion density, thereby negating the idea that the reduced friction is due to an increased number of counter-ions per unit area. Therefore the decreased friction is related to the molecular geometry (linear versus bottle brush).

The overall sequential controlled polymerization approach is key to the formation of well-defined macroinitiator brushes and the subsequent synthesis of the bottle-brush bristles. By contrast, the lack of control associated with conventional polymerization initiators leads to ill-defined macroinitiator brushes and side chains.[108] Given the inherent control afforded over macromolecular architecture, surface tethered well-defined bottle-brush polymers prepared by ATRP are an attractive prospect for the development of novel surface properties, such as lubricity. Tailoring of both the backbone and bristle segments can be achieved using the 'grafting *from*' approach; furthermore, the surface density of backbone grafts can also be independently controlled using plasmachemical deposition of initiator sites in order to allow predetermined side chain (bristle) growth.[38,43] The key merits of the present approach relate to the substrate-independent covalent anchoring of the bottle-brushes to the surface, which offers scope for far more widespread applicability than their physisorbed counterparts. Potential applications of such surface tethered bottle-brushes could include actuators, sensors, building blocks for nanostructures, templates for producing metallic nanowires, as well

as mimicking biomolecules possessing bottle-brush architectures for performing biological lubrication (such as proteoglycans[109] and epithelial tethered mucins[110,111]).

2.5 CONCLUSIONS

Surface tethered polymer bottle-brushes have been produced by ATRP from plasmachemical deposited initiator layers. The surface density of ATRP initiator sites can be tailored by variation of plasma deposition parameters. This in turn allows the space surrounding surface immobilised backbone macroinitiators to be controlled, allowing the outward growth of polymer brush side chains (bristles). Lateral force scanning probe microscopy has shown that poly(glycidyl methacrylate)-graft-poly(sodium 4-styrenesulfonate) bottle-brush decorated surfaces give rise to an enhancement in lubrication.

2.6 REFERENCES

(1) Gallyamov, M. O.; Tartsch, B.; Potemkin, I. I.; Börner, H. G.; Matyjaszewski, K.; Khokhlov, A. R.; Möller, M. *Eur. Phys. J. E* **2009**, *29*, 73.

(2) Rathgeber, S.; Lee, H.; Matyjaszewski, K.; Di Cola, E. *Macromolecules* **2007**, *40*, 7680.

(3) Xu, H.; Sun, F. C.; Shirvanyants, D. G.; Rubinstein, M.; Shabratov, D.; Beers, K. L.; Matyjaszewski, K.; Sheiko, S. S. *Adv. Mater.* **2007**, *19*, 2930.

(4) Börner, H. G.; Beers, K.; Matyjaszewski, K.; Sheiko, S. S.; Möller, M. *Macromolecules* **2001**, *34*, 4375.

(5) Djalali, R.; Li, S. Y.; Schmidt, M. *Macromolecules* **2002**, *35*, 4282.

(6) Cheng, G.; Böker, A.; Zhang, M.; Krausch, G.; Müller, A. H. E. *Macromolecules* **2001**, *34*, 6883.

(7) Iwasaki, Y.; Akiyoshi, K. *Macromolecules* **2004**, *37*, 7637.

(8) Matyjaszewski, K.; Tsarevsky, N. V. *Nat. Chem*. **2009**, *1*, 276.

(9) Park, I.; Sheiko, S. S.; Nese, A.; Matyjaszewski, K. *Macromolecules* **2009**, *42*, 1805.

(10) Chen, M.; Briscoe, W. H.; Armes, S. P.; Klein, J. *Science* **2009**, *323*, 1698.

(11) Pettersson, T.; Naderi, A.; Makuška, R.; Claesson, P. M. *Langmuir* **2008**, *24*, 3336.

(12) Durmaz, Y. Y.; Kumbaraci, V.; Demirel, A. L.; Talinli, N.; Yagci, Y.; *Macromolecules* **2009**, *42*, 3743.

(13) Tang, H.; Li, Y.; Lahasky, S. H.; Sheiko, S. S.; Zhang, D. *Macromolecules* **2011**, *44*, 1491.

(14) Gao, H.; Matyjaszewski, K. *J. Am. Chem. Soc.* **2007**, *129*, 6633.

(15) Naderi, A.; Iruthayaraj, J.; Vareikis, A.; Makuška, R., Claesson, P. M. *Langmuir* **2007**, *23*, 12222.

(16) Iruthayaraj, J.; Olanya, G.; Claesson, P. M. *J. Phys. Chem. C* **2008**, *112*, 15028.

(17) Vogt, A. P.; Sumerlin, B. S. *Macromolecules* **2006**, *39,* 5286.

(18) Zhai, G.; Kang, E. T.; Neoh, K. G. *Macromolecules* **2004**, *37*, 7240.

(19) Tasdelen, M. A.; Yagci, Y.; Demirel, A. L.; Biedron, T.; Kubisa, P. *Polym. Bull.* **2007**, *58*, 653.

(20) Tang, C.; Dufour, B.; Kowalewski, T.; Matyjaszewski, K. *Macromolecules* **2007**, *40*, 6199.

(21) Yu, W. H; Kang, E. T.; Neoh, K. G. *Langmuir* **2005**, *21*, 450.

(22) Edmondson, S.; Osborne, V. L.; Huck, W. T. S. *Chem. Soc. Rev.* **2004**, *33*, 14.

(23) Bontempo, D.; Tirelli, N.; Feldman, K.; Masci, G.; Crescenzi, V.; Hubbell, J. A. *Adv. Mater.* **2002**, *14*, 1239.

(24) Gonzalez-Leon, J. A.; Acar, M. H.; Ryu, S.-W.; Ruzette, A.-V. G.; Mayes, A. M. *Nature* **2003**, *426*, 424.

(25) Kong, H.; Gao, C.; Yan, D. *J. Am. Chem. Soc.* **2004**, *126*, 412.

(26) Kowalewski, T.; Tsarevsky, N. V.; Matyjaszewski, K. *J. Am. Chem. Soc.* **2002**, *124*, 10632.

(27) Gao, X.; Zhu, S.; Sheardown, H.; Brash, J. L. *Polymer* **2010**, *51*, 1771.

(28) Jennings, G. K.; Brantley, E. L. *Adv. Mater.* **2004**, *16*, 1983.

(29) Jonas, A. M.; Glinel, K.; Oren, R.; Nysten, B.; Huck, W. T. S. *Macromolecules* **2007**, *40*, 4403.

(30) Wang, X.; Tu, H.; Braun, P. V.; Bohn, P. W. *Langmuir* **2006**, *22*, 817.

(31) Tang, X. D.; Han, N. F.; Zhou, D. J. *Adv. Mater. Res*. **2010**, *87*, 36.

(32) Li, D.; Sheng, X.; Zhao, B. *J. Am. Chem. Soc.* **2005**, *127*, 6248.

(33) Zhao, B.; Haasch, R. T.; MacLaren S. *J. Am. Chem. Soc.* **2004**, *126*, 6124.

(34) von Werne, T.; Patten, T. E. *J. Am. Chem. Soc.* **2001**, *123,* 7497.

(35) Mulvihill, M. J.; Rupert, B. L.; He, R.; Hochbaum, A.; Arnold, J.; Yang, P. *J. Am. Chem. Soc.* **2005**, *127*, 16040.

(36) Kim, J.-B.; Bruening, M. L.; Baker, G. L. *J. Am. Chem. Soc.* **2000**, *122,* 7616.

(37) Ma, H.; Hyun, J.; Stiller, P.; Chilkoti, A. *Adv. Mater.* **2004**, *16*, 338.

(38) Feng, W.; Zhu, S.; Ishihara, K.; Brash, J. L. *Biointerphases* **2006**, *1*, 50.

(39) Sheiko, S. S.; Sun, F. C.; Randall, A.; Shirvanyants, D.; Rubinstein, M.; Lee, H.; Matyjaszewski, K. *Nature* **2006**, *440*, 191.

(40) Olanya, G.; Iruthayaraj, J.; Poptoshev, E.; Makuška, R.; Vareikis, A.;

Claesson, P. M. *Langmuir* **2008**, 24, 5341.

(41) Feuz, L.; Leermakers, F. A. M.; Textor, M.; Borisov, O. *Langmuir* **2008**, *24*, 7232.

(42) Naderi, A.; Iruthayaraj, J.; Pettersson, T.; Makuška, R.; Claesson, P. M. *Langmuir* **2008**, *24*, 6676.

(43) Pietrasik, J.; Cusick, B.; Kowalewski, T.; Matyjaszewski, K. *Polym. Prepr.* **2005**, *46,* 335.

(44) Lee, M.-T.; Hsueh, C.-C.; Freund, M. S.; Ferguson, G. S. *Langmuir* **1998**, *14,* 6419.

(45) Tang, Z.; Wang, Y.; Podsiadlo, P.; Kotov, N. A. *Adv. Mater.* **2006**, *18*, 3203.

(46) Hancer, M. *Prog. Org. Coat.* **2008**, *63*, 395.

(47) Ulman, A. *Chem. Rev.* **1996**, *96*, 1533.

(48) Wang, M.; Liechti, K. M.; Wang, Q.; White, J. M. *Langmuir* **2005**, *21*, 1848.

(49) Teare, D. O. H.; Barwick, D. C.; Schofield, W. C. E.; Garrod, R. P.; Ward, L. J.; Badyal, J. P. S. *Langmuir* **2005**, *21*, 11425.

(50) Schelz, S.; Oelhafen, P. *Surf. Sci.* **1992**, *279*, 137.

(51) Schelz, S.; Reinke, P.; Oelhafen, P. *Surf. Sci.* **1993**, *293*, 275.

(52) Grill, A. *Cold Plasma in Materials Fabrication: From Fundamentals to Applications*, IEEE Press: Piscataway, NJ, USA, 1994; p 65.

(53) Ehrlich, C. D.; Basford J. A. *J. Vac. Sci. Technol., A* **1992**, *10,* 1.

(54) Tsarevsky, N. V.; Pintauer, T.; Matyjaszewski, K. *Macromolecules* **2004**, *37*, 9768.

(55) Lovering, D. *NKD-6000 Technical Manual*; Aquila Instruments: Cambridge, U.K. 1998.

(56) Haugstad, G.; Gladfelter, W. L.; Weberg, E. B.; Weberg, R. T.; Jones, R. R. *Langmuir* **1995**, *11*, 3473.

(57) Hammerschmidt, J. A.; Moasser, B.; Gladfelter, W. L.; Haugstad, G.; Jones, R. R. *Macromolecules* **1996**, *29*, 8996.

(58) Koszewski, A.; Rymuza, Z.; Reuther, F. *Microelectron. Eng.* **2008**, *85*, 1189.

(59) Bistac, S.; Schmitt, M.; Ghorbal, A.; Gnecco, E.; Meyer, E. *Polymer*

2008, *49,* 3780.

(60) Sahoo, R. R.; Biswas, S. K. *J. Colloid Interface Sci.* **2009**, *333*, 707.

(61) Perry, S. S.; Yan, X.; Limpoco, F. T.; Lee, S.; Müller, M.; Spencer, N. D. *ACS Appl. Mater. Interface*s **2009**, *1*, 1224.

(62) Pettersson, T.; Nordgren, N.; Rutland, M. W.; Feiler, A. *Rev. Sci. Instrum.* **2007**, *78*, 093702.

(63) Koinkar, V. N.; Bhushan, B. *J. Appl. Phys*. **1997**, *81*, 2472.

(64) Bhushan, B.; Kulkarni, A. V. *Thin Solid Films* **1996**, *278*, 49.

(65) Enachescu, M.; van den Oetelaar, R. J. A.; Carpick, R. W.; Ogletree, D. F.; Flipse, C. F. J.; Salmeron, M. *Tribol. Lett.* **1999**, *7*, 73.

(66) Moulder, J. F.; Stickle, W. F.; Sobol, P. E.; Bomben, K. D. *Handbook of X-Ray Photoelectron Spectroscopy: A Reference Book of Standard Spectra for Identification and Interpretation of XPS Data*; Perkin-Elmer Corp.: Eden Prarie, MN, 1992.

(67) Lin-Vien, D.; Colthrup, N. B.; Fateley, W. G.; Grasselli, J. G. *The Handbook of Infrared and Raman Characteristic Frequencies of Organic Molecules*; Academic Press: Boston, 1991.

(68) Tarducci, C.; Kinmond, E. J.; Badyal, J. P. S.; Brewer, S. A.; Willis, C. *Chem. Mater.* **2000**, *12*, 1884.

(69) Morsch, S.; Schofield, W. C. E.; Badyal, J. P. S. *Langmuir* **2010**, 26, 12342.

(70) Matyjaszewski, K.; Xia, J. *Chem. Rev.* **2001**, *101,* 2921.

(71) Jones, D. M.; Brown, A. A.; Huck, W. T. S. *Langmuir* **2002**, *18*, 1265.

(72) Yu, W. H.; Kang, E. T.; Neoh, K. G. *Langmuir* **2004**, *20,* 8294.

(73) Xu, F. J.; Cai, Q. J.; Li, Y. L.; Kang, E. T.; Neoh, K. G. *Biomacromolecules* **2005**, *6*, 1012.

(74) Edmondson, S.; Huck, W. T. S. *J. Mater. Chem.* **2004**, *14*, 730.

(75) Krishnan, R.; Srinivasan, K. S. V. *Macromolecules* **2004**, *37*, 3614.

(76) Odian, G. G. *Principles of Polymerization*; John Wiley & Sons: New York, 2004; p 226.

(77) van Poll, M. L.; Khodabakhsh, S.; Brewer, P. J.; Shard, A G.; Ramstedt, M.; Huck, W. T. S. *Soft Matter* **2009**, *5*, 2286.

(78) Motornov, M.; Minko, S.; Nitschke, M.; Grundke, K.; Stamm, M. *Poly.*

Mater.: Sci. Eng. **2003**, *88*, 264.

(79) Ryan, M. E.; Hynes, A. M.; Badyal, J. P. S. *Chem. Mater.* **1996**, *8*, 37.

(80) Osborne, V. L.; Jones, D. M.; Huck, W. T. S. *Chem. Commun.* **2002**, *17*, 1838.

(81) Tugulu, S.; Barbey, R.; Harms, M.; Fricke, M.; Volkmer, D.; Rossi, A.; Klok; H.-A. *Macromolecules* **2007**, *40*, 168.

(82) Iddon, P. D.; Robinson, K. L.; Armes, S. P. *Polymer* **2004**, *45*, 759.

(83) Miller, M. D.; Baker, G. L.; Bruening, M. L. *J. Chromatogr. A* **2004**, *1044*, 323.

(84) Moreno, J.; Sherrington, D. C. *Chem. Mater.* **2008**, *20,* 4468.

(85) Wang, J.-Y.; Chen, W.; Liu, A.-H.; Lu, G.; Zhang, G.; Zhang, J.-H.; Yang, B. *J. Am. Chem. Soc.* **2002**, *124*, 13358.

(86) Robinson, K. L.; Weaver, J. V. M.; Armes, S. P.; Marti, E. D.; Meldrum, F. C. *J. Mater. Chem.* **2002**, *12*, 890.

(87) Zhang, L.; Li, L.; Chen, S.; Jiang, S. *Langmuir* **2002**, *18*, 5448.

(88) Ren, S. L.; Yang, S. R.; Zhao, Y. P. *Appl. Surf. Sci.* **2004**, *227*, 293.

(89) Gong, J. P. *Soft Matter* **2006**, *2*, 544.

(90) Lee, S.; Spencer, N. D. *Science* **2008**, *319*, 575.

(91) Klein, J.; Kumacheva, E.; Mahalu, D.; Perahia, D.; Fetters, L. J. *Nature* **1994**, *370*, 634.

(92) Zhu, Y. Y.; Kelsall, G. H; Spikes, H. A. *Tribol. Trans.* **1994**, *37*, 811.

(93) Hähner, G.; Marti, A.; Spencer, N. D. *Tribol. Lett.* **1997**, *3*, 359.

(94) Brochard, F.; de Gennes, P. J. *Langmuir* **1992**, *8*, 3033.

(95) Tadmor, R.; Janik, J.; Klein, J.; Fetters, L. J. *Phys. Rev. Lett.* **2003**, *91*, 115503.

(96) Plunkett, M. A.; Feiler, A.; Rutland, M. W. *Langmuir* **2003**, *19,* 4180.

(97) Feiler, A.; Plunkett, M. A.; Rutland, M. W. *Langmuir* **2003**, *19,* 4173.

(98) Clayden, J.; Greeves, N.; Warren, S.; Worthers, P. *Organic Chemistry;* Oxford University Press: Oxford, U.K., 2001; p 1026.

(99) Badyal, J. P. S. *Chem. Brit.* **2001**, *37*, 45.

(100) Matyjaszewski, K.; Qin, S.; Boyce, J. R.; Shirvanyants, D.; Sheiko, S. S. *Macromolecules* **2003**, *36*, 1843.

(101) Zhang, Z.; Morse, A. J.; Armes, S. P.; Lewis, A. L.; Geoghegan, M.; Leggett, G. J. *Langmuir* **2011**, *27*, 2514.

(102) Kampf, N.; Gohy, J.-F.; Jérôme, R.; Klein, J. *J. Polym. Sci., Part B* **2005**, *43*, 193.

(103) Rathgeber, S.; Pakula, T.; Wilk, A.; Matyjaszewski, K.; Beers, K. L. *J. Chem. Phys*. **2005**, *122*, 124904.

(104) Zhang, B.; Gröhn, F.; Pedersen, J. S.; Fischer, K.; Schmidt, M. *Macromolecules* **2006**, *39*, 8440.

(105) Raviv, U.; Giasson, S.; Kampf, N.; Gohy, J.-F.; Jérôme, R.; Klein, J. *Nature* **2003**, *425*, 163.

(106) Liberelle, B.; Giasson, S. *Langmuir* **2008**, *24*, 1550.

(107) Heeb, R.; Bielecki, R. M.; Lee, S.; Spencer, N. D. *Macromolecules* **2009**, *42*, 9124.

(108) Chabrecek, P.; Lohmann, D. *US Patent* 6,465,056 B1, October 15, 2002.

(109) Klein, J. *Science* **2009**, *323*, 47.

(110) Hattrup, C. L.; Gendler, S. J. *Annu. Rev. Physiol.* **2008**, *70*, 431.

(111) Yakubov, G. E.; McColl, J.; Bongaerts, J. H. H.; Ramsden, J. J. *Langmuir* **2009**, *25,* 2313.

CHAPTER 3

NANOPATTERNED POLYMER BRUSHES

3.1 INTRODUCTION

Micro- and nanoscale-patterned polymer structures are of key importance for the development of multifunctional surfaces sought in fields such as regulated cell growth,[1,2,3] proteomics,[4,5,6] fluidics,[7,8,9] and biosensors.[10,11,12]

By combining surface initiated ATRP with lithographic techniques, there is scope for the fabrication of multifunctional surfaces, where patterning of the initiator species determines the eventual polymer brush positioning. The most widely reported variants include micro-contact printing of initiator bearing SAMs,[13,14,15,16,17] UV irradiation through masks,[18] electron beam patterning,[19,20,21] photolithography,[1,22,23] and microcontact moulding.[24] Surprisingly, few attempts have been made to try to combine surface-initiated ATRP with scanning probe lithography. Scanning electrochemical microscopy is one example where the localised reduction of ATRP initiator moieties has been used to generate micropatterned poly(styrene) and poly(glycidyl methacrylate) brushes.[25,26] Also, there has been nanoshaving of silane initiator SAMs followed by surface initiated ATRP to produce line widths ranging from 300 nm to 500 nm of poly(*N*-isopropylacrylamide).[27] An alternative SAM approach entailed dip-pen nanolithography of thiol bearing initiator spots patterned by onto gold, followed by grafting to yield 90-nm-diameter poly(oligo(ethylene glycol) methyl ether methacrylate) polymer islands.[28] Although these studies represent significant advances in the field, their inherent substrate dependency places a severe limitation on more widespread applicability.

The aforementioned drawbacks can be addressed by adopting the molecular scratchcard lithographic technique.[29,30,31,32] It entails plasmachemical bilayering, followed by selective puncturing of the upper nanolayer using a scanning probe tip. This approach circumvents any issues relating to substrate specificity; for instance pulsed plasma deposited poly(vinylbenzyl chloride) initiator layers have been successfully used in the past for the growth of ATRP polymer brushes onto a variety of substrate materials and geometries.[33]

In this study, pulsed plasmachemical bilayer stacks are fabricated comprising a poly(vinylbenzyl chloride) ATRP initiator base layer which, in keeping with the established molecular scratchcard methodology, is covered

with a protein-resistant[34] poly(*N*-acryloylsarcosine methyl ester) resist layer.[29,32] Scanning probe lithography is then selectively employed to expose the underlying halide initiator functionalities, which readily undergo localised ATRP to yield nanoscale polymer brush features, Scheme 3.1. The inherent functional background provided by this method (e.g., protein resistance) circumvents the commonly required additional step of subsequent back filling with SAMs or sequential polymerizations.[14,35]

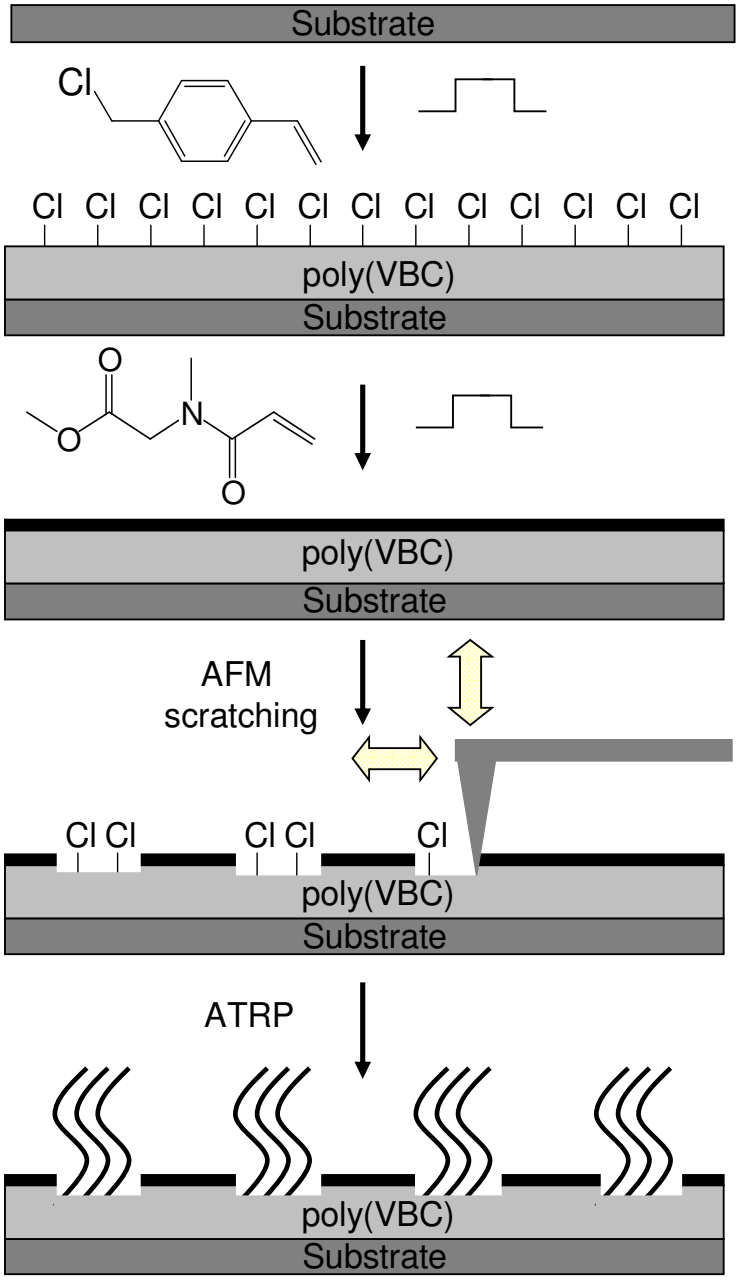

Scheme 3.1: Pulsed plasmachemical deposition of poly(vinylbenzyl chloride) / poly(*N*-acryloylsarcosine methyl ester) bilayer molecular scratchcards, followed by scanning probe lithography, and finally ATRP of methyl methacrylate to create nanoscale polymer brush structures.

3.2 EXPERIMENTAL

3.2.1 Pulsed Plasmachemical Nanolayering

Plasma depositions were performed according to the methodology outlined in Chapter 2, Section 2.2.1, using the deposition parameters given in Table 3.1. A temperature-controlled oven was employed in the case of poly(*N*-acryloylsarcosine methyl ester).

Table 3.1: Pulsed plasma deposition parameters yielding high levels of precursor structural retention[33,34] (peak power = 30 W) (error values are one stadard deviation).

Precursor	***Reactor Temperature*** *(°C)*	***Pulse duty cycle*** *(μs)*		***Deposition rate*** *(nm min^{-1})*
		Time on	*Time off*	
4-Vinylbenzyl chloride (+97%, Aldrich)	22	100	4,000	191 ± 17
N-acryloylsarcosine methyl ester (+97%, Lancaster)	40	20	5,000	3.5 ± 0.3

3.2.2 Molecular Scratchcard Lithography

For bilayer fabrication, 1 cm^2 silicon wafer pieces were coated with 100 nm of pulsed plasma deposited poly(vinylbenzyl chloride) initiator layer followed by immediate overcoating with 20 nm of a pulsed plasma poly(*N*-acryloylsarcosine methyl ester) barrier layer. Subsequent nanoscale patterning entailed mounting these samples onto an atomic force microscope stage (Digital Instruments Nanoscope III) followed by selective puncturing of the upper layer to expose underlying poly(vinylbenzyl chloride) initiator sites by scanning a tapping-mode tip (Nanoprobe, spring constant 42-83 Nm^{-1}) in contact mode. Tip movement in the *x*, *y*, and *z* planes was controlled using Veeco Nanolithography Software (version 5.30r1).

3.2.3 Surface Initiated ATRP

ATRP initiator-functionalised substrates were loaded into a sealable glass tube containing 5 mmol copper (I) bromide (+98 %, Aldrich), 0.1 mmol copper (II) bromide (+99 %, Aldrich), 10 mmol 2,2'-bipyridyl (+99 %, Aldrich), 0.05 mol methyl methacrylate (+99 %, Aldrich), and 4 mL *N,N*-dimethylformamide

(+99.9 %, Fisher), Scheme 3.2. The mixture was thoroughly degassed using freeze-pump-thaw cycles and then immersed into an oil bath maintained at 80 °C for a range of grafting times (1 – 20 h). Final cleaning and removal of any physisorbed polymer was achieved by Soxhlet extraction using hot toluene for at least 16 h.

ATRP of poly(glycidyl methacrylate) was performed in a similar manner to that described above, using instead a reaction mixture comprising 5 mmol copper (I) bromide, 1 mmol copper (II) bromide, 10 mmol 2,2'-bipyridyl, 0.05 mol glycidyl methacrylate (+97 %, Aldrich), and 4 mL *N,N*-dimethylformamide. Subsequent fluorescent tagging of patterned poly(glycidyl methacrylate) epoxide centers was achieved by brief submersion into a 1 mg dm^{-3} aqueous solution of Alexafluor 350 Cadaverine dye (Invitrogen), followed by extensive rinsing with high-purity water, and then a second Soxhlet extraction in hot toluene.

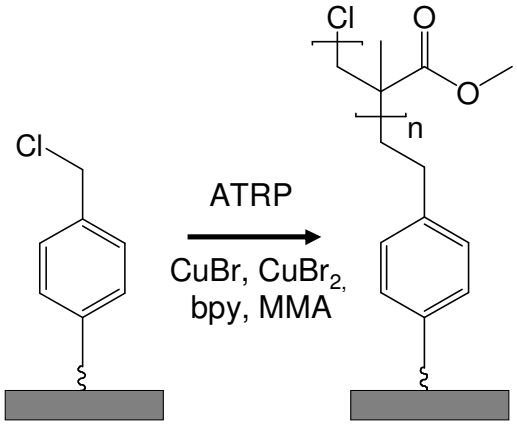

Scheme 3.2: ATRP grafting of poly(methyl methacrylate) brushes onto pulsed plasma-deposited poly(vinylbenzyl chloride) initiator layer.

3.2.4 Film Characterisation

Film thickness, infrared spectra and XPS elemental compositions were measured as described in Chapter 2, Section 2.2.3.

Atomic force microscopy images were collected in tapping mode at 20 °C in ambient air (Digital Instruments Nanoscope III). The tapping mode tip had a spring constant of 42 - 83 N m^{-1}(Nanoprobe).

Fluorescence microscopy was performed using an Olympus IX-70 system (DeltaVision RT, Applied Precision, WA). Images were collected using

an excitation wavelength of 360 nm corresponding to the absorption maximum of the Alexafluor 350 Cadaverine dye molecule.

Sessile drop contact angle measurements were made at 20 °C using a video capture apparatus (A.S.T. Products VCA 2500 XE) and 2 µL of high purity water droplets (BS 3978 Grade 1).

3.3 RESULTS

3.3.1 Surface Initiated ATRP of Poly(methyl methacrylate)

Analysis of the pulsed plasma deposited poly(vinylbenzyl chloride) ATRP initiator layers yielded XPS elemental compositions and infrared spectroscopy fingerprint absorbances identical to those reported in Chapter 2, Table 3.2 and Figure 3.1.

Table 3.2: XPS elemental compositions of pulsed plasma deposited nanolayers, and poly(methyl methacrylate) ATRP grafted onto pulsed plasma deposited poly(vinylbenzyl chloride) surfaces (error values are one standard deviation).

Surface		***XPS Elemental Composition***			
		C %	***O %***	***N %***	***Cl %***
Pulsed plasma deposited poly(vinylbenzyl chloride)	*Theoretical*	90	0	0	10
	Actual	90 ± 1	0	0	10 ± 1
Pulsed plasma deposited poly(N-acryloylsarcosine methyl ester)	*Theoretical*	64	27	9	0
	Actual	63 ± 1	28 ± 1	9 ± 1	0
ATRP grafted poly(methyl methacrylate)	*Theoretical*	71	29	0	0
	Actual	70 ± 2	30 ± 2	0	0

ATRP grafted poly(methyl methacrylate) brushes grown from pulsed plasma deposited poly(vinylbenzyl chloride) ATRP initiator layers gave rise to XPS elemental compositions which are in good agreement with the calculated theoretical composition for poly(methyl methacrylate), Table 3.2 and Scheme 3.2. In addition, no chlorine was detectable, thereby confirming complete coverage of the poly(vinylbenzyl chloride) initiator film by the ATRP grafted polymer brushes. Characteristic infrared absorbances for both the methyl methacrylate monomer and ATRP grafted poly(methyl methacrylate) include the ester carbonyl C=O stretch at 1740 cm^{-1} and C-O-C bending at 1170 cm^{-1}, Figure 3.1. Loss of the monomer vinyl double bond peaks at 1635 cm^{-1} (C=C stretch) and 937 cm^{-1} (vinyl CH_2 wag) provide further evidence of ATRP having taken place.[36]

The controlled nature of ATRP polymer brush growth on pulsed plasma deposited poly(vinylbenzyl chloride) initiator layers was verified by monitoring the increase in poly(methyl methacrylate) layer thickness versus grafting time, Figure 3.2. A linear correlation was observed, corresponding to a growth rate of 23 ± 3 nm h^{-1}. Although each point in Figure 3.2 corresponds to only one experiment, the rate is in keeping with that previously reported for ATRP grafting of poly(methyl methacrylate) onto pulsed plasma deposited poly(vinylbenzyl chloride) layers.[33] Whilst this is fast in comparison to other reports of surface initiated ATRP of poly(methyl methacrylate) in organic solvents (e.g., 9 nm h^{-1} in diphenyl ether at 90 °C[37]), it is comparable to the rate reported using a methanol/water solvent alongside low ratios of $CuCl_2$:CuCl based catalytic complexes (approximately 20 nm h^{-1}).[38] Furthermore, rates of up to 250 nm h^{-1} have been reported for the ATRP of poly(methyl methacrylate) using very active 1,4,8,11-tetramethyl-1,4,8,11-tetraazacyclotetradecane (Me_4cyclam) complexes in anisole/*N,N*-dimethylformamide solvent mixtures.[39] As discussed in Chapter 2 Part 2.3.2, an enhanced polymerization rate in the present study may be related to water in the *N,N*-dimethylformamide solvent used, or else the polymeric nature of the pulsed plasma deposited poly(vinylbenzyl chloride) initiator layer.

Surprisingly, unlike in the case of poly(glycidyl methacrylate) ATRP described in Chapter 2, no slowing of the polymerization rate was observed for up to 20 h of reaction time, whereupon polymer brush film thickness had reached 500 nm (very thick), signifying a steady rate of growth and a negligible contribution from polymerization termination reactions. The omission of catalytic copper species from the reaction mixture under otherwise identical conditions produced no detectable poly(methyl methacrylate) grafting after 4 h, precluding auto-polymerization as an alternative explanation for the reported observations.[40]

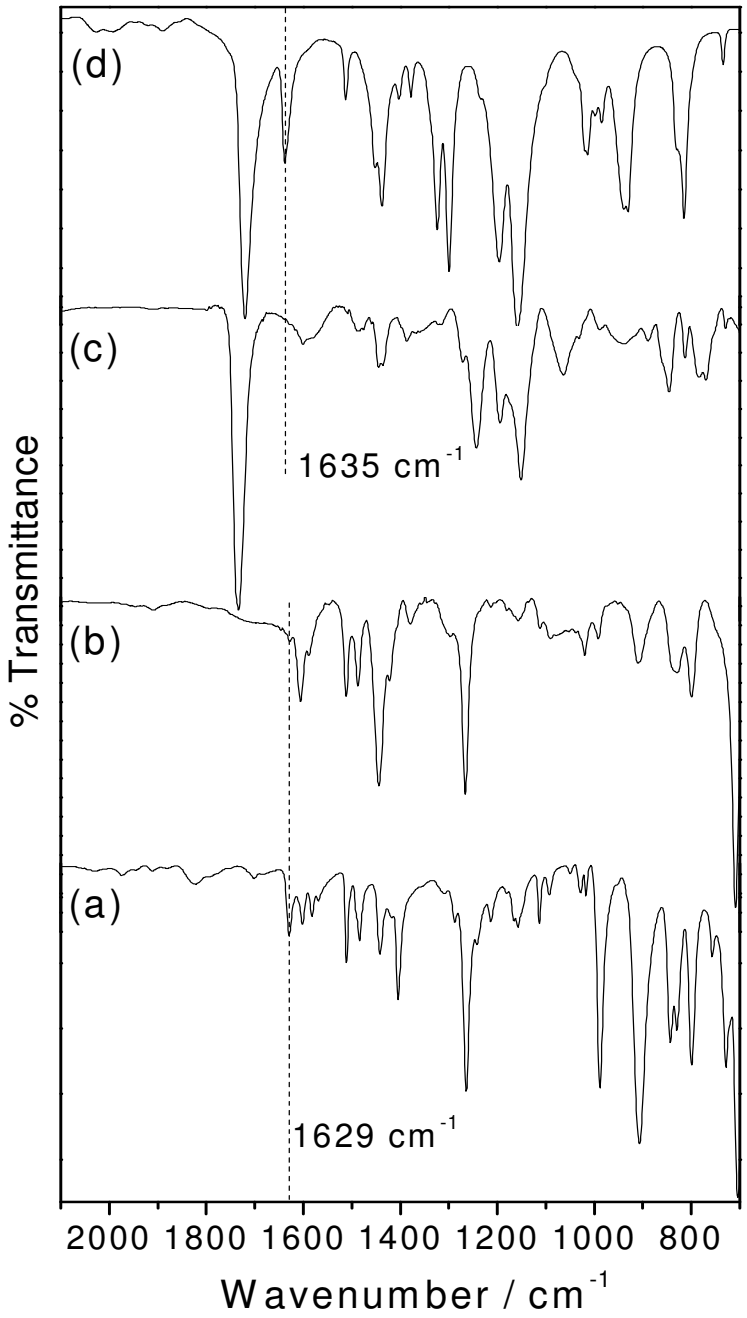

Figure 3.1: Infrared spectra of: (a) the vinylbenzyl chloride monomer; (b) pulsed plasma deposited poly(vinylbenzyl chloride) ATRP initiator layer; (c) ATRP grafted poly(methyl methacrylate) brushes on 100 nm pulsed plasma deposited poly(vinylbenzyl chloride); and (d) the methyl methacrylate monomer.

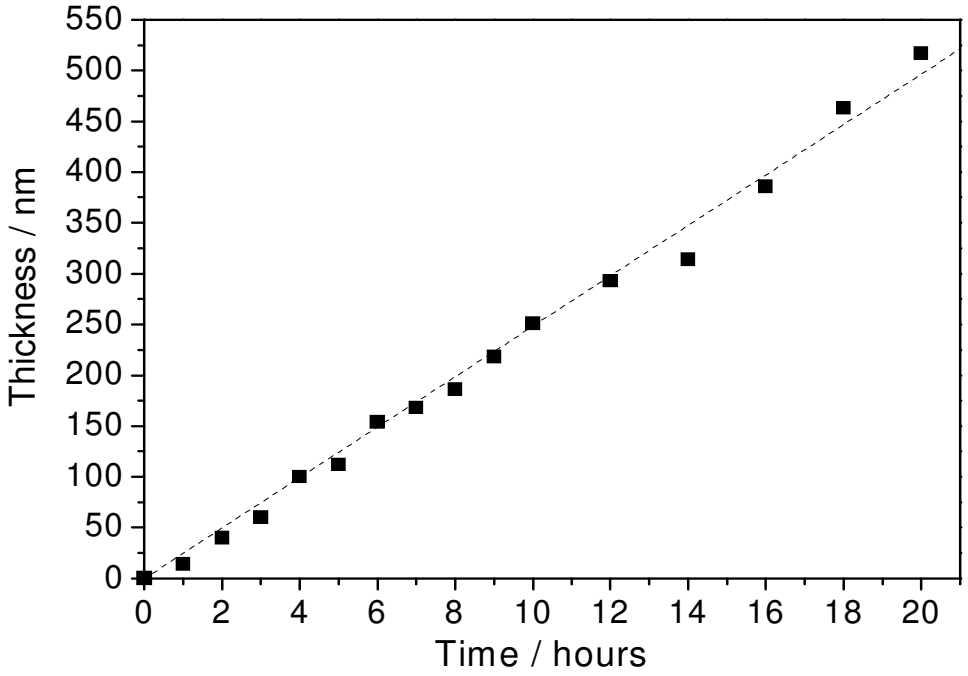

Figure 3.2: Variation of poly(methyl methacrylate) film thickness as a function of ATRP grafting time onto 100 nm pulsed plasma deposited poly(vinylbenzyl chloride) initiator layer.

3.3.2 Bilayer Molecular Scratchcards

Pulsed plasma deposited bilayer stacks comprising 100 nm poly(vinylbenzyl chloride) ATRP initiator base film covered with a 20 nm poly(*N*-acryloylsarcosine methyl ester) barrier layer were characterised by XPS and infrared spectroscopies. XPS analysis yielded identical elemental compositions to those obtained for pulsed plasma deposited poly(*N*-acryloylsarcosine methyl ester), Table 3.2. Infrared absorbances associated with the 20 nm thick poly(*N*-acryloylsarcosine methyl ester) top layer include 1739 cm^{-1} (carbonyl ester stretch) and 1644 cm^{-1} (carbonyl amide stretch),[34,36] Figure 3.3. Retention of chloride functionality for the underlying pulsed plasma deposited poly(vinylbenzyl chloride) layer was evident by the infrared peak at 1263 cm^{-1} (CH_2 wag on CH_2-Cl).

Control experiments to verify that poly(*N*-acryloylsarcosine methyl ester) behaves as an effective barrier layer entailed exposing the bilayer samples to methyl methacrylate monomer under ATRP conditions for 4 h, where no polymer growth was measured. Furthermore, no warping or swelling of such samples was observed by AFM or spectral reflectance, thereby

demonstrating the thermal and chemical stabilities of the fabricated molecular scratchcard bilayer stack.

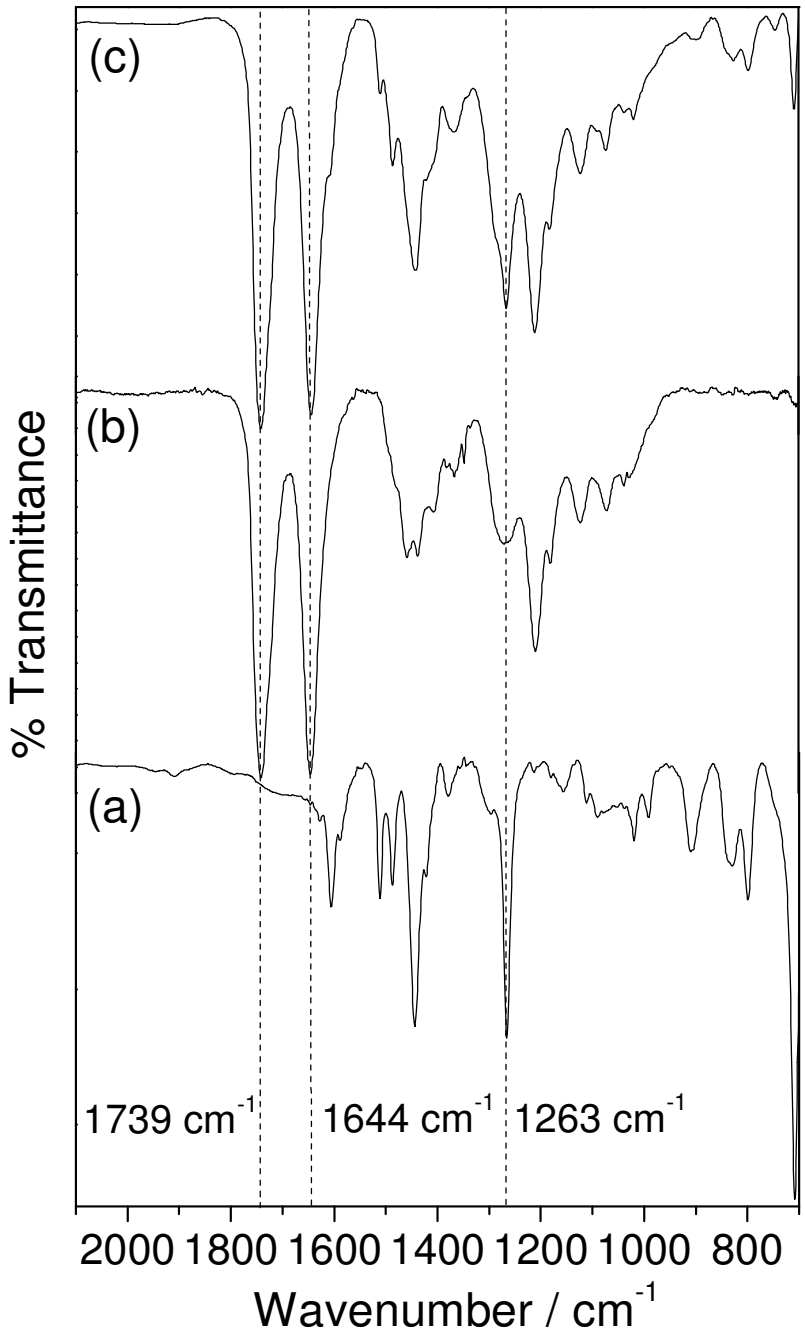

Figure 3.3: Infrared spectra of: (a) 100 nm pulsed plasma deposited poly(vinylbenzyl chloride) ATRP initiator layer; (b) 20 nm pulsed plasma deposited poly(*N*-acryloylsarcosine methyl ester) barrier layer; and (c) bilayer stack comprising 100 nm pulsed plasma deposited poly(vinylbenzyl chloride) initiator base film with 20 nm pulsed plasma deposited poly(*N*-acryloylsarcosine methyl ester) overlayer.

Piercing of the aforementioned bilayer stacks using a scanning probe tip (<12.5 nm radius of curvature, front angle 15 ± 2°, back angle 17.5 ± 2°), followed by tapping mode AFM imaging, revealed 80 nm to 100 nm indentation features, Figure 3.4. ATRP was then observed to occur exclusively from the exposed underlying poly(vinylbenzyl chloride) initiator layer regions, thus confirming that the molecular scratchcard technique successfully unveils ATRP initiator functionalities. Poly(methyl methacrylate) brush features following 30 min grafting from the punctured areas were measured to have dry heights of 47 ± 16 nm and lateral dimensions spreading out sideways to several hundred nms, Figure 3.4. Trench lines were also scratched into the bilayer samples using this approach, followed by ATRP of methyl methacrylate for 60 min and 120 min, to yield polymer brush heights / widths of 105 ± 16 nm / 834 ± 178 nm and 222 ± 45 nm / 1915 ± 224 nm respectively, again revealing spillover of the polymer brushes across the surrounding poly(*N*-acryloylsarcosine methyl ester) barrier layer surface, Figure 3.5.

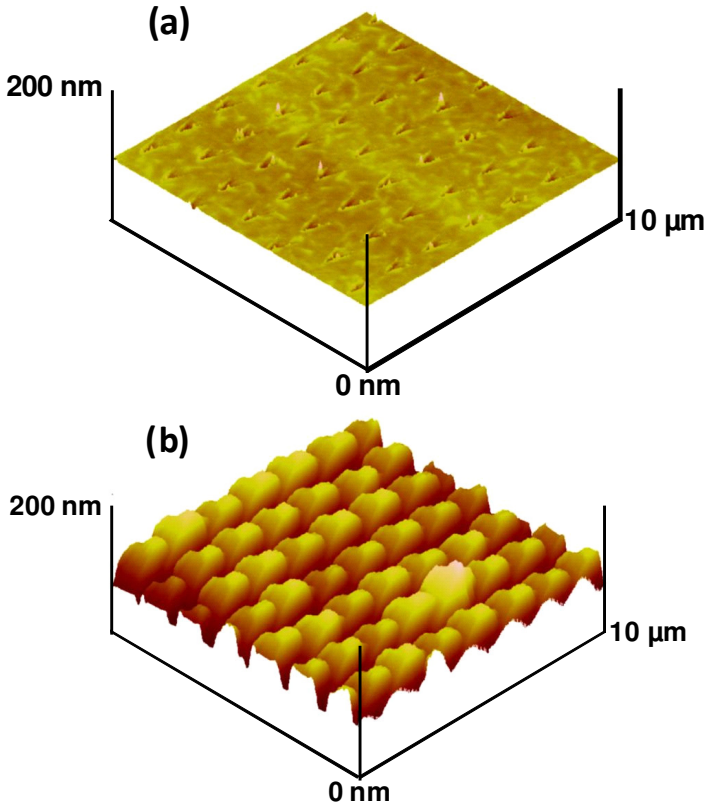

Figure 3.4: Tapping mode AFM height images of poly(vinylbenzyl chloride) / poly(*N*-acryloylsarcosine methyl ester) bilayers: (a) 80-100 nm indentations spaced 1.3 µm apart prepared using a scanning probe tip; and (b) following ATRP of methyl methacrylate for 30 min from (a).

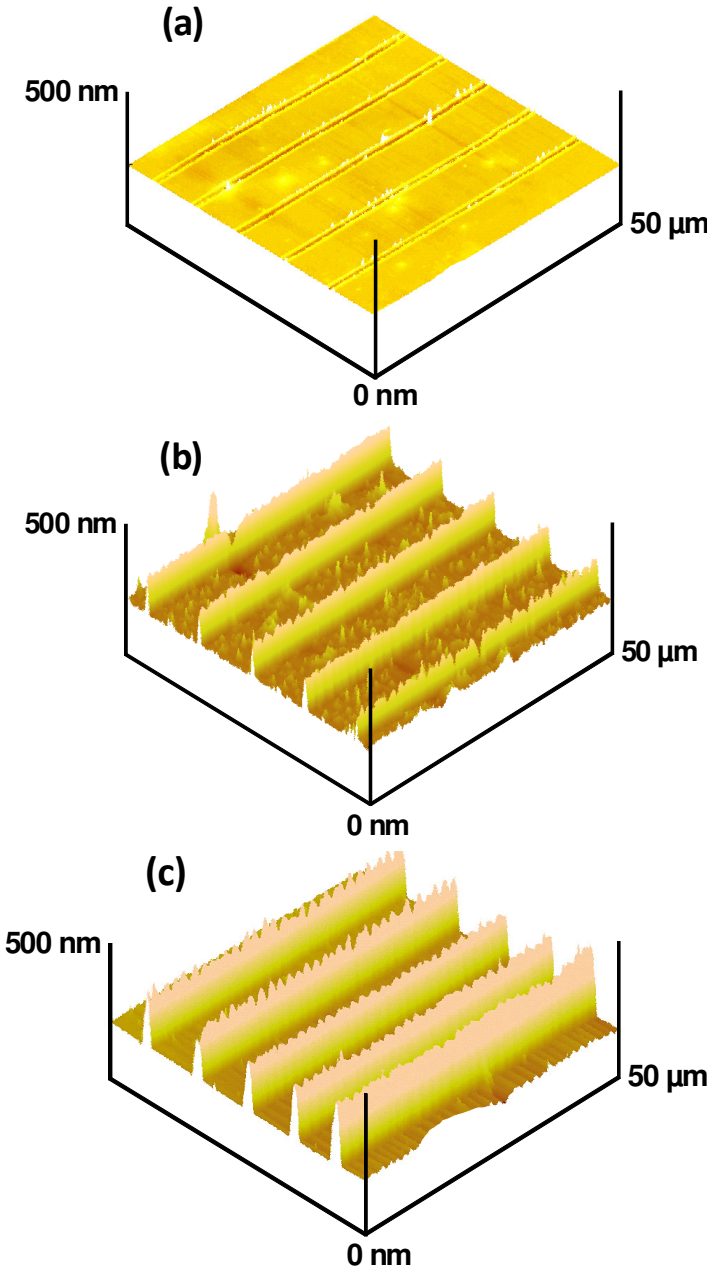

Figure 3.5: Tapping mode AFM height images of pulsed plasma deposited poly(vinylbenzyl chloride) / poly(*N*-acryloylsarcosine methyl ester) bilayers: (a) 100 nm trenches scratched using a scanning probe tip; (b) subsequent ATRP graft polymerization of methyl methacrylate for 60 min; and (c) subsequent ATRP graft polymerization of methyl methacrylate for 120 min.

The widths and heights of the nanopatterned poly(methyl methacrylate) brush lines were found to be responsive to propan-2-ol solvent, Figure 3.6. Lateral spreading of the polymer brushes was observed by AFM, with measured heights / widths progressively changing from the initial values of 200 nm / 2000 nm to 30 nm / 3000 nm after 3 immersions in propan-2-ol. No subsequent changes in dimensions were measured following either overnight drying, drying in a stream of nitrogen, or heating in an oven maintained at 80 ℃ for 4 h. Exposure to solvents such as water, methanol or cyclohexane and then drying also had no influence on these horizontally spread out polymer brush dimensions. However, dipping this substrate into toluene or tetrahydrofuran followed by drying resulted in the original polymer brush line dimensions being restored, Figure 3.6. Manipulation of the surface architecture in this manner with the respective solvents was found to be reversible (over three repetitive cycles of spreading and restoration by cycling between propan-2-ol and toluene, respectively).

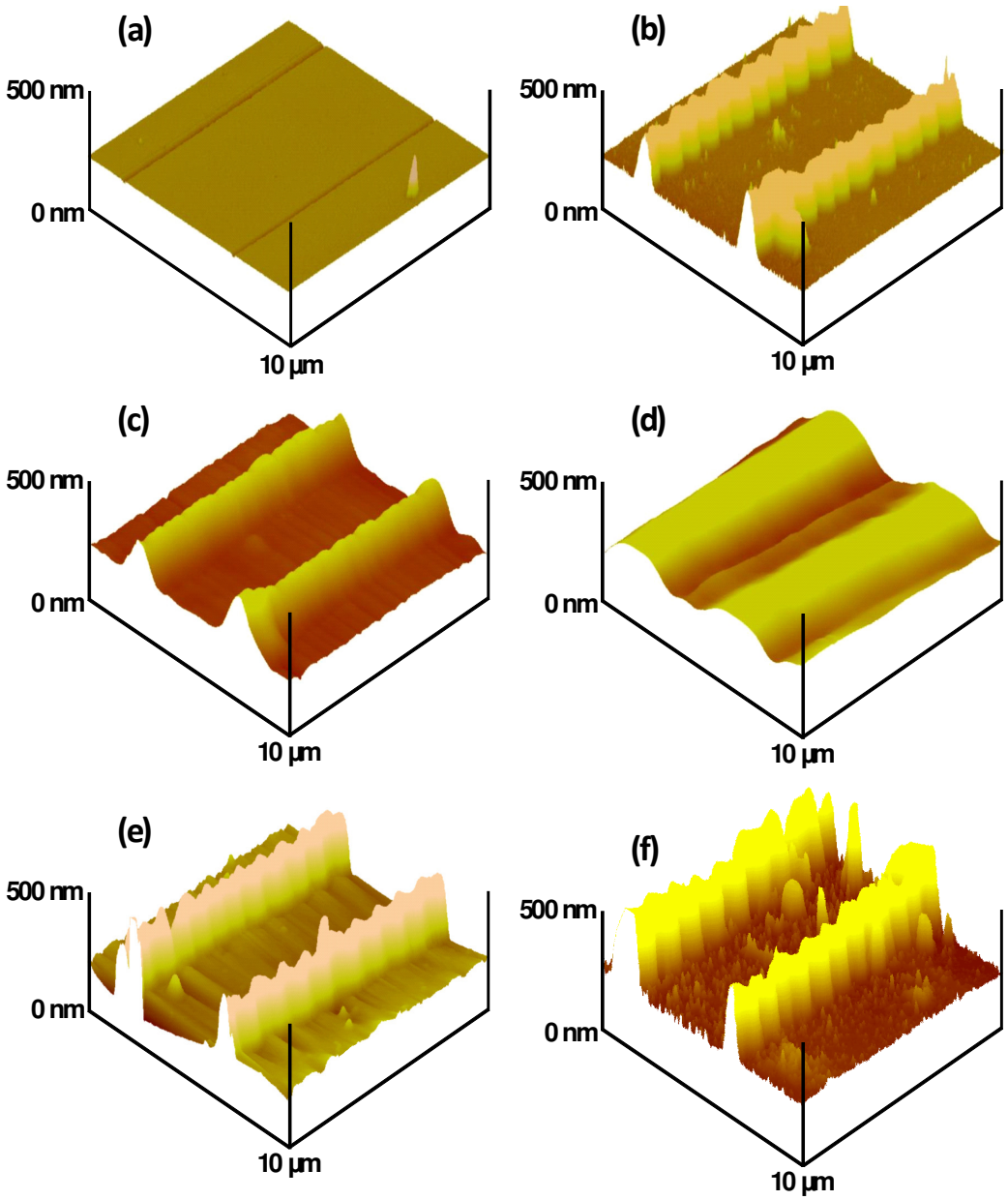

Figure 3.6: Tapping mode AFM height images of pulsed plasma deposited poly(vinylbenzyl chloride) / poly(*N*-acryloylsarcosine methyl ester) bilayers: (a) 100 nm wide lines created by scanning probe tip scratching; (b) after 120 min ATRP grafting of poly(methyl methacrylate); (c) after immersion of (b) in propan-2-ol and drying; (d) after immersion and drying of (b) in propan-2-ol for 3 cycles; (e) after the exposure of (d) to toluene; and (f) after the exposure of (d) to tetrahydrofuran.

Infrared spectra of ATRP grafted poly(methyl methacrylate) brush films following immersion into propan-2-ol revealed a distinctive absorbance band at 3400 cm^{-1} attributable to the O-H stretch,[36] Figure 3.7. This feature was absent for polymer brush samples exposed to toluene, or after contact with propan-2-ol and then rinsing in toluene. A corresponding shift in the polymer brush carbonyl ester stretch was observed between 1740 cm^{-1} (toluene) and 1736 cm^{-1} (propan-2-ol) which, together with the appearance of a shoulder at 1699 cm^{-1} (propan-2-ol), signified a reversible change in chemical environment. Comparable spectra were noted for commercially available low molecular weight poly(methyl methacrylate) spin coated from toluene and propan-2-ol solutions. For all propan-2-ol exposed polymer brush samples, extensive drying and treatment with non-solvents (water, methanol and cyclohexane) produced no effect on the observed infrared spectra, thereby confirming propan-2-ol was being incorporated into the poly(methyl methacrylate) polymer brush matrix, and could be dislodged only with selective solvents (e.g., toluene or tetrahydrofuran). Contact angle measurements were consistent with the aforementioned observations, Table 3.3. A lowering of the water contact angle was noted following immersion of the poly(methyl methacrylate) polymer brushes in propan-2-ol. This change in the water contact angle value was reversed by rinsing in toluene.

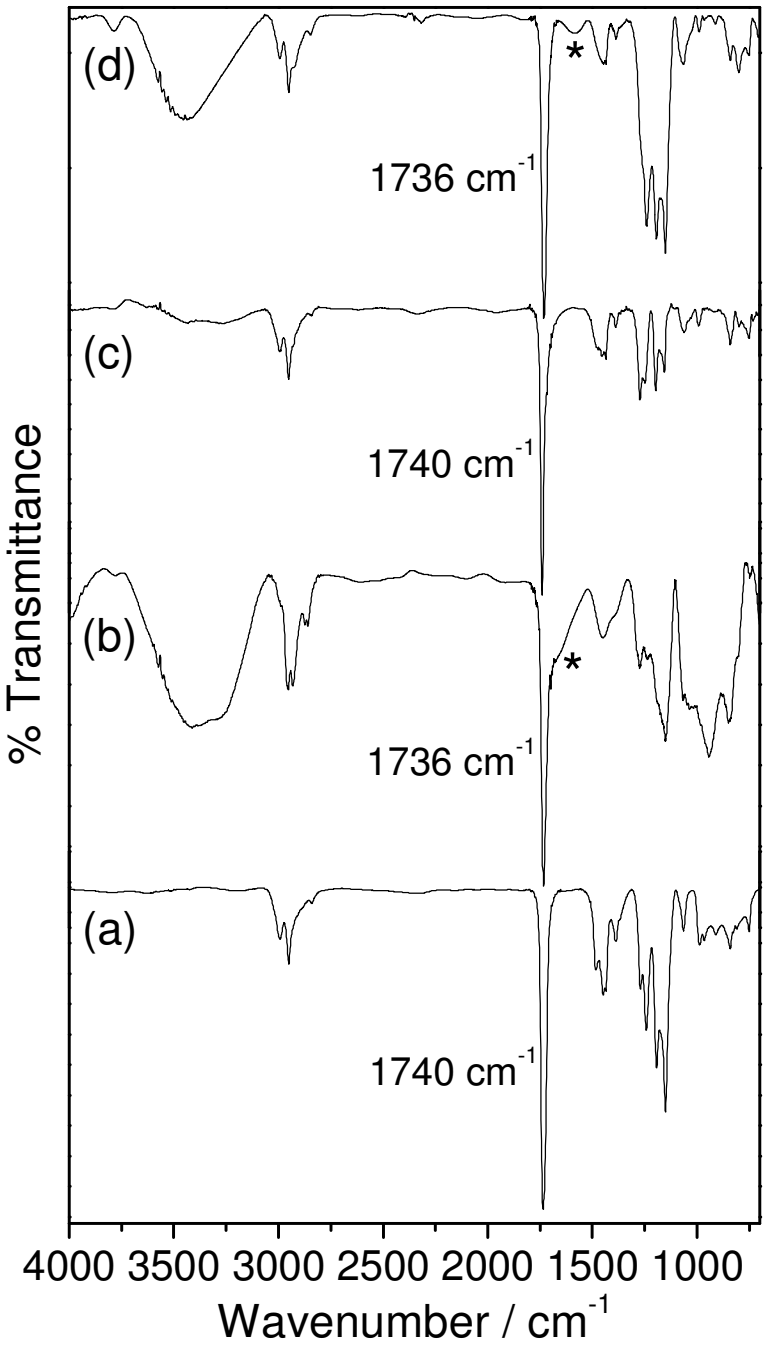

Figure 3.7: Infrared spectra of: (a) commercially available low molecular weight poly(methyl methacrylate) spin coated from toluene solution; (b) commercially available low molecular weight poly(methyl methacrylate) spin coated from propan-2-ol solution; (c) poly(methyl methacrylate) brushes grafted by ATRP from pulsed plasma deposited poly(vinylbenzyl chloride) initiator layers followed by immersion in toluene; and (d) poly(methyl methacrylate) brushes grafted by ATRP from pulsed plasma deposited poly(vinylbenzyl chloride) initiator layers followed by immersion in propan-2-ol. Where * denotes a shoulder at 1699 cm^{-1}.

Table 3.3: Sessile drop water contact angle measurements for pulsed plasma deposited poly(*N*-acryloylsarcosine methyl ester) barrier layer, and ATRP grafted polymer brushes following immersion into various solvents and drying (error values are one standard deviation).

Surface	***Contact angle (°)***
Pulsed plasma poly(*N*-acryloylsarcosine methyl ester)	49 ± 1
ATRP grafted poly(methyl methacrylate)	87 ± 4
ATRP grafted poly(methyl methacrylate) after immersion in propan-2-ol	70 ± 2
ATRP grafted poly(methyl methacrylate) after immersion in propan-2-ol and toluene	92 ± 2
ATRP grafted poly(glycidyl methacrylate)	72 ± 3
ATRP grafted poly(glycidyl methacrylate) derivatised with Alexafluor Cadaverine 350 dye	65 ± 3
ATRP grafted poly(glycidyl methacrylate) derivatised with Alexafluor Cadaverine 350 dye after immersion in water	41 ± 3
ATRP grafted poly(glycidyl methacrylate) derivatised with Alexafluor Cadaverine 350 dye after immersion in water and toluene	66 ± 3

In order to understand this solvent triggered surface spreading of polymer brushes further, poly(glycidyl methacrylate) brush lines were ATRP grafted from trench lines prepared on the bilayer molecular scratchcard (following the same procedure as described earlier for poly(methyl methacrylate)), Table 3.4. These were also found to display a similar spreading effect and affinity towards propan-2-ol.

Table 3.4: ATRP grafted polymer brush features grown from 100 nm trench lines produced on a molecular scratchcard bilayer (error values are one standard deviation).

Surface	***Width*** *(nm)*	***Height*** *(nm)*
60 min ATRP grafted poly(methyl methacrylate)	834 ± 178	105 ± 16
30 min ATRP grafted poly(glycidyl methacrylate)	981 ± 123	56 ± 6

Fluorescent tagging of the poly(glycidyl methacrylate) brushes via nucleophilic ring opening of the epoxide centres was undertaken using a dilute solution of Alexafluor 350 Cadaverine dye, Scheme 3.3. Fluorescence microscopy then revealed selective uptake of the fluorophore by the patterned poly(glycidyl methacrylate) regions, Figure 3.8. Once tagged however, the poly(glycidyl methacrylate) brushes were no longer found to spread upon exposure to propan-2-ol. Instead, because of the inherent polarity of the attached dye molecules, water was found to be effective for this system, as confirmed by fluorescence microscopy and AFM imaging, Figure 3.8. Fluorescence was observed across the entire imaged region following immersion in water, indicating that the closely spaced poly(glycidyl methacrylate) line features had extended to overlap and completely cover the surrounding barrier surface. Furthermore, this behaviour was reversible via rinsing in toluene (analogous to the earlier described system of surface grafted poly(methyl methacrylate) brushes interacting with propan-2-ol and toluene), Figure 3.8. Contact angle measurements made on a film of dye-derivatised poly(glycidyl methacrylate) brushes showed a lowering of the water contact angle value following immersion in water, and its subsequent reversal after rinsing with toluene, Table 3.3. These observations are consistent with the polymer brush movements (surface wetting) noted using fluorescence microscopy for the patterned dye-tagged poly(glycidyl methacrylate) brush surfaces.

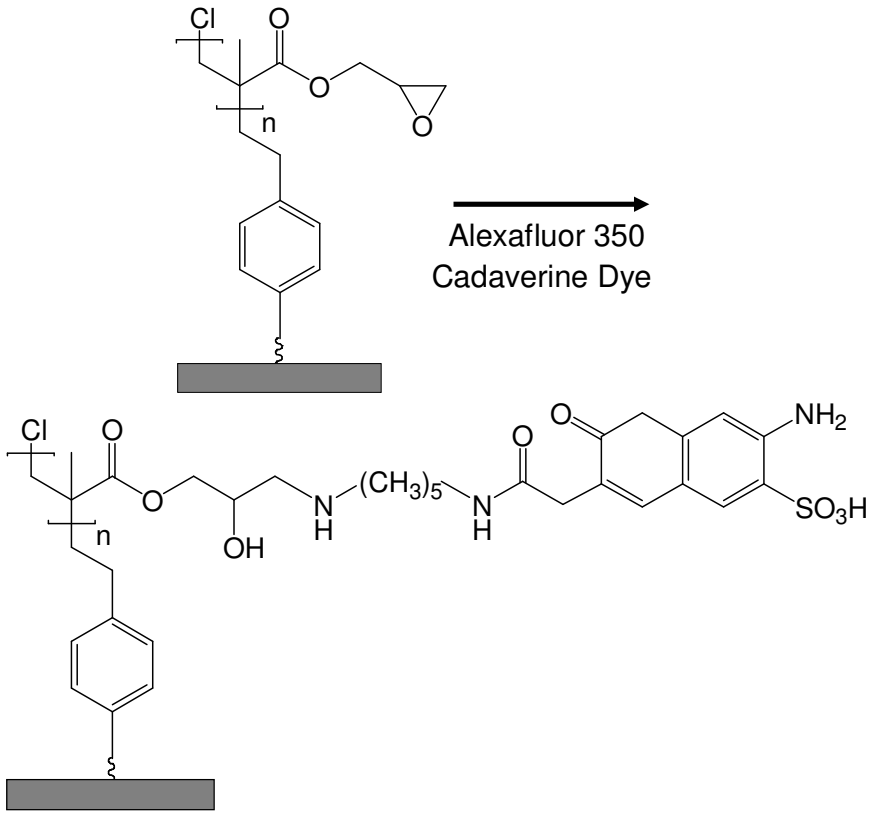

Scheme 3.3: ATRP grafting of glycidyl methacrylate onto pulsed plasma deposited poly(vinylbenzyl chloride) initiator layer followed by nucleophilic ring opening of the epoxide groups with Alexafluor 350 Cadaverine dye.

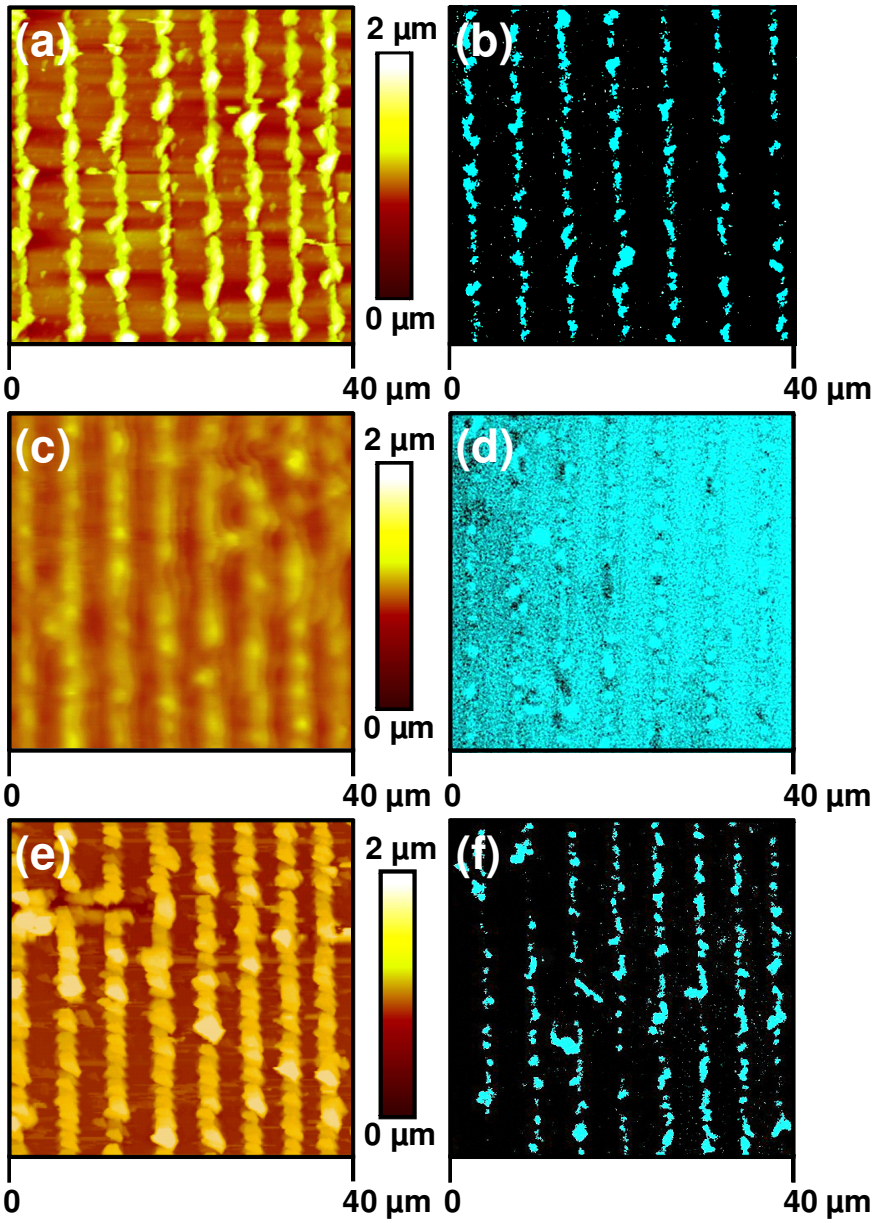

Figure 3.8: 30 min ATRP grafted poly(glycidyl methacrylate) lines on patterned pulsed plasma deposited poly(vinylbenzyl chloride) / poly(*N*-acryloylsarcosine methyl ester) bilayer samples and then tagged with fluorescent dye: (a) tapping mode AFM image; (b) fluorescence micrograph; (c) tapping mode AFM image following the exposure of (a) to water; (d) fluorescence micrograph corresponding to (c); (e) tapping mode AFM image of (c) after washing with toluene; and (f) fluorescence micrograph corresponding to (e). All of the fluorescence images are shown with the same contrast and brightness settings.

3.4 DISCUSSION

Given the wide range of polymers available and the high degree of precision achievable over polymer brush length, patterned surface initiated ATRP is a promising route to multifunctional surfaces.[41,42] Efficient ATRP initiation requires the rate of initiator radical formation to exceed the rate of polymerization propagation.[41] Hence, ATRP initiator surfaces ordinarily contain halogen atoms attached to carboradical stabilising groups, (e.g., tertiary halides in association with conjugating carbonyl groups).[43,44,45,46] In the case of poly(vinylbenzyl chloride), benzyl radical stabilisation arises from conjugation with the aromatic ring.[47] Therefore, a high level of precursor structural retention during plasmachemical deposition of the initiator layer is critical for successful ATRP initiation. Indeed, this has been observed for pulsed plasma deposited poly(vinylbenzyl chloride) layers, where good agreement between measured XPS elemental compositions and predicted theoretical values is found, as are definitive infrared fingerprint features, Table 3.2 and Figure 3.1. ATRP of poly(methyl methacrylate) brushes proceeds in a highly controlled fashion from these plasmachemical deposited initiator nanolayers as is evident from the linear increase in film thickness with the time of polymerization, Figure 3.2.

Nanolithographic patterning of bilayer stack samples comprising 100 nm poly(vinylbenzyl chloride) covered with a 20 nm barrier layer of poly(*N*-acryloylsarcosine methyl ester) has been achieved by employing the molecular scratchcard technique.[32] In principle, even smaller feature sizes can be envisaged by adopting sharper probes for piercing (e.g., carbon nanotube SPM tips).[48] For such ultrathin and soft polymer layers, the SPM probe retains its sharpness to allow satisfactory patterning of several samples with no perceptible loss in feature size (despite the direct contact methodology). This is an important advantage compared to earlier attempts within this field where tip wear has prevented the more widespread application of SPM lithographic techniques.[49,50,51]

For similar grafting times, there is a disparity between polymer brush layer heights for grafting directly from pulsed plasma deposited poly(vinylbenzyl chloride) and nanopatterned bilayer samples, with heights of the nanopatterned poly(methyl methacrylate) features 4 to 5 times greater

than the measured thickness of corresponding (effectively) infinite brush layers, Figures 3.2, 3.4 and 3.5. This is contrary to previous reports for patterned brushes found in the literature, where lateral relaxation of brushes reduces the thickness of patterned features in comparison to infinite layers.[20] One explanation for the thickness of brush features in the present study could be confinement of the grafted polymer chains causing them to extend vertically. This could be brought about by an effective increase in initiator density in patterned regions due to the concave shape of indentations or trenches made using the SPM probe. However, it has been shown that ATRP initiated at concave surfaces is actually expected to proceed more slowly than that initiated from planar substrates.[52,53] An alternative reason may be a change in the polymerization kinetics owing to enhanced availability of initiator sites in the case of nanopatterns. Further investigations are needed to properly account for the formation of such large features and could include varying the width of surface patterns by using SPM probes of differing sharpness for patterning, and monitoring the shape of grafted brush features.

A striking observation made in this study has been lateral polymer brush spreading under certain conditions, e.g., solvents. For ATRP grafted poly(methyl methacrylate) brushes, diffusion of propan-2-ol molecules into this amorphous polymer causes expansion to produce a swollen rubbery material.[54,55] Such chain solvation depends upon the thermodynamic compatibility of the polymer with the solvent, and can be approximated through comparison of the respective solubility parameters,[56] Table 3.5. A large difference implies that the polymer and solvent are thermodynamically incompatible, and polymer dissolution does not progress beyond swelling. On the other hand, if the difference is relatively small, then polymer chains become disentangled and dissolve because of favourable solvent-polymer intermolecular interactions. The extent and rate of this disentanglement is influenced by numerous factors including the degree of cross-linking, polymer molecular weight and solvent diffusion rate.[54,57,58] Surface tethered polymer brushes grafted by ATRP can be regarded as negligibly cross-linked and of low molecular weight; however, secure covalent anchoring of these polymer chains to the substrate prevents their complete dissolution.[59]

Table 3.5: Hansen solubility parameters for poly(methyl methacrylate) and various solvents. The total solubility parameters (δ_o) consist of contributions from dispersion forces (δ_d), dipolar forces (δ_p) and hydrogen bonding (δ_h).[56]

Polymer / Solvent	δ_o	***Components of δ_o***		
		δ_d	δ_p	δ_h
Water	47.9	15.5	16.0	42.4
Methanol	29.7	15.1	12.3	22.3
Propan-2-ol	23.5	15.8	6.1	16.4
Poly(methyl methacrylate)	22.7	18.6	10.5	7.5
Tetrahydrofuran	19.4	16.8	5.7	8.0
Toluene	18.0	18.0	1.4	2.0
Cyclohexane	16.8	16.8	0	0.2

The aforementioned thermodynamic compatibility for solvent-polymer pairs is primarily governed by the specific intermolecular interactions, Table 3.5. The total solubility parameters (δ_o) are a measure of internal cohesion and contain contributions from dispersion forces (δ_d), dipolar forces (δ_p) and hydrogen bonding (δ_h) (Hansen three dimensional solubility parameters).[56] The more similar these contributing parameters are for two substances, the more miscible they will be. Reported literature solubility parameters predict that tetrahydrofuran should be a strong solvent for poly(methyl methacrylate) because of its similar total solubility parameter (δ_o); therefore, the corresponding polymer brushes can be expected to extend into the solvent during immersion.[56] Toluene also has a similar overall solubility parameter (δ_o), although it can be seen that polar and hydrogen bonding contributions are much lower. In the case of toluene, however, additional specific π-π interactions are expected to exist between aromatic toluene and the π system of the poly(methyl methacrylate) ester groups which are not accounted for by the polar component of the solubility parameter. In contrast, non-polar cyclohexane is predicted to be a much poorer solvent for poly(methyl methacrylate), because of its very low values for both the dipolar solubility

parameter (δ_p) and the hydrogen bonding parameter (δ_h) compared to poly(methyl methacrylate), leading to a negligible interaction with the polymer brush chains. For the case of lower alcohols and water, overall solubility parameters (δ_o) predict them to be poor solvents for poly(methyl methacrylate) because of the much greater level of hydrogen bonding (δ_h) present within these solvents, yielding poor polymer-solvent miscibility. Hence, exposure to water or methanol affords no change to poly(methyl methacrylate) brush feature shape within the time scales utilised in this study, whereas a swelling effect was observed following immersion in the slightly more compatible solvent, propan-2-ol, and drying (for propan-2-ol the overall solubility parameter is similar to that of poly(methyl methacrylate), but the much higher contribution of hydrogen bonding within propan-2-ol indicates that it would be a poor solvent and less likely to diffuse into poly(methyl methacrylate), as this involves interaction with poly(methyl methacrylate) rather than with itself). Slow diffusion of poor solvents into and out of a polymer matrix is known to result in solvent entrapment. In fact, it is well known that lower alcohols are poor solvents for poly(methyl methacrylate), and immersion may lead to swelling rather than dissolution.[57,60]

Hydrogen bonding of propan-2-ol molecules with the poly(methyl methacrylate) brushes was confirmed by infrared analysis,[61,62] Figure 3.7. The reversible shift of the infrared ester carbonyl absorption towards lower frequencies following exposure to propan-2-ol, accompanied by the appearance of a shoulder on the peak at 1699 cm^{-1}, can be attributed to these hydrogen bonding effects (which weaken the C=O bond and thereby shift the vibrations to a lower frequency).[36] Entrapment of propan-2-ol within the polymer brushes (lowering the water contact angle to 70°) encourages their lateral spreading across the adjacent hydrophilic surface, with a concurrent drop in feature height. Removal of the trapped propan-2-ol by toluene or tetrahydrofuran can be rationalised on the basis of poly(methyl methacrylate) polymer brushes extending into these solvents, with concurrent displacement of propan-2-ol into solution,[63] thereby restoring the polymer brush features back to their original form.

A similar argument may be made for the spillover of patterned poly(glycidyl methacrylate) brushes with propan-2-ol, and their subsequent

restoration using toluene. However, reaction of the pendant epoxy groups with the highly polar fluorophore, Alexafluor 350 Cadaverine, yields derivatised poly(glycidyl methacrylate) brushes which lose their affinity towards propan-2-ol, (greater difference in polarity and hydrophilicity) Scheme 3.3 and Table 3.5. Instead, water now induces the swelling effect, which is consistent with its greater compatibility with the hydrophilic character of the dye derivatised polymer brushes. Fluorescence microscopy shows that these swollen (extended) polymer brushes can be made to wet the adjacent poly(*N*-acryloylsarcosine methyl ester) background and thus overlap, Figure 3.8.

Previously reported solvent responsive polymer brush layers have shown only conformational transitions of block co-polymers or phase separation of mixed polymers (where one of the film constituents displays greater affinity towards a solvent).[64,65,66,67] In addition it is only the *vertical* swelling and collapse of surface tethered polymer brushes that is documented for good/poor solvents.[68,69] The long lasting entrapment of poor solvents into patterned ATRP brushes to provide a mechanism for lateral surface spreading has not been previously accomplished. It is envisaged that this new surface phenomenon provides an additional tool for fabricating smart multifunctional surfaces.

3.5 CONCLUSIONS

The surface patterning of poly(vinylbenzyl chloride) ATRP initiator sites followed by polymerization using molecular scratchcard lithography can be used to produce nanoscale three-dimensional polymer brush architectures whose aspect ratios are responsive towards external stimulation. For instance, the spreading and retraction of polymer brushes across a protein resistant surface can readily be actuated by choice of solvent, thereby providing the means for hiding and unveiling functional surfaces.

3.6 REFERENCES

(1) Fan, X.; Lin, L.; Dalsin, J. L.; Messersmith, P. B. *J. Am. Chem. Soc.* **2005**, *127*, 15843.

(2) Co, C. C.; Wang, Y.-C.; Ho C.-C. *J. Am. Chem. Soc.* **2005**, *127*, 1598.

(3) Li, L.; Driscoll, M.; Kumi, G.; Hernandez, R.; Gaskell, K. J.; Losert, W.; Fourkas, J. T. *J. Am. Chem. Soc.* **2008**, *130*, 13512.

(4) Doh, J.; Irvine, D. J. *J. Am. Chem. Soc*. **2004**, *126*, 9170.

(5) Christman, K. L.; Schopf, E.; Broyer, R. M.; Li, R. C.; Chen, Y.; Maynard, H. D. *J. Am. Chem. Soc.* **2009**, *131*, 521.

(6) Zhou, H.; Baldini, L.; Hong, J.; Wilson, A. J.; Hamilton, A. D. *J. Am. Chem. Soc.* **2006**, *128*, 2421.

(7) Vullev, V. I.; Wan, J.; Heinrich, V.; Landsman, P.; Bower, P. E.; Xia, B.; Millare, B.; Jones, G. *J. Am. Chem. Soc.* **2006**, *128*, 16062.

(8) Rolland, J. P.; Van Dam, R. M.; Schorzman, D. A.; Quake, S. R.; DeSimone, J. M. *J. Am. Chem. Soc.* **2004**, *126*, 2322.

(9) Childs, W. R.; Nuzzo, R. G. *J. Am. Chem. Soc.* **2002**, *124*, 13583.

(10) Schofield, W. C. E.; McGettrick, J.; Bradley, T. J.; Badyal, J. P. S.; Przyborski, S. *J. Am. Chem. Soc.* **2006**, *128*, 2280.

(11) Hyun, J.; Chilkoti, A. *J. Am. Chem. Soc.* **2001**, *123,* 6943.

(12) Davis, J.; Glidle, A.; Cass, A. E. G.; Zhang, J.; Cooper, J. M. *J. Am. Chem. Soc.* **1999**, *121,* 4302.

(13) Vázquez-Dorbatt, V.; Tolstyka, Z. P.; Chang, C.-W.; Maynard, H. D. *Biomacromolecules* **2009**, *10*, 2207.

(14) Zhou, F.; Zheng, Z.; Yu, B.; Liu, W.; Huck, W. T. S. *J. Am. Chem. Soc.* **2006**, *128*, 16253.

(15) Ma, H.; Li, D.; Sheng, X.; Zhao, B.; Chilkoti. A. *Langmuir* **2006**, *22*, 3751.

(16) Edmondson, S.; Vo, C.-D.; Armes, S. P.; Unali, G.-F. *Macromolecules* **2007**, *40*, 5271.

(17) Hamelinck, P. J.; Huck, W. T. S. *J. Mater. Chem*. **2005**, *15*, 381.

(18) Iwata, R.; Suk-In, P.; Hoven, V. P.; Takahara, A.; Akiyoshi, K.; Iwasaki, Y. *Biomacromolecules* **2004**, *5*, 2308.

(19) Maeng, I. S.; Park, J. W. *Langmuir* **2003**, *19*, 9973.

(20) Jonas, A. M.; Hu, Z.; Glinel, K.; Huck, W. T. S. *Macromolecules* **2008**, *41*, 6859.

(21) Chen, J.-K.; Hsieh, C.-Y.; Huang, C.-F.; Li, P.-M.; Kuo, S.-W.; Chang, F.-C. *Macromolecules* **2008**, *41*, 8729.

(22) Zou, Y.; Yeh, P.-Y. J.; Rossi, N. A. A.; Brooks, D. E.; Kizhakkedathu, J. N. *Biomacromolecules* **2010**, *11*, 284.

(23) Dong, R.; Krishnan, S.; Baird, B. A.; Lindau, M.; Ober, C. K. *Biomacromolecules* **2007**, *8*, 3082.

(24) von Werne, T. A.; Germack, D. S.; Hagberg, E. C.; Sheares, V. V.; Hawker, C. J.; Carter, K. R. *J. Am. Chem. Soc.* **2003**, *125*, 3831.

(25) Hauquier, F.; Matrab, T.; Kanoufi, F.; Combellas, C. *Electrochim. Acta* **2009**, *54*, 5127.

(26) Slim, C.; Tran, Y.; Chehimi, M. M.; Garraud, N.; Roger, J.-P.; Combellas, C.; Kanoufi, F. *Chem. Mater.* **2008**, *20*, 6677.

(27) Kaholek, M.; Lee, W.-K.; LaMattina, B.; Caster, K. C.; Zauscher, S. *Nano Lett.* **2004**, *4*, 373.

(28) Ma, H.; Hyun, J.; Stiller, P.; Chilkoti, A. *Adv. Mater.* **2004**, *16*, 338.

(29) Harris, L. G.; Schofield, W. C. E.; Doores, K. J.; Davis, B. G.; Badyal, J. P. S. *J. Am. Chem. Soc.* **2009**, *131,* 7755.

(30) McGettrick, J.; Harris, L. G.; Badyal, J. P. S. GB Pat. Appl. No. 0509213.5, 2005.

(31) Muir, B. W.; Fairbrother, A.; Gengenbach, T. R.; Rovere, F.; Abdo, M. A.; McLean, K. M.; Hartley, P. G. *Adv. Mater.* **2006**, *18*, 3079.

(32) Harris, L. G.; Schofield, W. C. E.; Badyal, J. P. S. *Chem. Mater.* **2007**, *19,* 1546.

(33) Teare, D. O. H.; Barwick, D. C.; Schofield, W. C. E.; Garrod, R. P.; Ward, L. J.; Badyal, J. P. S. *Langmuir* **2005**, *21*, 11425.

(34) Teare, D. O. H.; Schofield, W. C. E.; Garrod, R. P.; Badyal, J. P. S. *J. Phys. Chem. B* **2005**, *109*, 20923.

(35) Liu, Y.; Klep, V.; Luzinov, I. *J. Am. Chem. Soc.* **2006**, *128*, 8106.

(36) Lin-Vien, D.; Colthrup, N. B.; Fateley, W. G.; Grasselli, J. G. *The Handbook of Infrared and Raman Characteristic Frequencies of Organic Molecules*; Academic Press: Boston, 1991.

(37) Ejaz, M.; Yamamoto, S.; Tsujii, Y.; Fukuda, T. *Macromolecules* **2002**, *35,* 1412.

(38) Tomlinson, M. R.; Genzer, J. *Macromolecules* **2003**, *36*, 3449.

(39) Saha, S.; Bruening, M. L.; Baker, G. L. *ACS Appl. Mater. Interfaces* **2011**, *3*, 3042.

(40) Odian, G. G. *Principles of Polymerization*, John Wiley & Sons: New York, 2004; p 226.

(41) Jennings, G. K.; Brantley, E. L. *Adv. Mater.* **2004**, *16*, 1983.

(42) Pyun, J.; Kowalewski, T.; Matyjaszewski, K. *Macromol. Rapid Commun.* **2003**, *24*, 1043.

(43) Robinson, K. L.; Weaver, J. V. M.; Armes, S. P.; Marti, E. D.; Meldrum, F. C. *J. Mater. Chem.* **2002**, *12*, 890.

(44) Wang, J.-Y.; Chen, W.; Liu, A.-H.; Lu, G.; Zhang, G.; Zhang, J.-H.; Yang, B. *J. Am. Chem. Soc.* **2002**, *124*, 13358.

(45) Moreno, J.; Sherrington, D. C. *Chem. Mater.* **2008**, *20,* 4468.

(46) Miller, M. D.; Baker, G. L.; Bruening, M. L. *J. Chromatogr. A* **2004**, *1044*, 323.

(46) Clayden, J.; Greeves, N.; Warren, S.; Worthers, P. *Organic Chemistry;* Oxford University Press: Oxford, U.K., 2001; p1026.

(48) Wilson, N. R.; Macpherson, J. V. *Nature Nanotechnology*, **2009**, 4, 483.

(49) Cui, Z. *Nanofabrication: Principles, Capabilities and Limits*, Springer, 2008, p 151.

(50) Chung, K.-H.; Lee, Y.-H.; Kim, D.-E.; Yoo J.; Hong, S. *IEEE Trans. Magn.* **2005**, *41*, 849.

(51) Khurshudov, A. G.; Kato, K.; Koide, H. *Tribol. Lett.* **1996**, *2*, 345.

(52) Gorman, C. B.; Petrie, R. J.; Genzer, J. *Macromolecules* **2008**, *41*, 4856.

(53) Liu, H.; Zhu, Y.-L.; Zhang, J.; Lu, Z.-Y.; Sun, Z.-Y. *ACS Macro Lett.* **2012**, *1*, 1249.

(54) Stevens, F. *J. Appl. Polym. Sci*. **2005**, *97*, 1082.

(55) Zhu, M.; Vesely, D. *Eur. Polym. J.* **2007**, *43*, 4503.

(56) Brandrup, J.; Immergut, E. H. *Polymer handbook*, 3rd Edition, John Wiley & Sons, **1999**, ch VII.

(57) Lai, K. L.; Leu, I. C.; Hon, M. H. *J. Micromech. Microeng.* **2009**, *19*, 037001.

(58) Favre, E. *Eur. Polym. J.* **1996**, *32*, 1183.

(59) Zhao, B.; Brittain, W. J. *Prog. Polym. Sci.* **2000**, *25*, 677.

(60) Andrews, E. H.; Levy, G. M.; Willis, J. *J. Mater. Sci.* **1973**, *8*, 1000.

(61) Rhudy, K. L.; Su, S.; Howell, H. R.; Urban, M. W. *Langmuir* **2008**, *24,* 1808.

(62) González-Benito, J.; Koenig, J. L. *Macromolecules* **2002**, *35,* 7361.

(63) Kock, H. J.; Rehage, G. *Colloid. Polym. Sci.* **1984**, *262***,** 182.

(64) Zhu, L.; Zhao, B. *J. Phys. Chem. B* **2008**, *112,* 11529.

(65) Motornov, M.; Minko, S.; Eichhorn, K.-J.; Nitschke, M.; Simon, F.; Stamm, M. *Langmuir* **2003**, *19,* 8077.

(66) Minko, S.; Stamm, M.; Horeshnik, E.; Usov, D.; Sidorenko, A. *PMSE Prepr.* 290, **2000**, 20.

(67) Kong, B.; Lee, J. K.; Choi, I. S. *Langmuir* **2007**, *23,* 6761.

(68) Lego, B.; François, M.; Skene, W. G.; Giasson, S. *Langmuir* **2009**, *25,* 5313.

(69) Cuenot, S.; Gabriel, S.; Jérôme, R.; Jérôme, C.; Fustin, C.-A.; Jonas, A. M.; Duwez, A.-S. *Macromolecules* **2006**, *39,* 8428.

CHAPTER 4

A COMBINED PLASMACHEMICAL AND EMULSION TEMPLATING APPROACH FOR ACTUATED MACROPOROUS SCAFFOLDS

4.1 INTRODUCTION

Materials containing interconnected pores are important to a plethora of applications including gas storage,[1,2] fuel cells,[3] catalysis,[4,5] sensors,[6] filtration,[7] chromatography,[8,9] tissue engineering,[10,11] microfluidic devices,[12,13] and biomineralisation.[14] Polymeric scaffolds are particularly attractive for many of these cases due to their low cost and light weight. A common approach for making porous polymer structures involves templated polymerization around the aqueous phase of high internal phase (>70 % aqueous phase[15]) water in oil emulsions (polyHIPEs). Variants of this methodology include templated polymerization around alternative porogenic substances such as salt crystals,[16] colloids,[17] and non-solvents,[18] where the final macroporous structures are obtained by drying, etching, or leaching for porogen extraction. There are drawbacks in all of these cases, which include large consumption of organic solvents and reagents, as well as waste disposal. Moreover, polyHIPE materials are renowned for their poor mechanical properties,[19,20,21] making them difficult to implement for many applications (such as catalysis, fuel cells, microfluidics and tissue engineering) where, in fact, thin macroporous films supported on a robust substrate would be a more viable alternative. One approach employed in the past to produce supported porous films has been the 'breath figure method' whereby the condensation of water droplets onto a spin cast polymer layer serves to template an interconnected pore structure.[22] Nonetheless, even in this instance, there are inherent disadvantages including the prerequisite for precisely controlled humidity and a need for organic solvents (the evaporation of which drives water condensation). Furthermore, such spin casting often presents poor adhesion to the underlying substrate.

In this study, a plasmachemical deposition combined with solvent templating approach is described that decouples pore functionalisation from pore formation. Furthermore, it minimises the usage of expensive reagents and waste generation, as well as offering applicability to a whole host of substrate materials and geometries.[23] Firstly, structurally well-defined functional layers are produced by introducing the film precursor into a pulsed electrical discharge.[24,25] Mechanistically, this entails the generation of active

sites in the gas phase and also at the growing film surface during the short duty cycle on-period (microseconds) followed by conventional polymerization mechanisms proceeding throughout the prolonged duty cycle off-period (milliseconds) in the absence of any UV-, ion-, or electron-induced damage.[26,27] The inherent reactive nature of the electrical discharge ensures good adhesion to the underlying substrate via free radical sites created at the interface during ignition of the plasma.

Although plasmachemical functionalisation of pre-assembled porous supports is well known,[28] the only attempts to directly induce porosity into plasma-deposited films have entailed selective leaching of low molecular weight material, which have suffered from a lack control over length scales and blistering or dissolution.[29,30] In this study it is demonstrated that plasmachemical deposited functional layers can be templated to yield macroporous films containing an interconnected open cell structure by introducing amphiphilic mediating species (such as cresyl violet perchlorate or sodium dodecyl sulphate) in combination with non-solvent (such as water). Furthermore, the host plasma polymer functional groups provide scope for secondary functionalisation of the generated macroporous structure. For instance, poly(vinylbenzyl chloride) films can be utilised for surface initiated atom transfer radical polymerization (ATRP) of poly(glycidyl methacrylate) to yield epoxide polymer brush functionalised macroporous layers, Scheme 4.1. These can then be employed as scaffolds for actuated control of porosity.

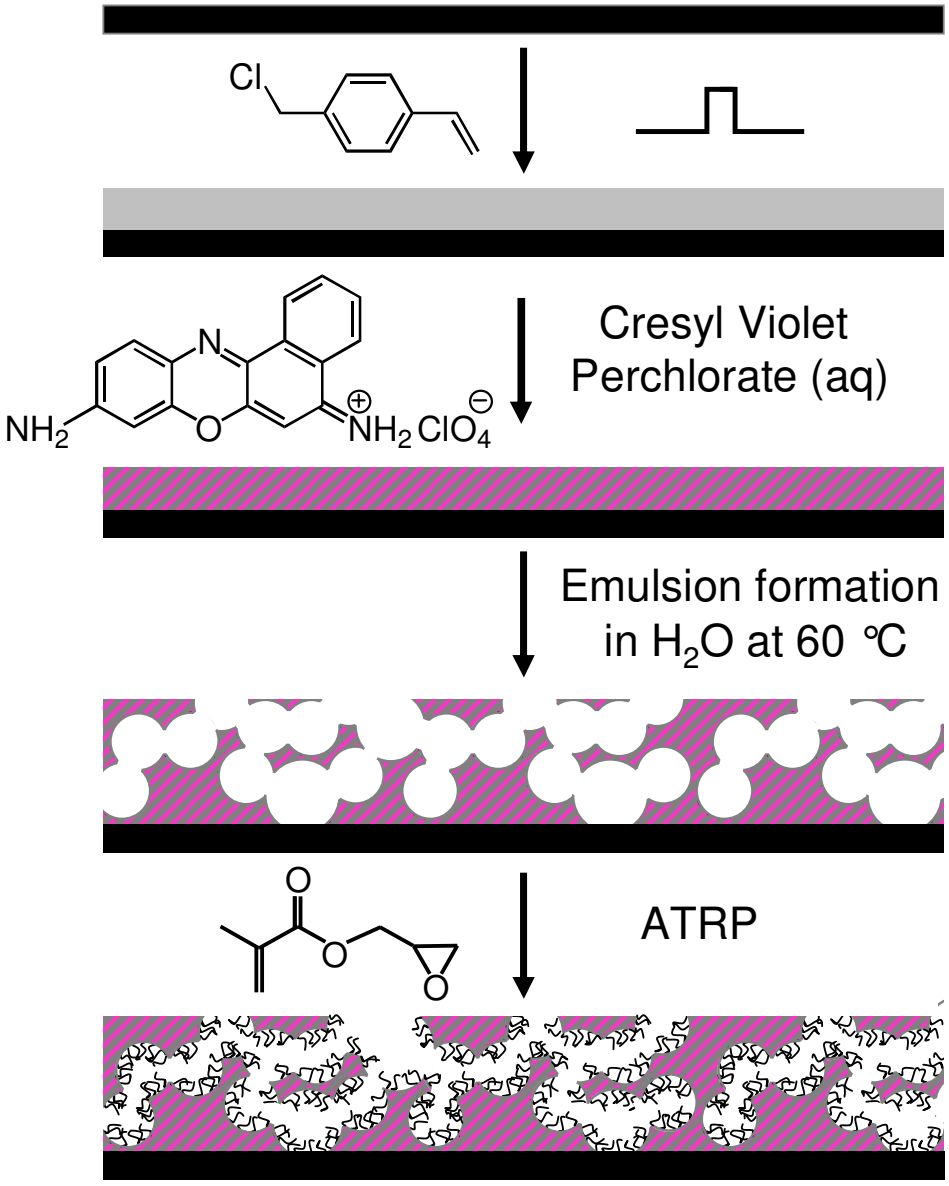

Scheme 4.1: Formation of porous pulsed plasma deposited poly(vinylbenzyl chloride) films by seeding with cresyl violet perchlorate, followed by spontaneous emulsion formation in water at elevated temperature (60 °C), and then additional surface functionalisation of pores (e.g., ATRP).

4.2 EXPERIMENTAL

4.2.1 Pulsed Plasma Deposition of Poly(vinylbenzyl chloride)

Poly(vinylbenzyl chloride) films were deposited by pulsed plasma deposition as described in Chapter 2, section 2.2.1.

4.2.2 Porous Film Formation

Substrates bearing 3 μm thick pulsed plasma deposited poly(vinylbenzyl chloride) layers were immersed in 0.15 mg L^{-1} aqueous solution of cresyl violet perchlorate (analytical grade, Aldrich) for 16 h. Following removal from solution, the samples were thoroughly rinsed with high purity water (BS 3978 Grade 1), and then soaked in fresh high purity water for an additional 16 h at room temperature. In order to induce pore formation, the samples were then placed inside a sealed jar containing high purity water and warmed to 60 °C for 1 h. Finally, the films were dried under ambient conditions for 16 h prior to analysis.

4.2.3 Surface Initiated ATRP of Poly(glycidyl methacrylate)

Porous poly(vinylbenzyl chloride) functionalised substrates were placed inside a sealable glass tube containing copper (I) bromide (5 mmol, +98 %, Aldrich), copper (II) bromide (1 mmol, +99 %, Aldrich), 2,2'-bipyridyl (12 mmol, +99 %, Aldrich), glycidyl methacrylate (0.05 mol, +97 %, Aldrich), and propan-2-ol (4 mL, reagent grade, Fisher), Scheme 4.2. The mixture was thoroughly degassed using freeze-pump-thaw cycles and then allowed to undergo polymerization at room temperature for 4 h. Cleaning and removal of any physisorbed ATRP polymer was accomplished by successive rinsing with propan-2-ol and tetrahydrofuran. Fluorescent tagging of the surface grafted poly(glycidyl methacrylate) epoxide centers was achieved by brief submersion into a 1 mg dm^{-3} aqueous solution of Alexafluor 350 Cadaverine dye (analytical grade, Invitrogen Ltd), followed by extensive rinsing with high purity water, Scheme 4.2.

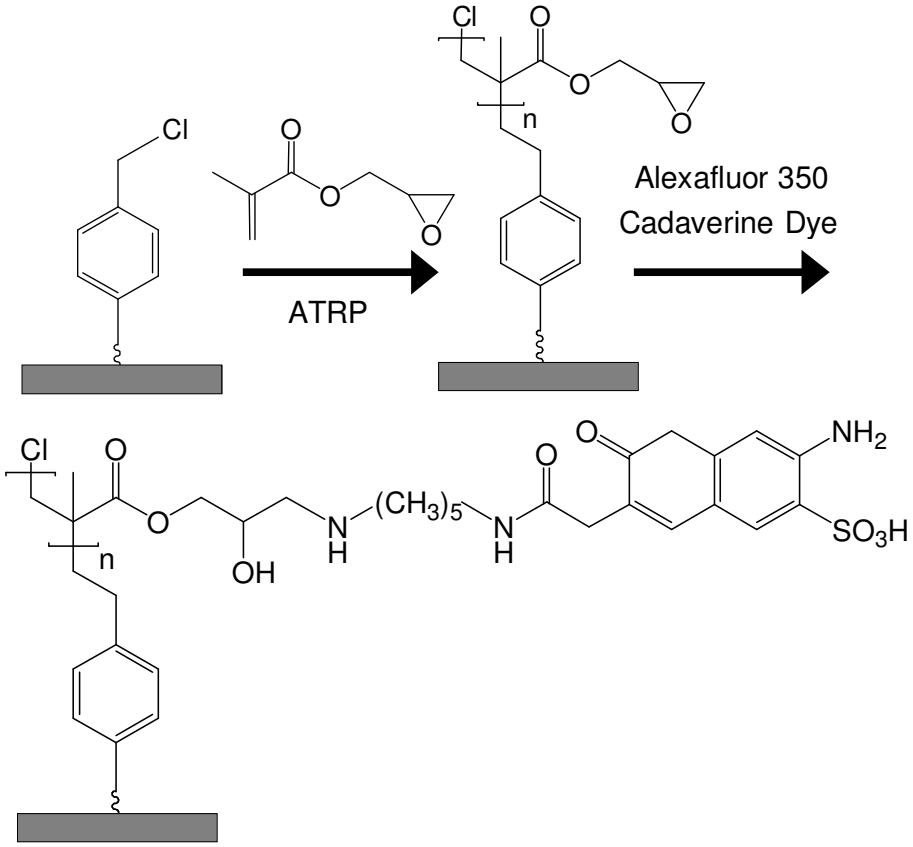

Scheme 4.2: ATRP grafting of glycidyl methacrylate onto pulsed plasma deposited poly(vinylbenzyl chloride) initiator layer followed by nucleophilic ring opening of the epoxide centres using Alexafluor 350 Cadaverine dye.

4.2.4 Film Characterisation

Film thickness, infrared spectra and XPS elemental compositions were measured as described in Chapter 2, Section 2.2.3. Fluorescence microscope images, atomic force microscope (AFM) images and sessile drop contact angles were obtained as described in Chapter 3, Section 3.2.4.

Surface micrographs were obtained with a scanning electron microscope (Cambridge Stereoscan 240). Prepared specimens were placed onto carbon discs and then mounted onto aluminium holders, followed by deposition of 15 nm gold coating (Polaron SEM coating unit). For cross-sectional images, samples were frozen and snapped under liquid nitrogen prior to mounting.

4.3 RESULTS

4.3.1 Pulsed Plasma Deposition of Poly(vinylbenzyl chloride)

XPS analysis of the pulsed plasma deposited poly(vinylbenzyl chloride) ATRP initiator layers yielded elemental compositions and infrared spectroscopy fingerprint features identical to those in Chapter 2, thereby indicating good structural retention of the benzyl chloride functionality, Table 4.1 and Figure 4.1.

Table 4.1: XPS elemental compositions of pulsed plasma deposited poly(vinylbenzyl chloride).

Pulsed Plasma Deposited Poly(vinylbenzyl chloride)		***Elemental Composition***			
		C %	**O %**	**N %**	**Cl %**
As deposited	*Theoretical*	90	0	0	10
	Experimental	90 ± 1	0	0	10 ± 1
Immersion in cresyl violet (aq)	*Experimental*	73 ± 2	20 ± 2	4 ± 1	3 ± 1
Cresyl violet (aq) + 16 h water rinsing	*Experimental*	79 ± 2	14 ± 2	2 ± 1	5 ± 1

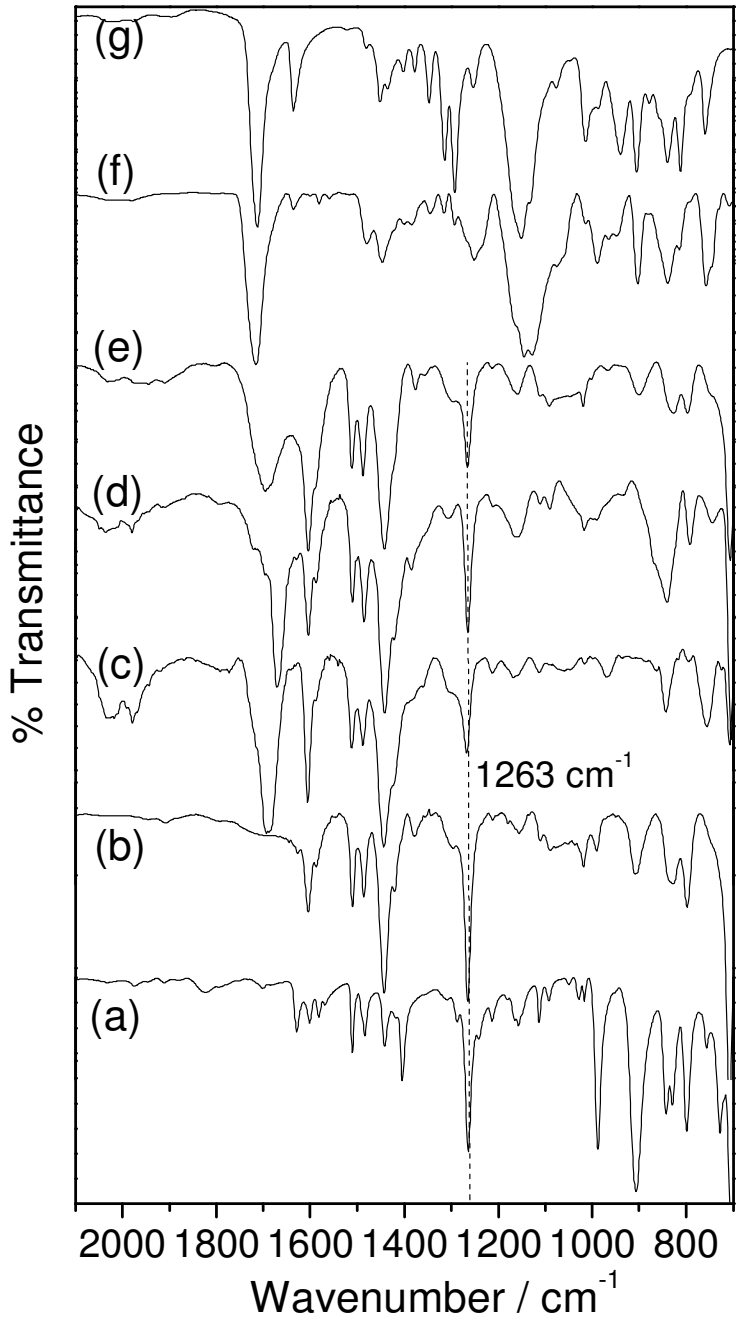

Figure 4.1: Infrared spectra of: (a) vinylbenzyl chloride monomer; (b) pulsed plasma deposited poly(vinylbenzyl chloride); (c) pulsed plasma deposited poly(vinylbenzyl chloride) following immersion in cresyl violet perchlorate solution; (d) following 16 h water rinsing of (c) at 22 °C and drying for 16 h in air at 22 °C; (e) following immersion of (d) in water at 60 °C for 1 h and then drying for 16 h in air at 22 °C; (f) poly(glycidyl methacrylate) ATRP grafted onto (e); and (g) glycidyl methacrylate monomer.

A linear film deposition rate of 193 ± 34 nm min^{-1} and water contact angle values of 80 ± 1° (not hydrophilic) were measured. Optical micrographs and fluorescence images (gathered at the excitation wavelength for cresyl violet perchlorate) were featureless, thereby confirming that the deposited films were smooth and homogenous, Figures 2.1 and 4.2.

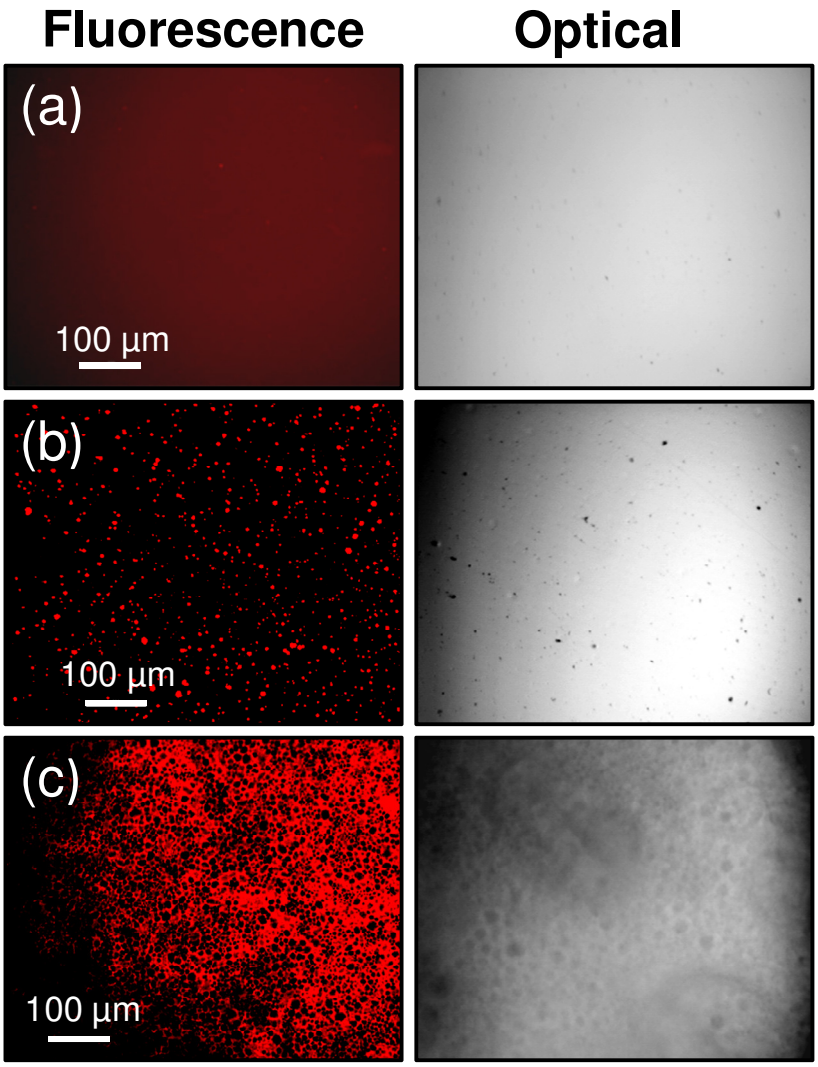

Figure 4.2: Fluorescence and corresponding optical micrographs (x10 magnification) of pulsed plasma deposited poly(vinylbenzyl chloride) films: (a) as deposited; (b) following immersion in cresyl violet solution; and (c) following immersion in cresyl violet perchlorate solution, rinsing in water at 22 °C for 16 h, soaking in water at 60 °C for 60 min, and then drying in air at 22 °C for 16 h.

4.3.2 Interaction with Cresyl Violet Perchlorate Amphiphile

Fluorescence microscopy showed that immersion of pulsed plasma deposited poly(vinylbenzyl chloride) films in cresyl violet perchlorate solution for 16 h resulted in uptake of the fluorophore, Figure 4.2. Subsurface penetration of cresyl violet perchlorate was evident by the greater number of crystals detected by fluorescence microscopy compared to those visible at the surface by optical microscopy, Figure 4.2. Furthermore, XPS elemental analysis confirmed the presence of cresyl violet perchlorate on the surface of pulsed plasma deposited layers via detection of N(1s) and O(1s) fluorophore signals, Table 4.1. Infrared spectroscopy identified a broad absorbance centred at 1690 cm^{-1} (H-O-H bend attributed to the crystallisation of water associated with cresyl violet perchlorate),[31,32] Figure 4.1. This was found to be absent when *N,N*-dimethylformamide was employed instead as the solvent for cresyl violet perchlorate under otherwise identical conditions (*N,N*-dimethylformamide is an alternative polar solvent that dissolves cresyl violet perchlorate).[33] Retention of the benzyl chloride infrared absorbances confirmed that no chemical changes to the polymer bulk had taken place during contact with aqueous cresyl violet perchlorate solution, Figure 4.1.

In addition to the aforementioned macroscale examination by fluorescence and optical microscopy, AFM was employed to monitor the microscale. Tapping mode height images confirmed that pulsed plasma deposited poly(vinylbenzyl chloride) surfaces were featureless, and only a slight roughening was visible following 16 h immersion in high purity water and then drying in air at 22 °C for 16 h, Figure 4.3. In contrast, immersion in aqueous cresyl violet perchlorate solution for 16 h and then drying in air at 22 °C for 16 h gave rise to crater formation around crystals on the film surface. Subsequent rinsing of these samples in high purity water at room temperature for 16 h removed the crystals to yield additional crater features. Partial removal of cresyl violet perchlorate from the surface during rinsing is supported by XPS analysis, which indicated a corresponding drop in surface oxygen and nitrogen content associated with the fluorophore, Table 4.1 and Scheme 4.1.

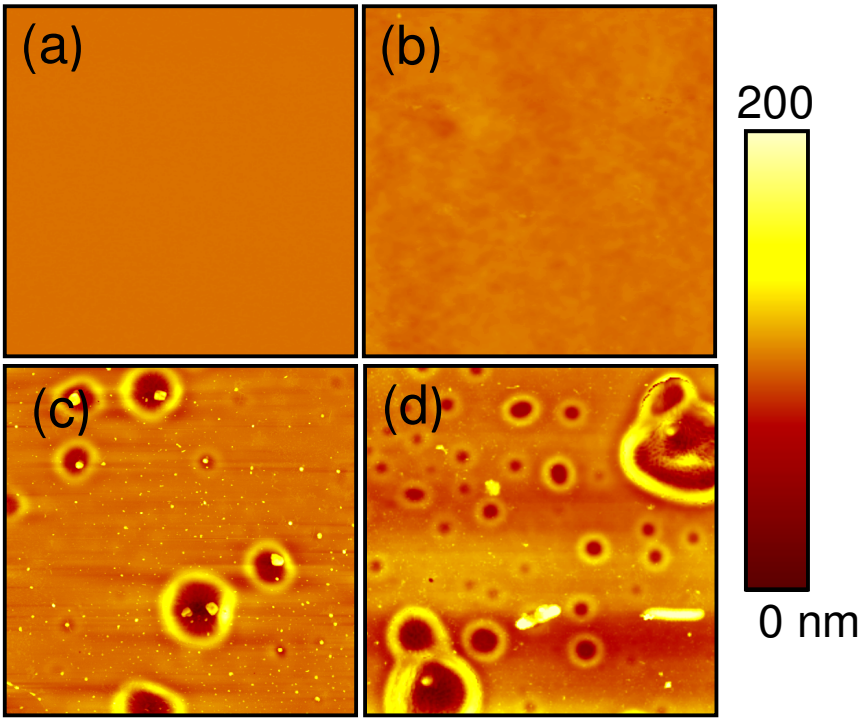

Figure 4.3: 20 µm x 20 µm AFM micrographs of pulsed plasma deposited poly(vinylbenzyl chloride) surfaces: (a) as deposited; (b) following rinsing in high purity water for 16 h and then drying in air at 22 °C for 16 h; (c) following 16 h immersion in aqueous cresyl violet perchlorate solution; and (d) following rinsing of (c) in high purity water for 16 h and then drying in air at 22 °C for 16 h.

Interactions between cresyl violet perchlorate and the pulsed plasma deposited poly(vinylbenzyl chloride) films was further investigated using 4-methylbenzyl chloride as an analogue to represent the pendant benzyl chloride functionality contained in the pulsed plasma deposited layers, Structures 4.1 and 4.2. Infrared spectra taken for 1 g dm^{-3} solutions of cresyl violet perchlorate in 4-methylbenzyl chloride showed no perturbation in the position or intensity of the fingerprint region infrared absorbances for 4-methylbenzyl chloride, thereby providing further confirmation that no chemical reaction is to be expected to occur between the pulsed plasma deposited poly(vinylbenzyl chloride) layers and cresyl violet perchlorate, Figure 4.4. Moreover, subtraction of the 4-methylbenzyl chloride infrared spectrum from that of the solution yielded the characteristic absorbances of cresyl violet perchlorate. These absorbances were comparable in width to those measured for cresyl violet perchlorate dissolved in water, and notably sharper

than those observed for the bulk crystalline material, Table 4.2. This is indicative of free rotation in both liquids, i.e., cresyl violet perchlorate can be solvated by both water and 4-methylbenzyl chloride (and therefore poly(vinylbenzyl chloride)).

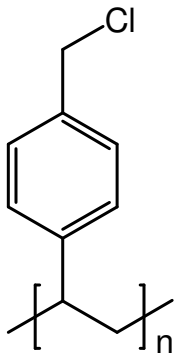

Structure 4.1: Poly(vinylbenzyl chloride).

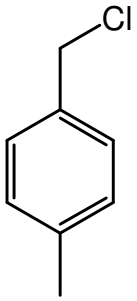

Structure 4.2: 4-methylbenzyl chloride.

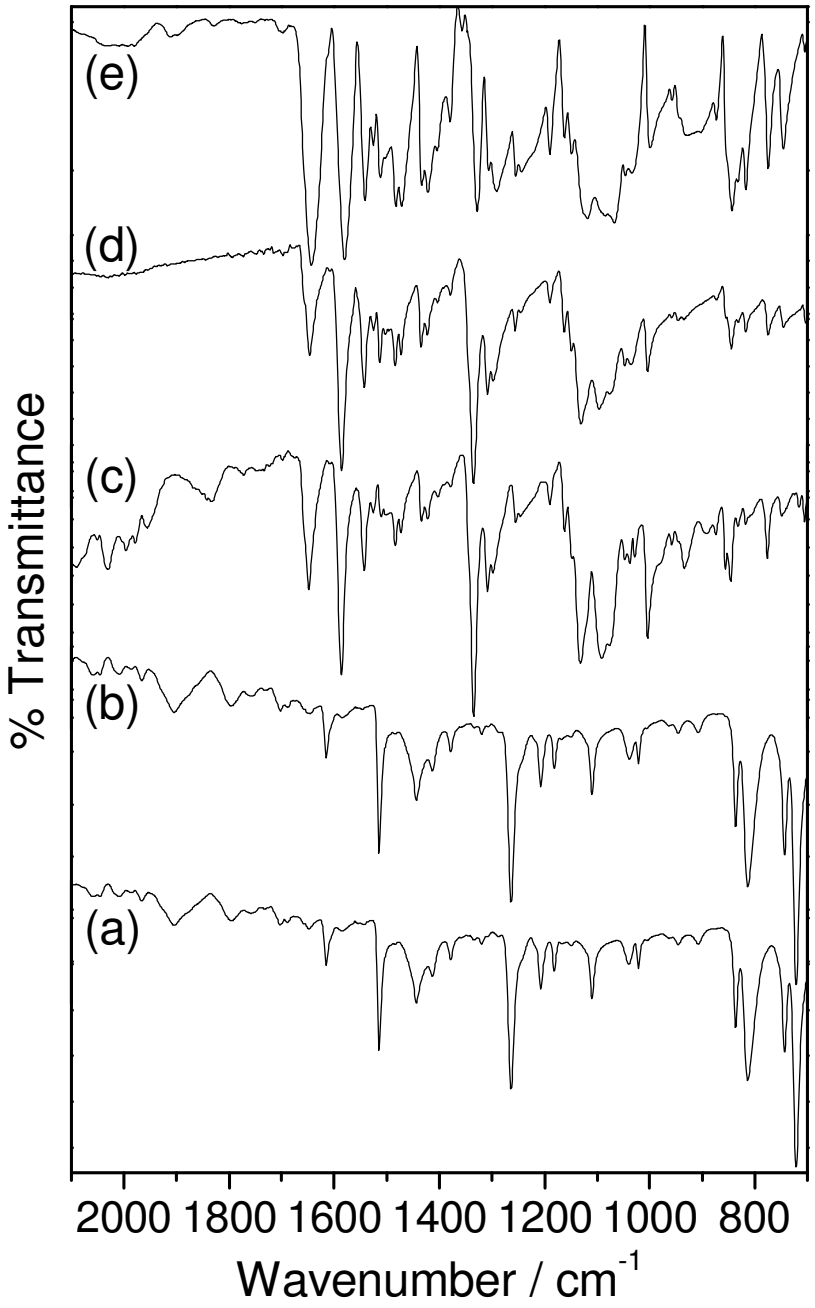

Figure 4.4: Infrared spectra of (a) 4-methylbenzyl chloride; (b) 0.1 mg dm^{-3} solution of cresyl violet perchlorate in 4-methylbenzyl chloride; (c) solvent subtracted spectrum of cresyl violet perchlorate dissolved in 4-methylbenzyl chloride; (d) solvent subtracted spectrum cresyl violet perchlorate dissolved in water; and (e) cresyl violet perchlorate bulk crystalline material.

Table 4.2: Infrared full-width-at-half-maximum (FHWM) peak widths corresponding to Figure 4.4.

***Absorbance*[34]**	***Peak FWHM*** *(cm^{-1})*		
	4-Methylbenzyl chloride Solution	**Water Solution**	**Bulk Crystal**
1642 cm^{-1} (in plane fused ring vibration)	20	23	36
1579 cm^{-1} (NH bending of amino groups)	15	18	26
1543 cm^{-1} (NH_2 out-of-plane bend)	10	11	17

4.3.3 Macroporous (polyHIPE) Structure Formation

In order to create macropores, the aforementioned samples (which had been immersed in aqueous cresyl violet perchlorate solution and rinsed in water) were stored in high purity water for 1 h at 60 °C. During this period, the polymer layer appearance changed from translucent (prior to heating) to opaque, and remained so upon subsequent drying in air. Fluorescence and optical micrographs revealed an interconnected porous structure (pore diameters of 1 – 10 µm) which is comparable to the 3D pore geometry of conventional poly(vinylbenzyl chloride) polyHIPE structures,[15,35] Figure 4.2. These macropores were clearly visible by high-resolution scanning electron microscopy (SEM), Figure 4.5. Moreover, the smooth and largely spherical pore morphology is consistent with solvent templating.[36,37,38] Furthermore, pore diameters (up to 10 µm) greatly exceed the dimensions of cresyl perchlorate crystals observed on poly(vinylbenzyl chloride) surfaces (< 1 µm) thereby eliminating crystal templating as an explanation for pore formation, Figures 4.3 and 4.5. Cross-sectional SEM micrographs confirm that porosity extends throughout the polymer films, which are distended from an initial thickness of 3 µm to 10 µm. These measurements effectively eliminate partial dissolution of plasmachemical polymer layers as being an alternative explanation for the creation of pores.[29]

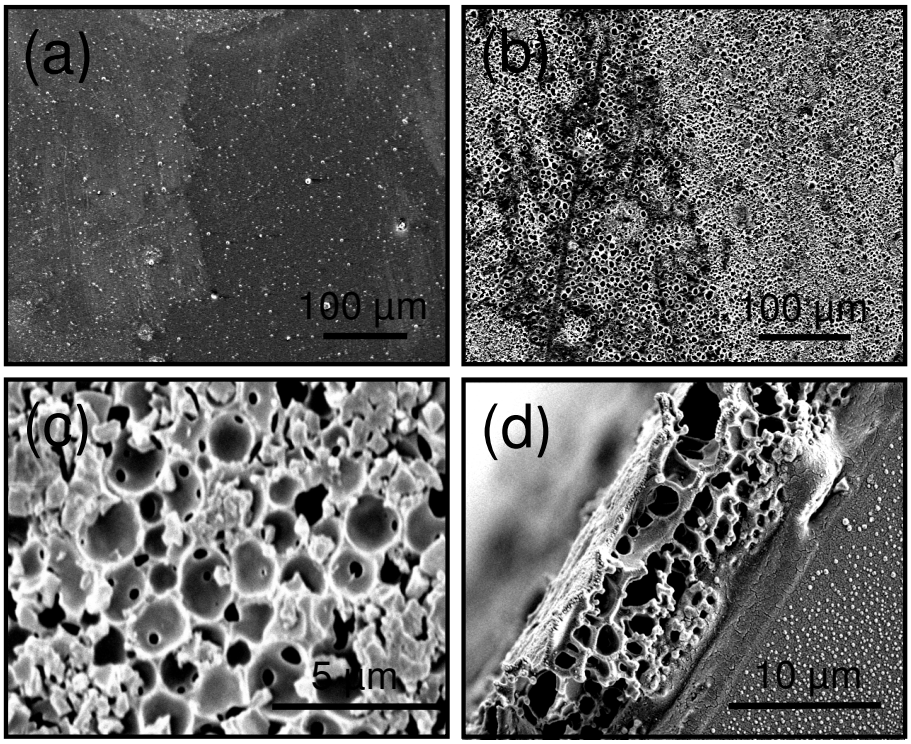

Figure 4.5: SEM images of pulsed plasma deposited poly(vinylbenzyl chloride) following 16 h immersion in aqueous cresyl violet perchlorate solution and then: (a) subsequent immersion in water at 22 °C for 1 h and drying in air at 22 °C for 16 h; (b) – (d) subsequent immersion in water at 60 °C for 1 h and drying in air at 22 °C for 16 h, where (d) corresponds to the cross-section. The pore diameters range between 1 – 10 µm. The interconnecting pore hole size range is 201 ± 65 nm in diameter. The pore wall thickness range is 172 ± 80 nm.

A series of control experiments using alternative reagents were undertaken to further elucidate the mechanism of pore formation. These employed identical conditions to those already used to generate the macroporous structures in pulsed plasma deposited poly(vinylbenzyl chloride) films (i.e., 16 h immersion in dissolved cresyl violet perchlorate solution, 16 h rinsing in solvent at 22 °C, immersion in solvent at 60 °C for 1 h, and air drying). First of all, rinsing the pulsed plasma deposited poly(vinylbenzyl chloride) films with only deionised water (in the absence of cresyl violet perchlorate) produced no porosity (featureless AFM, fluorescence and optical micrographs), thereby confirming that cresyl violet perchlorate plays a critical role in pore formation. Replacement of water with *N,N*-dimethylformamide (an alternative polar solvent) throughout also resulted in the absence of porosity,

which demonstrates the importance of water for templating. Finally, the choice of sodium dodecyl sulphate as a different amphiphile to cresyl violet perchlorate for mediating the interaction between water and pulsed plasma deposited poly(vinylbenzyl chloride) films (16 h immersion in 0.5 % (w/v) aqueous sodium dodecyl sulphate solution, followed by rinsing in water, heating at 60 °C in water, and drying) caused the appearance of the polymer film to change from translucent to opaque during heating, and SEM images taken after drying revealed the formation of macroporous (polyHIPE) structures, thereby confirming that amphiphilic surfactant action between water and pulsed plasma deposited poly(vinylbenzyl chloride) underpins the formation of macroporous structures, Figure 4.6.

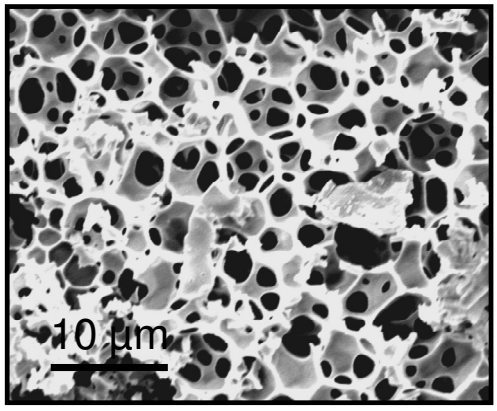

Figure 4.6: SEM image of pulsed plasma deposited poly(vinylbenzyl chloride) following immersion in aqueous sodium dodecyl sulphate solution at 22 °C, then immersion in water at 60 °C for 1 h, and finally drying in air at 22 °C for 16 h.

4.3.4 Surface Functionalisation of Macropores

Surface-initiated ATRP has previously been performed on conventional polyHIPE materials by incorporating bromoester-functionalised styrene initiators into the starting emulsion.[39,40,41] Pulsed plasma deposited poly(vinylbenzyl chloride) layers have previously been used for the initiation of atom transfer radical polymerization (ATRP) to create polymer brushes[42] and the infrared spectra of fabricated porous plasmachemical poly(vinylbenzyl chloride) films indicated retention of the ATRP initiating benzyl chloride functionality, Figure 4.1. Therefore ATRP grafting of glycidyl methacrylate onto the macroporous films was undertaken, and ATR infrared spectroscopy showed characteristic signature absorbances of poly(glycidyl methacrylate)[31,43] at 1726 cm^{-1} (C=O ester stretch, instead of 1714 cm^{-1} for the monomer due to conjugation with the vinyl group), 1152 cm^{-1} (C-O stretch), 1254 cm^{-1} (epoxide ring breathing), 906 cm^{-1} (antisymmetric epoxide ring deformation), and 841 cm^{-1} (symmetrical epoxide ring deformation), Figure 4.1. Absence of the glycidyl methacrylate monomer vinyl absorbances at 1637 cm^{-1} (C=C stretch) and 941 cm^{-1} (vinyl CH_2 wag) provided additional evidence for ATRP having taken place.

Subsequent fluorescent tagging of the poly(glycidyl methacrylate) brushes via nucleophilic ring opening of the epoxide centres was carried out using a dilute solution of Alexafluor 350 Cadaverine dye, Scheme 4.2. Fluorescence microscopy confirmed reaction of the fluorophore with the poly(glycidyl methacrylate) brushes, Figure 4.7. Imaging at the excitation wavelengths of 640 nm and 360 nm for both cresyl violet perchlorate and Alexafluor 350 Cadaverine dye respectively confirmed the grafting of poly(glycidyl methacrylate) brushes directly onto the underlying porous structure, Figure 4.7.

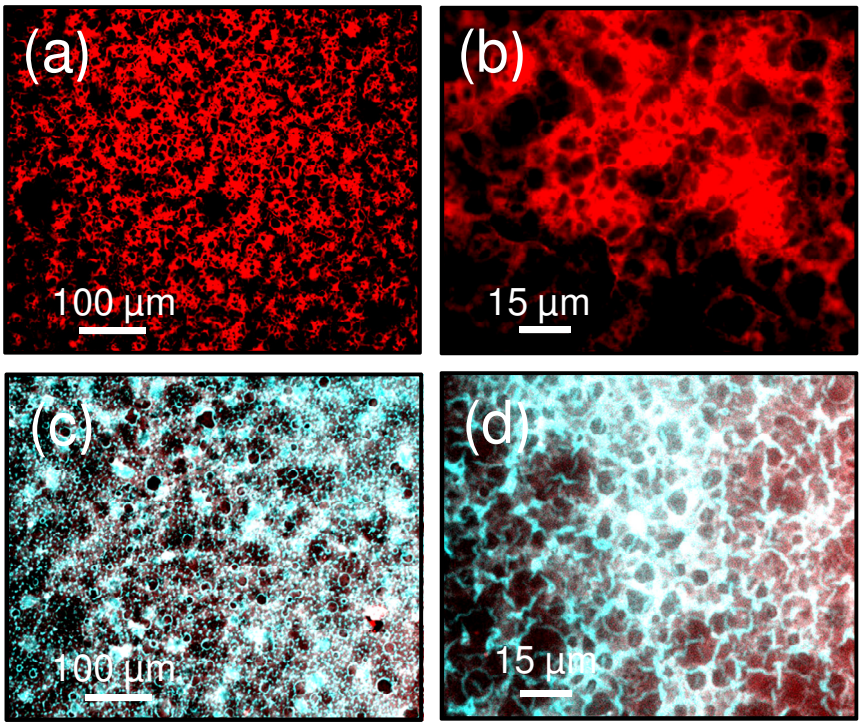

Figure 4.7: Fluorescence micrographs of pulsed plasma deposited poly(vinylbenzyl chloride): (a)-(b) following immersion in aqueous cresyl violet perchlorate solution for 16 h, and then rinsing in water at 60 °C for 1 h (red excitation at 640 nm for cresyl violet perchlorate); and (c)-(d) following exposure of (a) and (b) to ATRP grafting conditions for glycidyl methacrylate for 4 h and then immersion in Alexafluor 350 Cadaverine dye (excitation wavelengths for cresyl violet perchlorate (640 nm - red) and Alexafluor 350 Cadaverine dye (360 nm - blue)).

4.3.5 Polymer Brush Swelling and Collapse

ATRP grafted poly(glycidyl methacrylate) brushes tagged with Alexafluor 350 Cadaverine dye have previously been shown to exhibit solvent responsive behaviour, Figure 3.8. Owing to the hydrophilic nature of the fluorophore, these tagged brushes swell upon exposure to water, which in turn can be removed by exposure to hygroscopic organic solvents. AFM topography measurements of such ATRP grafting of poly(glycidyl methacrylate) onto macroporous poly(vinylbenzyl chloride), followed by reaction with Alexafluor 350 Cadaverine dye and extensive aqueous rinsing, showed complete coverage of pore features, thereby indicating that the swollen tagged poly(glycidyl methacrylate) brushes have filled the pores, Figure 4.8. Furthermore, the underlying porous poly(vinylbenzyl chloride) structure could

be observed using fluorescence microscopy taken at the excitation wavelength for cresyl violet perchlorate (640 nm - red), whilst those taken using the excitation wavelength of Alexafluor 350 Cadaverine dye (360 nm - blue) over the same area showed very little contrast, indicating the presence of the tagged polymer brushes across the entire pore structure. Water removal from these layers was accomplished by soaking in a hygroscopic solvent (tetrahydrofuran), which resulted in the restoration of porosity, as verified by both by fluorescence microscopy and AFM height images, Figure 4.8. This behaviour was shown to be reversible.

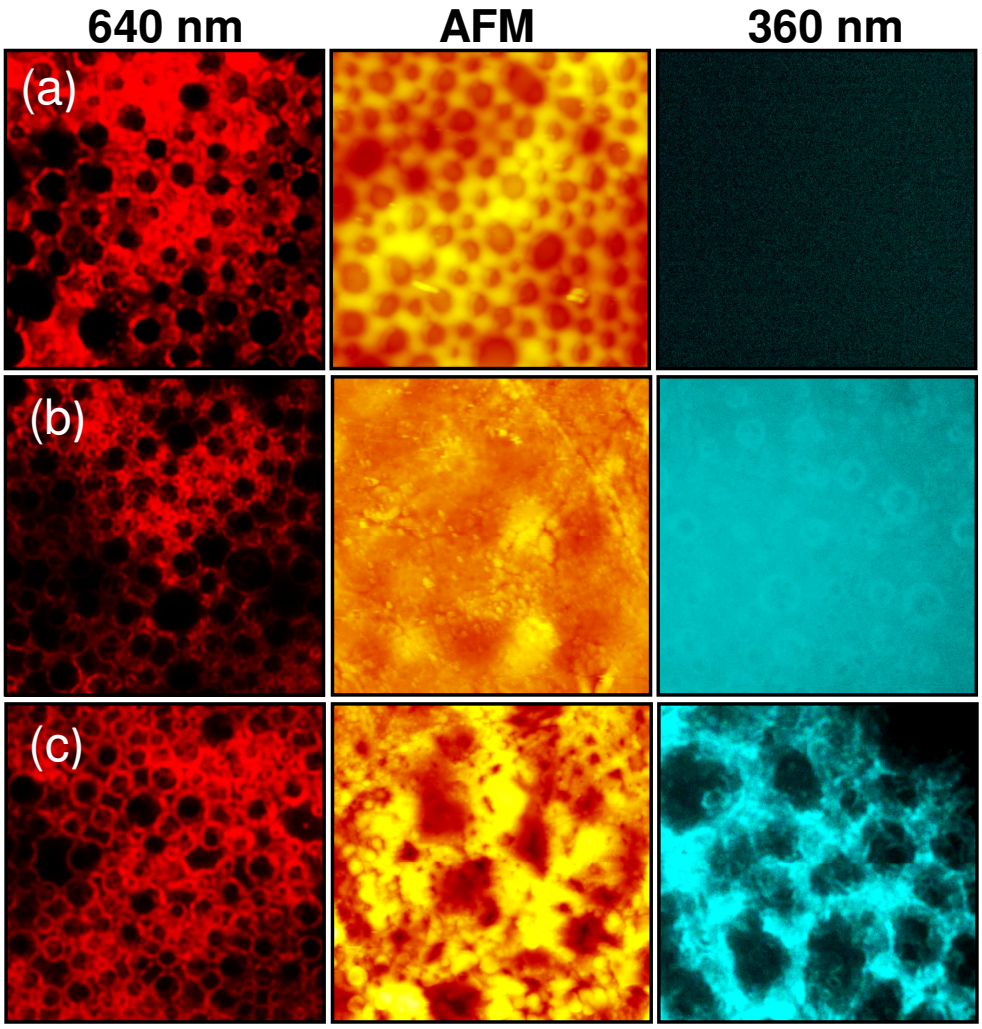

Figure 4.8: 50 µm x 50 µm tapping mode AFM images (z scale is 1500 nm) and corresponding fluorescence micrographs (excitation wavelengths for cresyl violet perchlorate (640 nm - red) and Alexafluor 350 Cadaverine dye (360 nm - blue)) of pulsed plasma deposited poly(vinylbenzyl chloride): (a) following immersion in aqueous cresyl violet perchlorate solution, and then rinsing at 60 ℃ for 1 h; (b) following exposure of (a) to ATRP grafting conditions for glycidyl methacrylate for 12 h, brief immersion in Alexafluor 350 Cadaverine dye, followed by 16 h aqueous rinsing at 22 ℃; and (c) following immersion of (b) in tetrahydrofuran and drying.

4.4 DISCUSSION

Macroporous polymers can be fabricated using high internal phase emulsion (HIPE) techniques, where the continuous organic phase consists of the monomer templated around the internal aqueous phase *prior* to polymerization, and then the aqueous phase is removed to leave behind a micron-scale interconnected porous structure.[44] These emulsions are necessarily stabilised by the addition of surfactants (which serve to lower the interfacial energy between the two phases, and hence prevent separation), but nonetheless their formation involves extensive mixing of the organic and aqueous phases. In marked contrast, the present study has demonstrated a completely different approach, where polymerization takes place prior to pore formation. The porous film structure is indicative of emulsion templating (smooth, spherical interconnected pores) and no pore formation was observed following exposure to miscible solvents. This indicates that an emulsion formed *spontaneously* at elevated temperatures between the pulsed plasma deposited polymer (impregnated with amphiphilic species) and water to create macroporous structures. Ordinarily emulsions require the input of work (mixing) for formation, but no mechanical action was used in the present case. Spontaneous emulsion formation is well documented in the case of microemulsions, where the addition of a significant amount of a mediating (surfactant) species lowers interfacial energy between two immiscible phases to such an extent that the contacting area is spontaneously maximised by emulsion formation.[45,46] Although the dimensions of generated pores obviously negates comparable microemulsion formation, the observation of surface craters around cresyl violet perchlorate crystals does indicate spontaneous maximisation of the water-pulsed plasma deposited poly(vinylbenzyl chloride) interface even at room temperature, pointing towards a related mechanism for emulsion formation, Figure 4.3. In the case of cresyl violet perchlorate, favourable interaction with both water and pulsed plasma deposited poly(vinylbenzyl chloride) can be understood by consideration of its molecular structure, Scheme 4.1. The ionic component of the molecule confers hydrophilicity, whilst the extended aromatic structure facilitates interaction with the benzyl chloride moieties contained within the

pulsed plasma deposited poly(vinylbenzyl chloride) film. Control experiments using 4-methylbenzyl chloride has confirmed this behaviour, Figure 4.4. Indeed, many similar organic dyes have previously been shown to disperse within aromatic polymer matrices via π-π interactions.[47,48] The utilisation of an alternative amphiphilic species (sodium dodecyl sulphate, which is known to mediate interactions between vinylbenzyl chloride and water[49,50]) has also been shown to impart porosity. In contrast, organic solvents (such as *N,N*-dimethylformamide) are less expected to form emulsions with polymers due to their higher miscibility.[51] Indeed, poly(vinylbenzyl chloride) has been reported to dissolve in *N,N*-dimethylformamide,[52] which helps to account for why the pulsed plasma deposited poly(vinylbenzyl chloride) layers are not templated by *N,N*-dimethylformamide solutions.

In keeping with conventional bulk emulsion polymerization methods, a finite amount of the surfactant is retained.[53] This is due to the equilibrium dispersion of surfactant between organic and aqueous phases. UV-Vis measurements showed that cresyl violet perchlorate partially disperses from aqueous solutions into methyl benzyl chloride liquid, and vice versa following a 16 h equilibration period. In the present study, the retention of a very small amount of cresyl violet perchlorate fluorophore within the porous polymer films has allowed fluorescence microscopy to be used as a tool, which offers the advantage of film inspection under ambient conditions (in contrast to SEM) as well as examination of subsurface morphology.

Apart from the mediating effect of surfactants, the stability of conventional water in oil microemulsions can also be enhanced by increasing the viscosity of the organic phase.[54] For the case of pulsed plasma deposited poly(vinylbenzyl chloride), although these films are not sufficiently flexible at room temperature to form emulsions, the plasmachemical layer can be considered to become a highly viscous organic phase at elevated temperatures. AFM height images show shallow crater formation at the film surface following exposure to cresyl violet perchlorate solution under ambient conditions, which is indicative of a limited amount of film deformation occurring at the solid-liquid interface around water droplets in order to maximise interfacial contact, Figure 4.3. This effect is enhanced at raised temperatures, with the greater polymer mobility allowing films to stretch

around water droplets to create an emulsion. This is akin to the thermoplastic behaviour of conventional poly(vinylbenzyl chloride), which becomes more flexible at elevated temperatures[55,56] (T_g of poly(vinylbenzyl chloride) for a molecular weight of 100,000 g mol^{-1} has been reported to be 70 °C[57]). Indeed, fluorescence images of 3 µm thick spin-coated poly(vinylbenzyl chloride) samples, treated in the same way as the plasma deposited samples (16 h exposure to cresyl violet solution, followed by 16 h rinsing in high purity water and 1 h in water at 60 °C) indicated that some interaction had occurred to form crater-like features, Figure 4.9. However, the polymer films appeared translucent and homogenous under the optical microscope, and heating frequently led to delamination of spin-coated films. It is speculated that water-filled porous structures may have formed during the heating stage, and then collapsed prior to characterisation, although more experiments are needed to confirm this. It is anticipated that optimisation of the molecular weight and degree of cross-linking for conventional poly(vinylbenzyl chloride) could potentially yield comparable macroporous films using the methodology described in the present study, although these parameters are not known for either the plasma deposited or spin coated layers used at present.

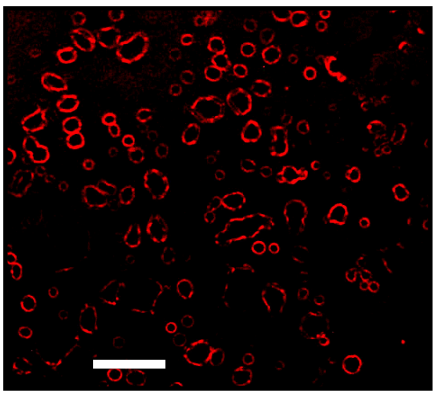

Figure 4.9: Fluorescence micrograph of spin coated poly(vinylbenzyl chloride) following 16 h exposure to cresyl violet solution, followed by 16 h rinsing in high purity water and 1 h in water at 60 °C. Scale bar corresponds to 100 µm.

The proposed mechanism for pore generation is therefore dependent upon a combination of surfactant action and polymer flexibility. A key feature is that unlike traditional approaches where polymerization takes place post emulsion (pore) formation, the present method effectively decouples the

polymerization step completely from emulsion formation. This is important given that conventional emulsions used to fabricate polyHIPE materials are highly complex formulations comprising solvents, surfactants, monomer(s), cross-linker, and polymerization initiators, where the molecular structure and concentration of each of these components affects emulsion stability and the resulting pore dimensions and morphology.[44,58] In such cases, porosity is also influenced by further factors including the material of the container contacting the emulsion during polymerization, temperature, and mixing speed.[44] Overall this means that a delicate balance of process conditions is required to reproducibly fabricate conventional open cell macroporous polymers. By decoupling the polymerization step, the present method allows for better control over the macromolecular architecture for a variety of surfactants (including cresyl violet perchlorate, which is not ordinarily considered to behave as a surfactant due to its small size). Raising the temperature can be expected to affect the flexibility of the pulsed plasma deposited poly(vinylbenzyl chloride) layer during the pore formation step, which will lead to increased coalescence of water phase droplets to yield larger pore sizes (analogous to decreased viscosity of the organic phase of a standard HIPE mixture[57,56,59]). Other variables for controlling pore size could include pressure[60] and surfactant concentration.[61] The main practical advantages of the described technique are that the plasmachemical deposition step is substrate-independent and solventless, whilst the spontaneous emulsion formation requires only the use of environmentally friendly aqueous solutions. A straightforward extension of this approach can be envisaged for the fabrication of a whole host of functionalised macroporous structures, given the wide range of well-defined plasmachemical deposited functional layers that are available. In addition, the generated macroporous structures can be further functionalised by either plasmachemical or conventional wet techniques (e.g., ATRP), which broadens the scope for potential applications (given the wide array of monomers and functionalities available - including bioactive hydrophilic polymers[62,63]).

4.5 CONCLUSIONS

Macroporous (polyHIPE) structures can be fabricated by impregnation of plasmachemical deposited polymeric films with an amphiphilic templating species followed by spontaneous emulsion formation. This enables the decoupling of pore functionalisation from pore formation. For instance, subsequent atom transfer radical polymerization (ATRP) of polymer brushes onto the pore surfaces facilitates pore size actuation. These functionalised macroporous scaffold structures have potential application for catalysis, fuel cells, gas storage, and biotechnology.

4.6 REFERENCES

(1) Furukawa, H.; Yaghi, O. M. *J. Am. Chem. Soc.* **2009**, *131*, 8875.

(2) Wang, H.; Gao, Q.; Hu, J. *J. Am. Chem. Soc.* **2009**, *131*, 7016.

(3) Ding, Y.; Chen, M.; Erlebacher, J. *J. Am. Chem. Soc.* **2004**, *126*, 6876.

(4) Yu, J-S.; Kang, S.; Yoon, S. B.; Chai, G. *J. Am. Chem. Soc.* **2002**, *124*, 9382.

(5) Pierre, S. J.; Thies, J. C.; Dureault, A.; Cameron, N. R.; van Hest, J. C. M.; Carette, N.; Michon, T.; Weberskirch, R. *Adv. Mater.* **2006**, *18*, 1822.

(6) Zhao, C.; Danish, E.; Cameron, N. R.; Kataky, R. *J. Mater. Chem.* **2007**, *17*, 2446.

(7) Ito, Y.; Ochiai, Y.; Park, Y. S.; Imanishi, Y. *J. Am. Chem. Soc.* **1997**, *119*, 1619.

(8) Mellors, J. S.; Jorgenson, J. W. *Anal. Chem.* **2004**, *76*, 5441.

(9) Bedair, M.; El Rassi, Z. *J. Chromatogr. A* **2005**, *1079*, 236.

(10) Barbetta, A.; Massimi, M.; Devirgiliis, L. C.; Dentini, M. *Biomacromolecules* **2006**, *7*, 3059.

(11) Bokhari, M.; Carnachan, R. J.; Przyborski S. A.; Cameron, N. R. *J. Mater. Chem.* **2007**, *17*, 4088.

(12) Kjeang, E.; Michel, R.; Harrington, D. A.; Djilali, N.; Sinton, D. *J. Am. Chem. Soc.* **2008**, *130*, 4000.

(13) Simms, H. M.; Brotherton, C. M.; Good, B. T.; Davis, R. H.; Anseth, K. S.; Bowman, C. N. *Lab Chip* **2005**, *5*, 151.

(14) Li, X.; Coffer, J. L.; Chen, Y.; Pinizzotto, R. F.; Newey, J.; Canham, L. T. *J. Am. Chem. Soc.* **1998**, *120*, 11706.

(15) Kimmins, S. D.; Cameron, N. R. *Adv. Funct. Mater.* **2011**, *21*, 211.

(16) Burdick, J. A.; Frankel, D.; Dernell, W. S.; Anseth, K. S. *Biomaterials* **2003**, *24*, 1613.

(17) Jiang, P.; McFarland, M. J. *J. Am. Chem. Soc.* **2004**, *126*, 13778.

(18) Xu, H.; Ling, X. Y.; van Bennekom, J.; Duan, X.; Ludden, M. J. W.; Reinhoudt, D. N.; Wessling, M.; Lammertink, R. G. H.; Huskens, J. *J. Am. Chem. Soc.* **2009**, *131*, 797.

(19) Normatov J.; Silverstein, M. S. *Macromolecules* **2007**, *40,* 8329.

(20) Menner, A.; Powell, R.; Bismarck, A. *Soft Matter* **2006**, *2*, 337.

(21) Youssef, C.; Backov, R.; Treguer, M.; Birot, M.; Deleuze, H. *J. Polym. Sci. A* **2010**, *48*, 2942.

(22) Bunz, U. H. F. *Adv. Mater.* **2006**, *18*, 973.

(23) Biederman H.; Slavínska, D. *Surf. Coat Technol.* **2000**, *125*, 371.

(24) Teare, D. O. H.; Schofield, W. C. E.; Garrod, R. P.; Badyal, J. P. S. *Langmuir* **2005**, *21*, 10818.

(25) Savage, C. R.; Timmons, R. B.; Lin, J. W. *Chem. Mater.* **1991**, *3*, 575.

(26) Ryan, M. E.; Hynes, A. M.; Badyal, J. P. S. *Chem. Mater.* **1996**, *8*, 37.

(27) Badyal, J. P. S. *Chem. Br.* **2001**, *37*, 45.

(28) Øye, G.; Roucoules, V.; Cameron, A. M.; Oates, L. J.; Cameron, N. R.; Steel, P. G.; Badyal, J. P. S.; Davis, B. G.; Coe, D.; Cox, R. *Langmuir* **2002**, *18*, 8996.

(29) Vasilev, K.; Britcher, L.; Casanal, A.; Griesser, H. J. *J. Phys. Chem. B* **2008**, *112,* 10915.

(30) Zelzer, M.; Alexander, M. R. *J. Phys. Chem. B* **2010**, *114,* 569.

(31) Lin-Vien, D.; Colthrup, N. B.; Fateley, W. G.; Grasselli, J. G. *The Handbook of Infrared and Raman Characteristic Frequencies of Organic Molecules*; Academic Press: Boston, U.S.A., 1991.

(32) Horobin, R. W. *Histochemical J.* **1969**, *1*, 231.

(33) Roucoules, V.; Schofield, W. C. E.; Badyal, J. P. S. *J. Mater. Chem.* **2011**, *21*, 16153.

(34) Vogel, E.; Gbureck, A.; Kiefer, W. *J. Mol. Struct.* **2000**, *550-551*, 177.

(35) Barbetta, A.; Cameron, N. R.; Cooper, S. J. *Chem. Commun.* **2000**, 221.

(36) Barbetta, A.; Dentini, M.; Leandri, L.; Ferraris, G.; Coletta, A.; Bernabei, M. *React. Funct. Polym.* **2009**, *69*, 724.

(37) Hainey, P.; Huxham, I. M.; Rowatt, B.; Sherrington D. C.; Tetley, L. *Macromolecules* **1991**, *24*, 117.

(38) Barbetta, A.; Cameron, N. R. *Macromolecules* **2004**, *37,* 3188.

(39) Cummins, D.; Duxbury, C. J.; Quaedflieg, P. J. L. M.; Magusin, P. C. M. M.; Koning, C. E.; Heise, A. *Soft Matter* **2009**, *5*, 804.

(40) Cummins, D.; Wyman, P.; Duxbury, C. J.; Thies, J.; Koning, C. E.; Heise, A. *Chem. Mater.* **2007**, *19,* 5285.

(41) Moine, L.; Deleuze, H.; Maillard, B. *Tetrahedron Letters* **2003**, *44*, 7813.

(42) Teare, D. O. H.; Barwick, D. C.; Schofield, W. C. E.; Garrod, R. P.; Ward, L. J.; Badyal, J. P. S. *Langmuir* **2005**, *21*, 11425.

(43) Tarducci, C.; Kinmond, E. J.; Badyal, J. P. S.; Brewer, S. A.; Willis, C. *Chem. Mater.* **2000**, *12*, 1884.

(44) Cameron, N. R. *Polymer* **2005**, *46*, 1439.

(45) Shahidzadeh, N.; Bonn, D.; Aguerre-Chariol, O.; Meunier, J. *Colloids Surf. A* **1999**, *147*, 375.

(46) Greiner, R. W.; Evans, D. F. *Langmuir* **1990**, *6*, 1793.

(47) Frederikson, P.; Bjørnholm, T.; Madsen, H. G.; Bechgaard, K. *J. Mater. Chem*. **1994**, *4*, 675.

(48) Uda, Y.; Kaneko, F.; Tanigaki, N; Kawaguchi, T. *Adv. Mater*. **2005**, *17*, 1846.

(49) Larpent, C.; Bernard, E.; Richard, J.; Vaslin, S. *React. Funct. Polym*. **1997**, *33*, 49.

(50) Larpent, C.; Bernard, E.; Richard, J.; Vaslin, S. *Macromolecules* **1997**, *30,* 354.

(51) Becker, J. R. *Crude Oil Waxes, Emulsions and Asphaltenes;* PennWell Books: Tulsa, U.S.A.,1997.

(52) Alexandratos, S. D.; Zhu, X. *Macromolecules* **2003**, *36,* 3436.

(53) Gurevitch, I.; Silverstein, M. S. *J. Polymer Sci. A* **2010**, *48*, 1516.

(54) Das, A. K.; Mukesh, D.; Swayambunathan, V.; Kotkar, D. D.; Ghosh, P. K. *Langmuir* **1992**, *8*, 2427.

(55) Ram, A. *Fundamentals of Polymer Engineering;* Plenum Press: New York, U.S.A., 1997.

(56) Baeurle, S. A.; Hotta, A.; Gusev A. A. *Polymer* **2006**, *47*, 6243.

(57) Chen, N.; Maeda, N.; Tirrell, M.; Israelachvili J. *Macromolecules* **2005**, *38*, 3491.

(58) Carnachan, R. J.; Bokhari, M.; Przyborski S. A.; Cameron, N. R. *Soft Matter* **2006**, *2*, 608.

(59) Zhang, S.; Chen, J.; Perchyonok, V. T. *Polymer* **2009**, *50*, 1723.

(60) Eastoe, J.; Robinson, B. H.; Steytler, D. C. *J. Chem. Soc. Faraday Trans.* **1990**, *86*, 511.

(61) Williams, J. M.; Gray, A. J.; Wilkerson, M. H. *Langmuir* **1990**, *6*, 437.

(62) Bontempo, D.; Maynard, H. D. *J. Am. Chem. Soc.* **2005**, *127*, 6508.

(63) Xu, F. J.; Liu, L. Y.; Yang, W. T.; Kang, E. T.; Neoh, K. G. *Biomacromolecules* **2009**, *10*, 1665.

CHAPTER 5

PART 1: NANOPLASMA SURFACE ELECTRIFICATION

5.1.1 INTRODUCTION

Direct nanoscale writing of charge onto surfaces has potential applications for data storage,[1,2] xerography,[3,4] self-assembly,[5,6] and electronics.[7] One powerful and promising tool for such patterning of surface charge is the scanning probe microscope (SPM).[8] It allows spatially localised and controlled electrification of insulators by application of a bias voltage to the sharp SPM probe tip positioned in close proximity to the surface of interest. Detection of the deposited charge can be accomplished by operating the SPM probe in electric field microscopy mode (EFM) with nanoscale lateral resolution. Specifically, two distinct approaches are known for SPM surface electrification: the most common is a contact mode methodology, where the probe tip makes direct contact with the sample surface prior to application of a bias voltage across the probe tip and underlying electrode.[9,10,11,12] Such contact mode electrification has been successfully applied to a whole host of insulators. Reproducibility of data can be problematic, however, given that experimental parameters such as the effective contact area and film thickness govern the efficacy of charge deposition.[13,14,15] Furthermore, there are prerequisites for the film to be ultrathin and in good contact with the conducting back electrode; thus limiting the technique to specially prepared substrates and precluding more widespread applicability.[16] The alternative is non-contact SPM surface charge deposition which is based on localised corona discharge formation, and circumvents the aforementioned drawbacks, as well as minimising damage to both the tip and underlying substrate. In this case, the conducting SPM probe tip is held at a fixed distance above the sample surface whilst a bias voltage is applied between the probe tip and the underlying metallic sample holder (the counter electrode). Due to the extreme curvature of the SPM probe tip (less than 10 nm), the local electric field exceeds the dielectric breakdown of air, resulting in a corona discharge.[17] This approach eliminates any requirement for specially prepared ultrathin films deposited onto conducting substrates. However, to date, it has been limited to some early proof-of-concept studies for polymethylmethacrylate and silicon nitride substrates.[17,18,19]

In this study, spatially confined electrification of a wide range of polymer surfaces is explored by applying a bias voltage to the scanning probe

tip whilst positioned above the sample. The deposited surface charge has subsequently been imaged by electric force microscopy (EFM).

5.1.2 EXPERIMENTAL

5.1.2.1 Sample Preparation

Thin polymer films (thickness 300 – 500 nm) were coated onto silicon wafer pieces (1 cm x 1 cm, 525 ± 25 µm thickness, electrical conductivity of 0.05 – 0.2 S cm^{-1}, MEMC Electronic Materials Inc). Polystyrene (Sigma-Aldrich Inc), polymethylstyrene (Polymer International Ltd), polymethoxystyrene (Polymer International Ltd), polyisopropylstyrene (Polymer International Ltd), polytertbutylstyrene (Polymer International Ltd), polymethylmethacrylate (Sigma-Aldrich Inc), polyhydroxyethylmethacrylate (Sigma-Aldrich Inc) and polychlorostyrene (Polymer International Ltd) were spin cast from 2% w/v solutions in toluene. Polyvinylchloride (Goodfellow Ltd) was spin cast from a 2% w/v solution in tetrahydrofuran. Polyvinylidene fluoride (Aldrich) was spin cast from a 2% w/v solution in *N,N*-dimethylformamide. Polyvinylalcohol (Sigma-Aldrich Inc) and polyethyleneoxide (Sigma-Aldrich Inc) were spin cast from 2% w/v solutions in propan-2-ol. A spin coater (Cammax Precima) operating at 2000 rpm for 30 s was used, and the cast films were allowed to dry under ambient conditions for 16 h. Nylon 6-6 (Goodfellow Ltd) pieces were cut from a sheet, wiped with propan-2-ol, and stuck to silicon wafer using double sided electrically non-conducting adhesive tape (Sellotape, 503874). In all cases, root-mean-square surface roughness was measured by AFM to be less than 2 nm.

5.1.2.2 SPM Charge Deposition

Polymer coated silicon wafer pieces were fixed onto 0.75 mm thick steel sample holder discs using double sided adhesive tape (Sellotape, 503874), and then loaded into a Nanoscope III atomic force microscope which was fitted with control and signal access modules (Digital Instruments). A conducting chromium sputter coated EFM probe tip was used for charge deposition and imaging (MikroMasch, Estonia, NS15/Cr, force constant ~ 40 Nm^{-1}, resonance frequency ~ 270 kHz, nominal tip radius 10 nm). This entailed the application of a bias voltage between the probe tip and the metal sample holder disc using a custom designed high voltage D.C. power supply (±180 V) which was gated through the signal access module. Probe tip movement in the *x*, *y*, and *z* planes, and bias voltage application to the tip

were controlled by Veeco Nanolithography Software (version 5.30r1). The charge deposition protocol comprised disabling tapping mode operation, followed by positioning of the probe tip to a predetermined height above the sample surface (5 – 100 nm), and then switching on the bias voltage for a predetermined time period (10 ms – 20 s).

The overall counter electrode consisted of the polymer layer coated silicon wafer (with its native oxide layer intact) fixed to the electrically grounded metal sample holder disc using double sided adhesive tape, Scheme 5.1.1. The SPM probe tip was effectively separated from the grounded metal sample holder disc by a maximum total distance (D) of 0.65 mm.

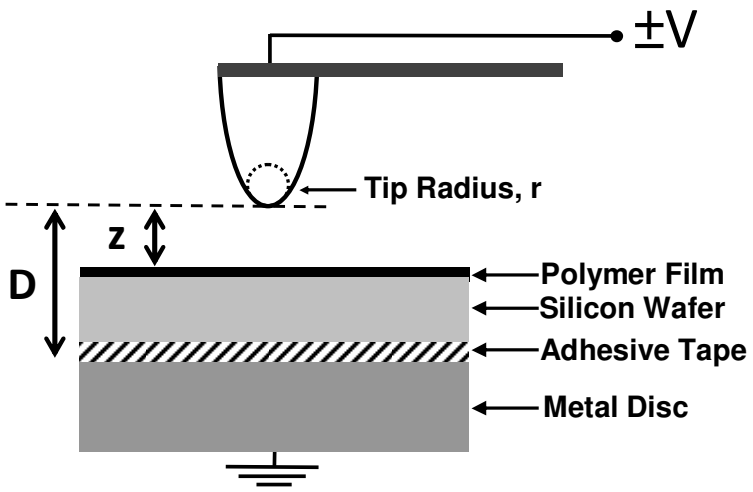

Scheme 5.1.1: SPM corona charging and EFM charge detection. Where D comprises adhesive tape (0.1 mm), silicon wafer (0.525 ± 0.025 mm), and polymer film (300 – 500 nm).

The electric field, E, generated by application of a voltage, V, to the probe tip apex can be approximated using Equation 5.1.[19] The tip of nominal radius r (10 nm) is modelled as a hyperboloid with curvature 1/r, and is separated from the metal sample holder disc by an effective distance D (0.65 mm).

$$E = \frac{V}{D} \frac{\sqrt{\xi(1+\xi)}}{\ln\left(\sqrt{\xi} + \sqrt{1+\xi}\right)} \quad \text{where } \xi = D/r \qquad \text{(Equation 5.1)}$$

By taking the stated values of D and r in conjunction with the reported dielectric strength of air (*E*) as being equal to 3 x 10^6 Vm^{-1},[20,21] the localised dielectric breakdown threshold voltage is calculated using Equation 5.1 to equal approximately 0.187 V; whilst replacement of the insulating adhesive tape with an electrically conducting tape yields a calculated value of approximately 0.079 V. These localised dielectric breakdown threshold voltages are significantly smaller in magnitude than the typical tip bias voltages employed in the present study (>12 V) and, therefore, corona discharge formation is to be expected.

5.1.2.3 Electric Force Microscopy

Following SPM charge deposition, topography and phase shift images were acquired for each surface, Scheme 5.1.2. Intermittent contact (tapping) mode operation of the AFM used for these scan lines involves oscillation of the AFM probe at close to its resonance frequency. The amplitude of this oscillation is chosen such that it drives the tip alternately between the short range attractive and hard sphere repulsive interaction regimes with the surface (it 'taps' the surface).[22] Each contact with the surface results in a loss of energy, thereby dampening tip oscillation in comparison to the free amplitude of tip oscillation in air.[23] The preselected amplitude is maintained via a feedback mechanism whereby the underlying sample position is precisely controlled by piezoelectric elements (which facilitate movements in the xyz planes), while the probe is simultaneously scanned in a raster pattern across the surface.[24,25]

The *modus operandi* for EFM comprises a double pass methodology, whereby the topography for each scan line is initially measured with a grounded conducting SPM probe tip operating in conventional tapping mode close to the surface (tip-to-sample distances < 10 nm[26]), followed by a second scan, during which a much larger preselected separation is maintained between the biased probe tip and sample surface (typically 100 nm), Scheme 5.1.2.[27,28] This large tip-to-substrate separation is chosen such that Van der Waals forces no longer influence the probe tip, and any detected response can be attributed to electrostatic forces because of their weaker distance dependency.[29]

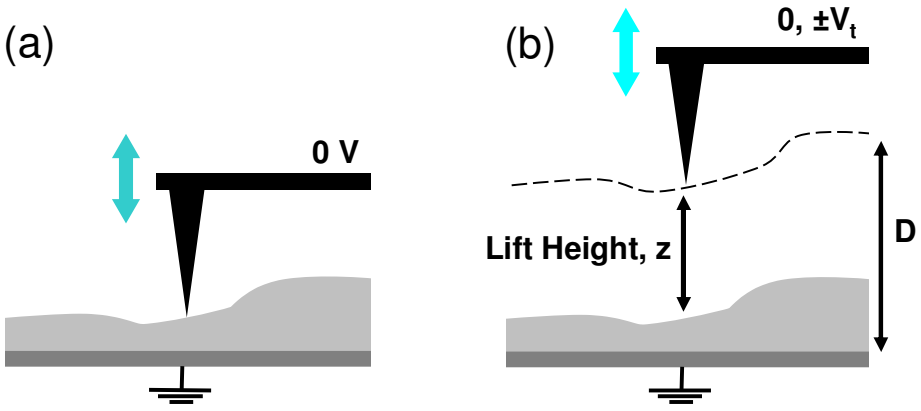

Scheme 5.1.2: SPM scanning for: (a) conventional AFM tapping mode topographical imaging (tip-to-sample distances < 10 nm); and (b) lift mode EFM scanning over the same line for charge imaging.

These electrostatic forces, *F*, acting upon the EFM probe tip during a scan can be broken down into two component forces: the capacitive interaction between the probe tip and underlying counter-electrode (metal disc sample holder), and Coulombic forces due to static charges present on the substrate surface, as detailed in Equation 5.2.[28,30]

$$F = \underbrace{\frac{1}{2}\left(\frac{dC}{dD}\right)V_t^2}_{\text{(Capacitative)}} + \underbrace{E_s Q_t}_{\text{(Coulombic)}} \qquad \text{(Equation 5.2)}$$

The first term corresponds to the capacitative interaction, where dC/dD is the derivative of capacitance between the probe tip and underlying metal disc electrode with respect to their separation (D), and V_t is the voltage applied to the probe tip. In the case of conventional EFM imaging of dielectrics (which requires ultrathin dielectric films to be in conformal contact with an underlying conducting electrode), D is very small and allows the measurement of capacitative interaction between the SPM probe tip and the underlying conducting substrate.[8,31,32,33] This enables electric force imaging of spatial variations in dielectric constant for neutral uncharged samples (the absence of surface charges means that there are no Coulombic forces which leaves only the capacitative interaction component in Equation 5.2).[31,34,35] On the

contrary, for the case where there is charge present at the surface, it becomes difficult to differentiate between contributions made to the detected phase shift component which are attributable to the presence of surface charge versus those contributions belonging to native variations of dielectric constant.

In contrast, for the present experimental set-up, the value of D exceeds the tip radius by many orders of magnitude (0.65 mm and 10 nm respectively), and so capacitance for such systems occurs between the counter metal disc holder electrode and the entire SPM probe (cantilever, conical region and tip apex).[36] The resultant force gradient is proportional to $1/D^3$ and is not localised to the probe tip. Therefore, the contribution towards electrostatic force attributable to capacitance between the probe and underlying metal disc counter electrode can be considered as being constant on the microscale. This explanation is supported by the consistently featureless EFM micrographs observed prior to each electrification experiment (with ±12 V applied to the probe tip).

Consequently, any phase shift responses measured in lift mode must relate to variation of electrostatic interaction between the SPM probe tip and localised surface charge. This contribution is taken into account by the second term E_sQ_t in Equation 5.2, which corresponds to the Coulombic component associated with surface charge, where E_s represents the induced electric field at the probe apex by the static charges present on the substrate surface, and Q_t is the effective charge formed on the probe tip (this includes contributions from both the applied bias V_t and induction due to substrate surface charge). These Coulombic forces operate over the much smaller tip-to-substrate distance, z (lift height, typically 100 nm).

The phase shift, $\Delta\Phi$, arising from these electrostatic forces, *F,* in relation to the probe tip-to-sample separation *z*, is given by Equation 5.3, where, *Q* is the cantilever quality factor and *k* is the cantilever spring constant, Scheme 5.1.2.[37]

$$\Delta\phi \approx \frac{Q}{K}\frac{dF(z)}{dz} \qquad \text{(Equation 5.3)}$$

For AFM imaging, the phase lag (Φ) of the SPM probe tip is defined as the difference between the frequency of oscillation set by the driving transducer and the actual frequency of oscillation of the cantilever, ordinarily expressed in degrees. The measured phase shift ($\Delta\Phi$) represents the difference between the phase lag of the freely vibrating cantilever (Φ_{free}), and the phase lag of the cantilever interacting with the sample ($\Phi_{interacting}$).

$$\Delta \Phi = \Phi_{free} - \Phi_{interacting} \qquad \text{(Equation 5.4)}$$

According to the theory of freely driven oscillators, the phase lag of a freely vibrating cantilever (Φ_{free}) at its maximum amplitude is 90°.[38] The phase lag of the cantilever interacting with a substrate ($\Phi_{interacting}$) is dependent on tip-substrate interactions which shift the resonance frequency of the cantilever (for AFM measurements, the driving frequency of oscillation of the freely vibrating probe is selected to be close to its resonance frequency in order to maximise response to tip-substrate interactions). During conventional AFM topographical tapping mode AFM imaging, this shift in resonance frequency is related to energy dissipation during interactions between the tip and the sample surface, so variations in composition of the sample, local adhesion, friction, viscoelasticity as well as topography all produce phase shifts.[39] In the case of electric force lift mode imaging tip-to-substrate interactions are limited to long-range electric forces which shift the cantilever resonance frequency. If the cantilever experiences a repulsive electric field gradient, the resonance frequency is increased, and the corresponding phase lag drops to below to 90°. The phase shift ($\Delta\Phi$) is therefore positive (contrast in phase image brightens), with its magnitude corresponding to the degree of electrostatic repulsion. Conversely an attractive electric force gradient reduces the resonance frequency, with the interacting phase lag at the driving frequency being raised above 90° to produce a negative phase shift (contrast in phase image darkens).

For the present study, electric force microscopy images were acquired using interleave 'lift mode' operation with ±12 V applied to the probe tip. Data was collected using a double pass technique, where the initial line scan

recorded tapping mode height and phase traces, and then a detection bias voltage was applied during the second pass at a constant height of 100 nm to obtain electric force micrographs. In order to ensure reproducibility, the amplitude set point was kept at 1.2 V, and the scan rate was set to 1 Hz (unless otherwise stated).

5.1.2.4 Water Contact Angle Measurements

Sessile drop contact angle measurements were made using a video capture apparatus (VCA 2500 XE, A.S.T. Products Inc) with 1 µL high purity water droplets (BS 3978 Grade 1) at 22 °C.

5.1.3 RESULTS

5.1.3.1 EFM Charge Deposition onto Polystyrene

Charge deposition onto polystyrene films was initially achieved by application of +140 V to the scanning probe tip for 1 s in conjunction with a tip-to-sample separation of 30 nm. EFM micrographs acquired subsequently (using a lift height of 100 nm and an imaging bias of +12 V) revealed areas of bright contrast corresponding to phase shifts characteristic of a repulsive electric field gradient between the scanning probe tip and sample, Figure 5.1.1. Dissipation of this surface charge was monitored by capturing successive EFM micrographs over time; and these showed rapid decay in the outer region, whilst the centre of the charged spot appeared more stable. No further decay was noted beyond the 120 min observation, Figure 5.1.1.

Next, the effect of probe tip bias on charge deposition was investigated across a range of applied voltages (+60 V, +100 V, +140 V), Figure 5.1.2. Tapping mode AFM height and phase images verified that charge deposition does not damage the surface topography of polystyrene, and only a slight decrease in phase lag is observed directly above the poled areas. The polarity of deposited charge was illustrated by comparing EFM micrographs taken using +12 V with those taken using -12 V applied to the probe tip, which show areas of enhanced and diminished brightness respectively corresponding to repulsive and attractive electric field gradients. In the case of the +12 V EFM micrographs, dark spots, characteristic of electrostatic attraction, were evident at the centre of the repulsive bright regions when higher probe tip biases were applied during the charge deposition step. This can be explained in terms of an induced negative charge acting upon the probe tip as it scans over the most highly charged positive regions.[17] To corroborate this, application of a greater voltage to the probe tip (+20 V) yielded phase shifts characteristic of a repulsive field gradient over the entirety of the charged regions, Figure 5.1.2. This illustrates that the regions of the substrate surface corresponding to the apparent electrostatic attraction noted in the +12 V EFM micrographs are in fact also positively charged; otherwise these regions would remain dark in the +20 V EFM micrographs.

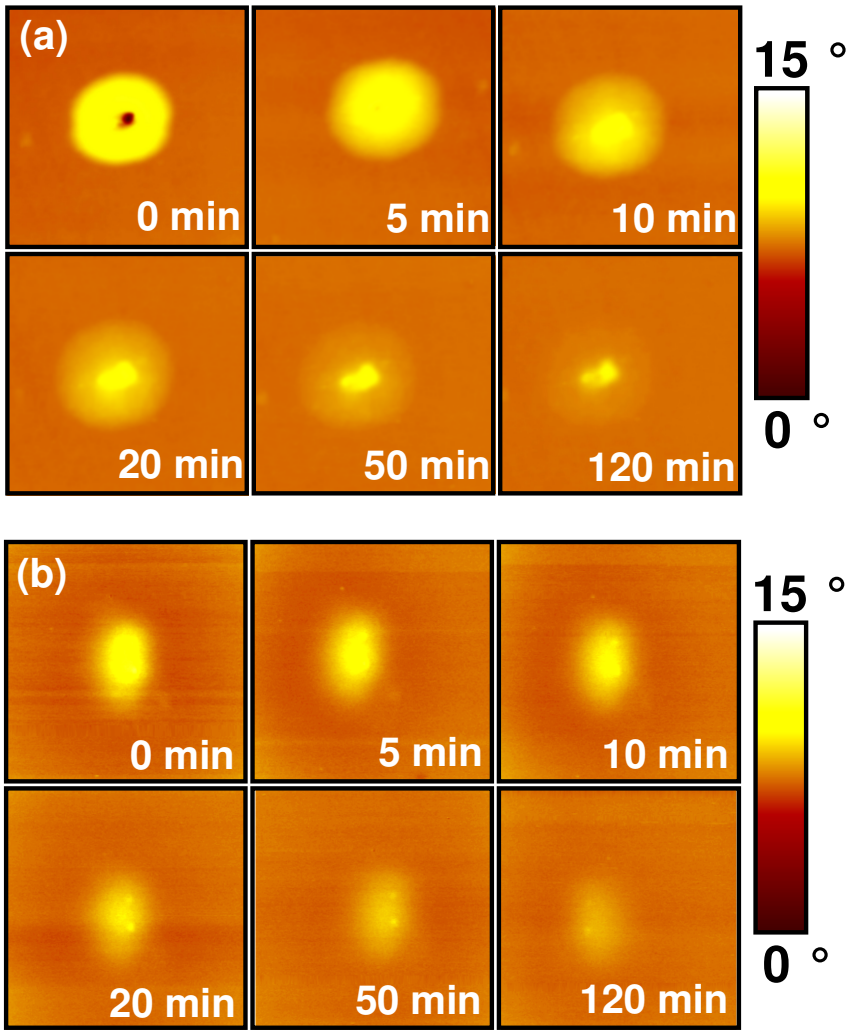

Figure 5.1.1 (a): 20 µm x 20 µm EFM micrographs of polystyrene taken at various times following the application of +140 V for 1 s using a 30 nm probe tip-to-sample separation. EFM micrographs were acquired by scanning at a lift height of 100 nm with +12 V applied to the probe tip. (b): 10 µm x 10 µm EFM micrographs of polystyrene taken at various times following the application of -160 V for 1 s using a 30 nm probe tip-to-sample separation. EFM micrographs were acquired by scanning at a lift height of 100 nm with -12 V applied to the probe tip.

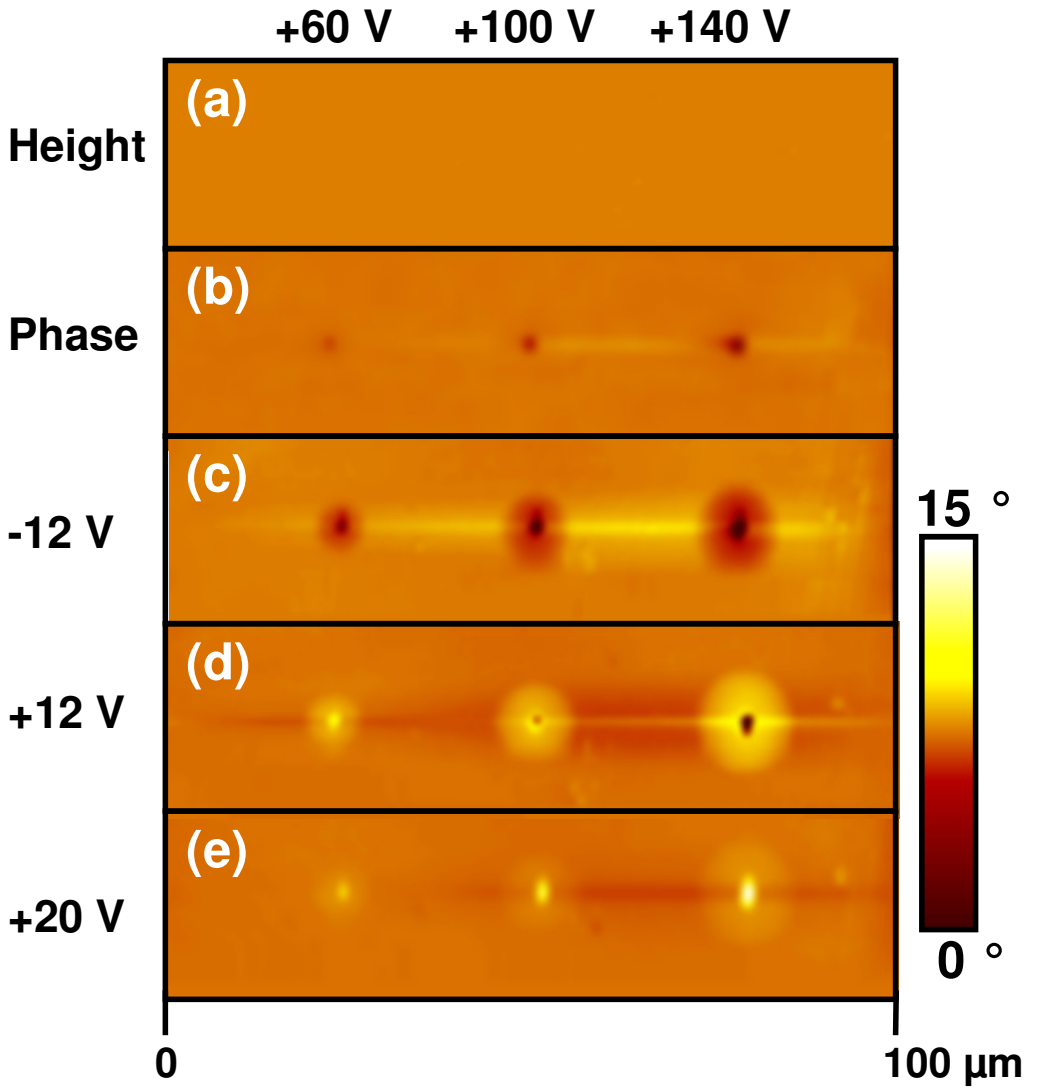

Figure 5.1.2: AFM micrographs of polystyrene taken immediately following the application of bias voltage (+60 V, +100 V, and +140 V) for 1 s using a probe tip-to-sample separation of 30 nm: (a) tapping mode height image, z scale = 100 nm; (b) tapping mode phase image, z scale = 15°; and (c) – (e) EFM micrographs obtained by scanning with a lift height of 100 nm where the voltage applied to the probe tip is: (c) -12 V; (d) +12 V; and (e) +20 V.

The systematic enlargement of observed surface charged regions with increasing applied voltage to the probe tip was verified by quantitative EFM analysis across a range of deposition voltages using a fixed probe tip-to-sample separation and duration, Figure 5.1.3. In order to minimise the effects of charge spreading and decay, the charging periods were restricted to 10 ms, and the EFM micrographs were acquired immediately afterwards at a scan speed of 3 Hz. A clear correlation is found between applied tip voltage and the resulting spot diameter of deposited charge.

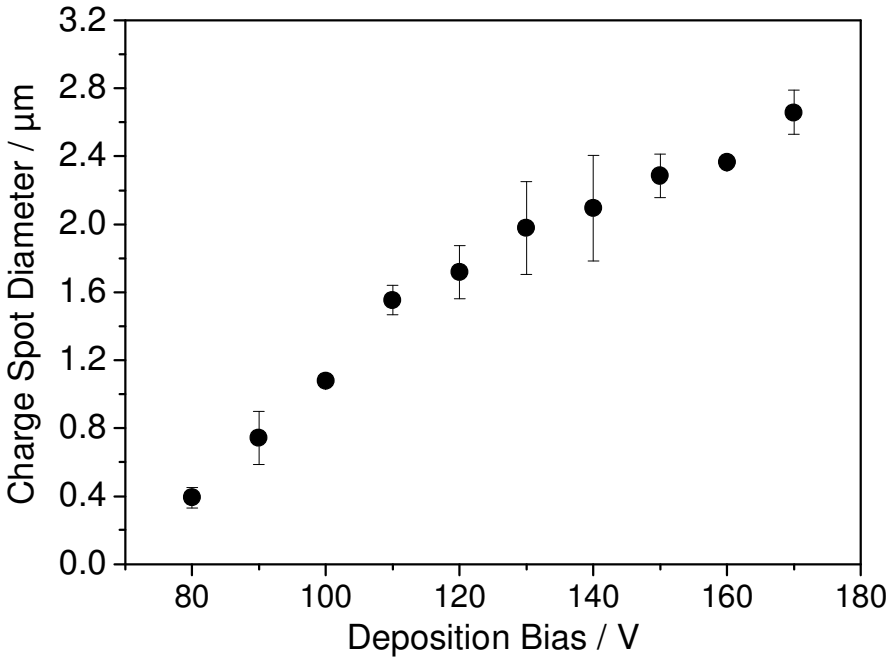

Figure 5.1.3: Deposited charge spot diameters measured from analysis of EFM micrographs for polystyrene (obtained by scanning 100 nm above the surface with +12 V applied to the probe tip) as a function of applied tip bias voltage using 30 nm tip-to-sample separation for 10 ms duration. Error bars correspond to one standard deviation.

Duration of surface charging was also found to be an important variable. Following 10 ms application of +100 V and +140 V bias voltage it can be seen that the charged region diameters (1.1 µm at +100 V and 2.1 µm at +140 V respectively) are significantly smaller in size compared to those measured for the longer 1 s deposition period under otherwise identical conditions, (9.0 µm at +100 V and 11.6 µm at +140 V respectively), Figures 5.1.2 and 5.1.3. Such dependency of charge spot size with deposition time was further exemplified by comparing longer periods of charging, Figure 5.1.4. It can be seen that the spreading of charge across the polymer surface exceeds the radius of the SPM probe tip (10 nm) by orders of magnitude.

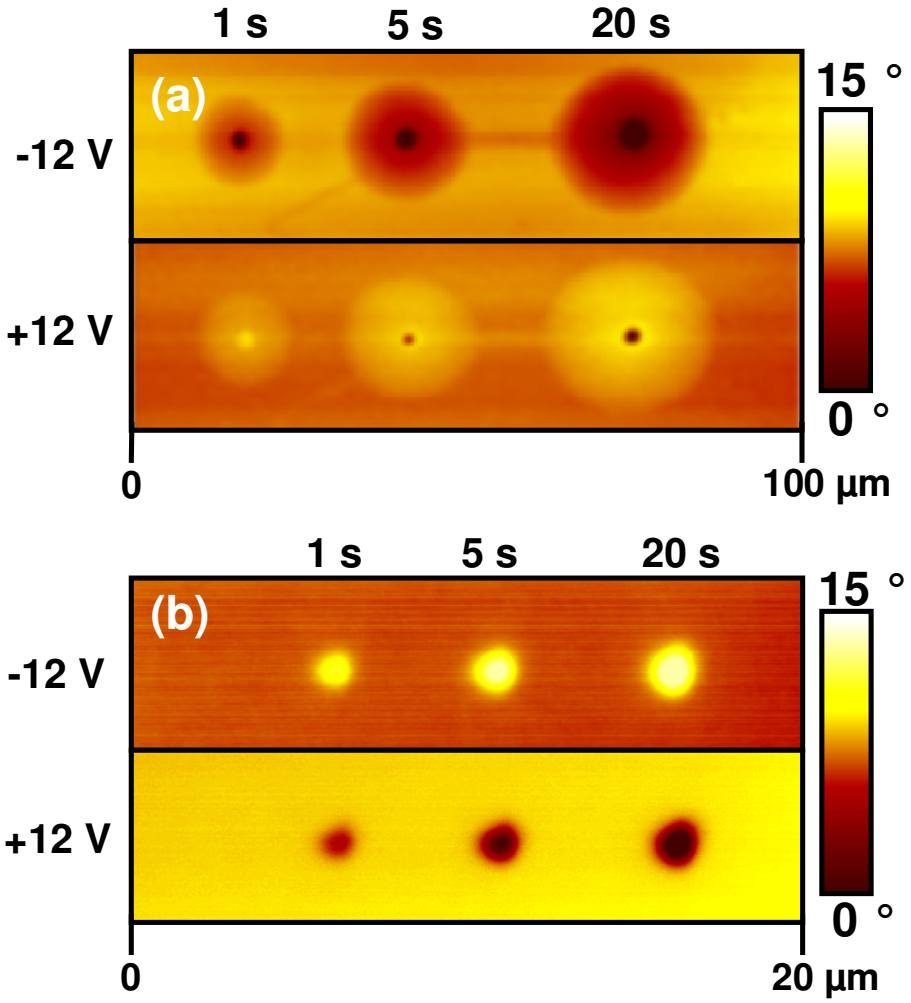

Figure 5.1.4: EFM micrographs of polystyrene following the application of (a) +100 V or (b) -140 V at a probe tip-to-sample separation of 30 nm for 1 s, 5 s, or 20 s duration. EFM micrographs were acquired by scanning at a lift height of 100 nm with either -12 V or +12 V applied to the probe tip.

In addition to charge deposition period and tip bias voltage magnitude, the charge spot sizes were also found to depend on the probe tip-to-sample separation, Figures 5.1.5 and 5.1.6. A strong correlation was observed between charge spot diameter and probe tip-to-sample separation.

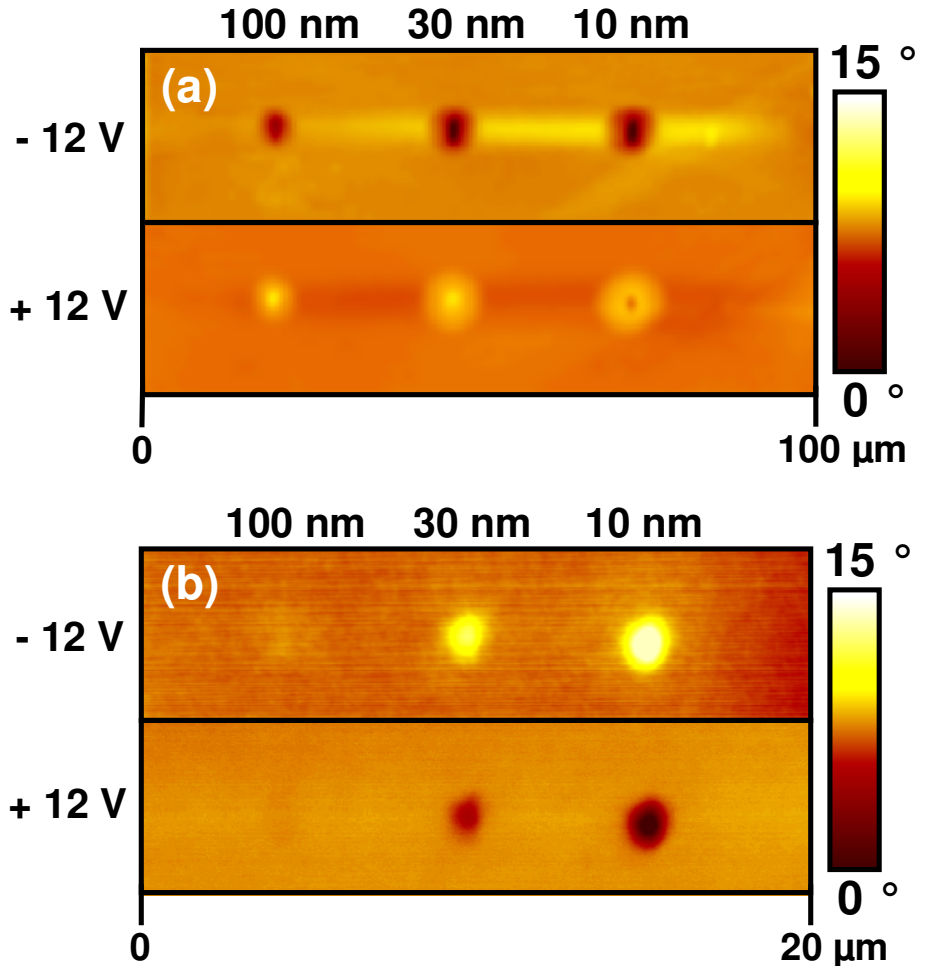

Figure 5.1.5: EFM micrographs of polystyrene following charge deposition using (a) +100 V and (b) -140 V tip bias voltage applied for 1 s at probe tip-to-sample separations of 100 nm, 30 nm, and 10 nm. EFM micrographs were acquired by scanning at a lift height of 100 nm with either -12 V or +12 V applied to the probe tip.

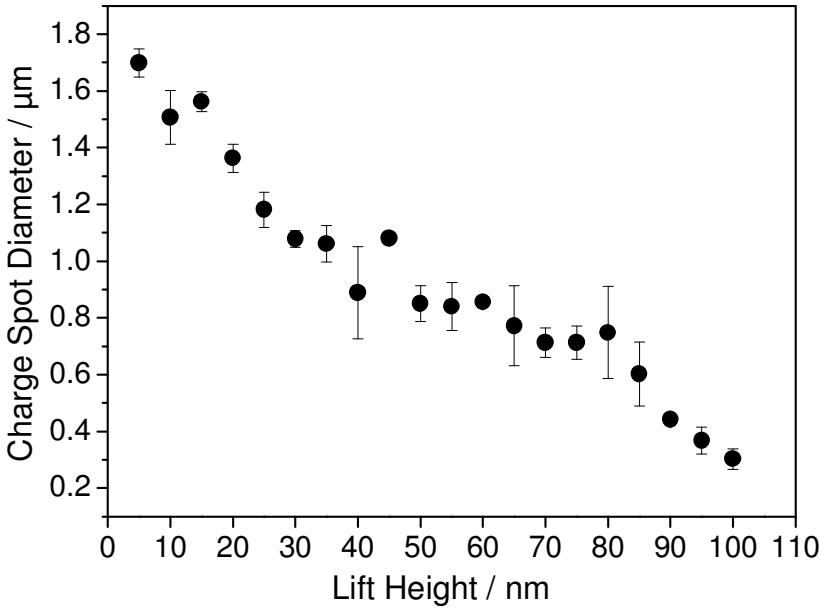

Figure 5.1.6: Charge spot diameters following the application of +100 V tip bias voltage for 10 ms, as a function of probe tip-to-sample separation for polystyrene. EFM micrographs were obtained by scanning at a lift height of 100 nm and +12 V applied to the probe tip (the effects of charge decay were minimised using a detection scan speed of 3 Hz following charge deposition). Error bars correspond to one standard deviation.

Corresponding experiments undertaken for negative charge deposition onto polystyrene surfaces also displayed featureless height and phase AFM images. Notable differences in the case of negative charging include consistently smaller regions of detected surface charge and a more uniform decay of charge across the whole spot, Figures 5.1.1 and 5.1.7. The relative charged region diameters increased with deposition bias voltage, charging duration and decreasing probe tip-to-sample separation (as previously observed for the positive charge deposition experiments), Figures 5.1.4, 5.1.5, and 5.1.7.

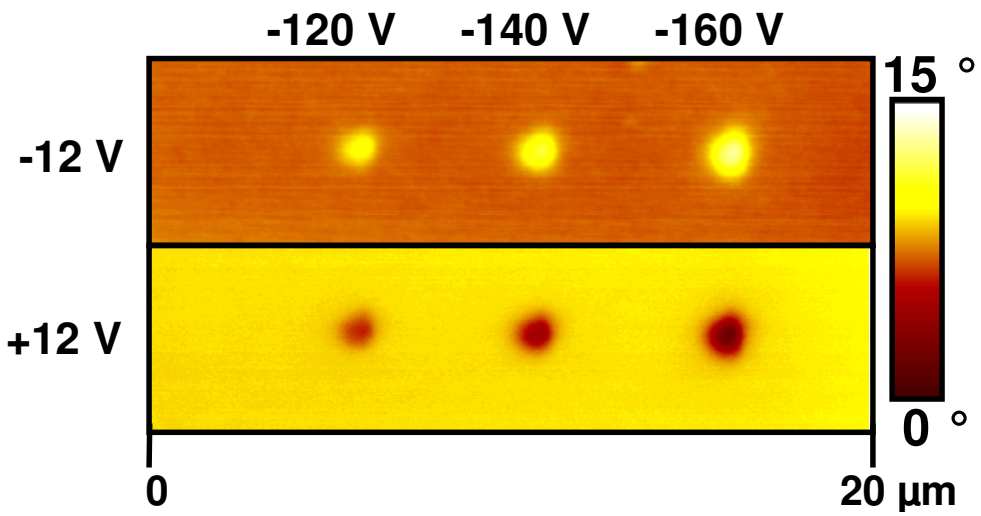

Figure 5.1.7: EFM micrographs of polystyrene following charge deposition for 1 s with a probe tip-to-sample separation of 30 nm and applied tip bias of -120 V, -140 V, and -160 V. EFM micrographs were acquired by scanning at a lift height of 100 nm with either -12 V or +12 V applied to the probe tip.

5.1.3.2 Polymer Surface Charging Thresholds

It was noted that a distinct threshold bias voltage applied to the SPM probe tip was necessary to elicit surface charging. This minimum voltage required for surface charging was determined for a variety of different polymers by raising bias voltage application to the probe tip in increments of 5 V (1 s duration held at a height of 30 nm above the surface) until a response was observed by EFM imaging, Table 5.1.1 and Figure 5.1.8. The measured positive and negative charging thresholds were found to correlate to each other.

Table 5.1.1: Negative and positive applied voltage SPM probe tip charging thresholds and water contact angles for polymers. Voltage was applied to the probe tip for 1 s with a tip-to-sample separation of 30 nm. Thresholds were measured by raising the applied bias voltage to the probe tip in increments of 5 V until a response was detectable in the EFM micrographs using a lift height of 100 nm with ±12 V applied to the probe tip (except in the case of polyvinylidene fluoride where a detection bias of just ±1 V was sufficient, due to the polymer's inherent high affinity towards charging[40]). †For more hydrophilic polymers such as polyhydroxyethylmethacrylate, polyvinylalcohol and polyethyleneoxide, no surface charging could be achieved, even following application of the highest voltages permittable by the apparatus (±180 V) (error values are one standard deviation).

Polymer	***Charging Threshold*** *(V)*		***Water Contact Angle*** *(°)*
	Positive	***Negative***	
Polyvinylidene fluoride	10	10	115 ± 1
Polymethoxystyrene	30	50	88 ± 1
Polychlorostyrene	30	60	88 ± 1
Polystyrene	25	70	92 ± 1
Polymethylstyrene	35	75	95 ± 1
Polyisopropylstyrene	45	80	100 ± 1
Polyvinylchloride	30	90	86 ± 1
Polytertbutylstyrene	35	95	103 ± 1
Polymethylmethacrylate	50	125	69 ± 1
Nylon 6-6	70	160	67 ± 1
Polyhydroxyethylmethacrylate	†	†	58 ± 1
Polyvinylalcohol	†	†	48 ± 1
Polyethyleneoxide	†	†	27 ± 1

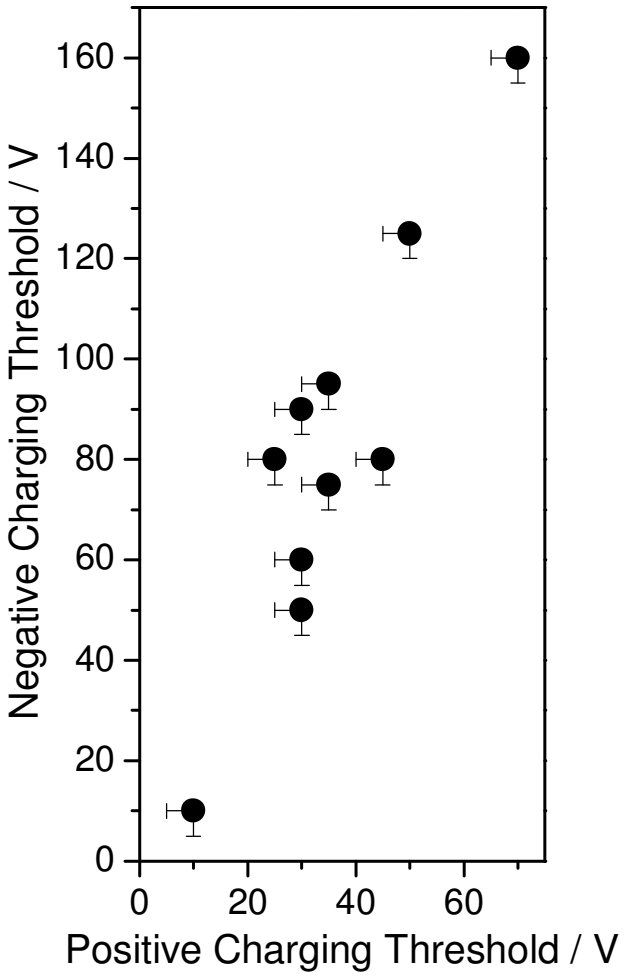

Figure 5.1.8: Applied voltage thresholds to the SPM probe tip for negative charge deposition onto a variety of polymer surfaces as a function of their positive charging thresholds (taken from Table 5.1.1).

Furthermore, it was noted that surface charging thresholds were found to be much greater for more hydrophilic polymers, Figure 5.1.9. No surface charging could be achieved for the more hydrophilic polymers (polyhydroxyethylmethacrylate (contact angle 58°), polyvinylalcohol (contact angle 48°), and polyethyleneoxide (contact angle 27°)), despite applying the highest probe tip voltages permittable by the apparatus (±180 V).

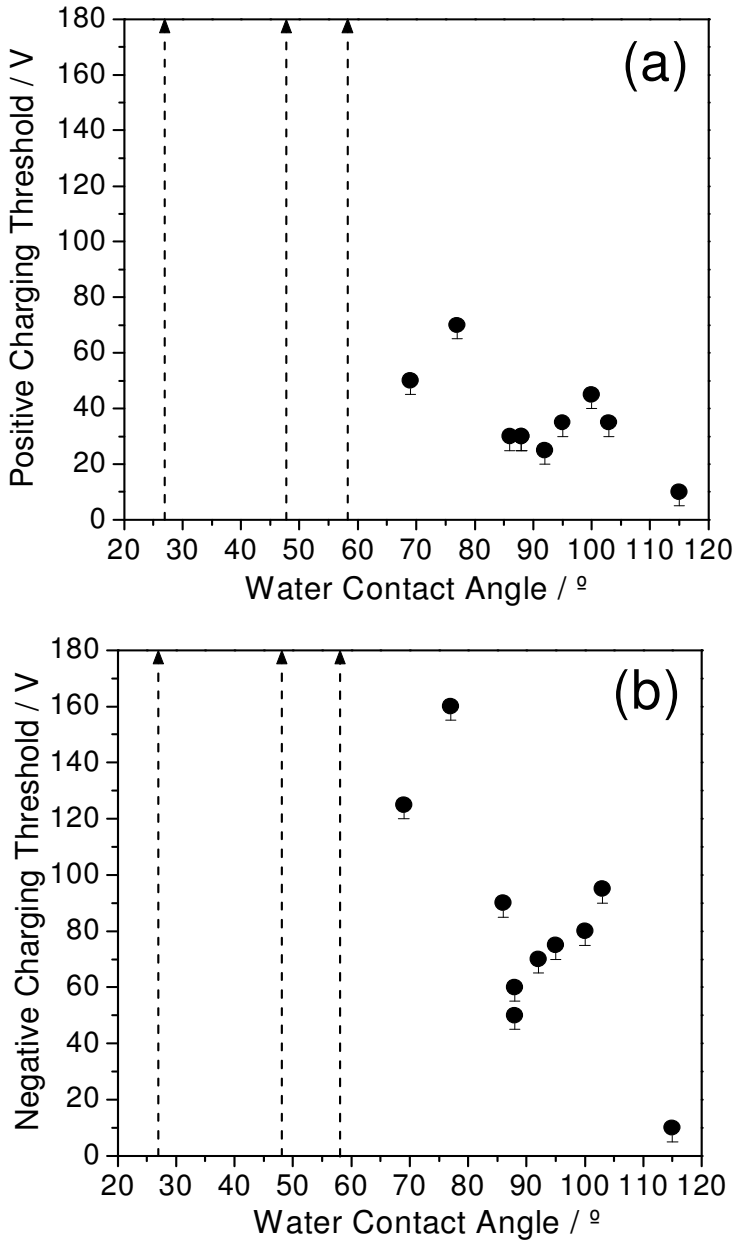

Figure 5.1.9: Applied bias voltage threshold for SPM probe tip surface charging of polymers as a function of static water contact angle: (a) positive charging; and (b) negative charging. For more hydrophilic polymers such as polyhydroxyethylmethacrylate (contact angle 58°), polyvinylalcohol (contact angle 48°) and polyethyleneoxide (contact angle 27°) no surface charging could be achieved (illustrated by dashed arrow lines), even following application of the highest voltages permittable by the apparatus (±180 V).

5.1.4 DISCUSSION

Potentially, three possible mechanisms can be envisaged for the deposition of charge onto insulator surfaces using a biased SPM probe tip. These are dielectric breakdown of the substrate,[28] contact electrification,[9,10,11,12] and corona discharge.[17,18,19] The featureless topography of the polymer surfaces observed by tapping mode AFM following charge deposition at even the highest applied probe tip bias voltages eliminates dielectric breakdown of the substrate, due to the absence of any evidence for heating or surface deformation features,[41,42] Figure 5.1.2. The measured correlation between charge spot size and probe tip-to-sample separation effectively eliminates contact electrification mechanisms (whether via direct contact with the substrate or by way of a water meniscus) because no charging would be expected to occur beyond a threshold probe tip-to-sample separation (lift height).[43,44,45] Therefore, the experimental observations are consistent with a corona discharge mechanism.

Surface charging of polymers using the present technique may be understood by further consideration of the corona discharge mechanism. During point-to-plane corona discharge formation in air, a localised plasma region develops around the sharp point, where the ions generated can drift across the applied electric field towards the lower planar counter electrode,[46,47,48] Table 5.1.2. In the case of SPM charging, these ions are created near the probe tip apex and impinge upon the polymer layer as they drift towards the underlying counter electrode (metal sample disc holder), to give rise to a line-of-sight localised build up of surface charge, Scheme 5.1.1.

Table 5.1.2: Examples of ions contained within positive and negative corona discharges at atmospheric pressure and humidity (in order of decreasing abundance).[46,47]

Positive Corona Discharge	***Negative Corona Discharge***
$(H_2O)_nH^+$	CO_3^-
$(NO^+)(H_2O)_n$	$CO_3(H_2O)^-$
$(NO_2^+)(H_2O)_n$	O_3^-
$O_2^+(H_2O)_n$	NO_2^-
HO_2^+	O^-
NH_3^+	

Negative charge deposition onto the range of polymer surfaces studied was consistently found to be less efficient than positive charging, as evident from the higher deposition bias voltages required to elicit an EFM phase signal response and the smaller size charged spots observed, Table 5.1.1 and Figure 5.1.1. This is consistent with previous work, where it is known that for corona discharge generation at a sharp point, positive coronas discharges readily form high velocity streamers directly in front of the needle.[49,50] The secondary electrons necessary to maintain the positive corona are formed outside of the plasma region and are attracted back towards the point electrode, while positive ions are concurrently being repelled away. This leads to the formation of streamers during the rapid expansion of the ionisation region surrounding the point electrode, to culminate in arcing across the gap. In the case of negative corona discharge, streamer formation can be inhibited due to a different mechanism being in operation. This is where, in contrast, secondary electrons are produced at the point electrode by the photoelectric effect, and they then quickly attach to electronegative molecules to form a slow moving negative ion cloud.[51] Such an ion cloud reduces the effective electric field at the negatively biased point electrode to below the air breakdown threshold, and thus halts the discharge. The discharge then reignites once the negative ion cloud drifts sufficiently far away from the tip such that the electric field at the probe apex is restored to above the gas

breakdown threshold.[51] As a consequence, negative corona discharges frequently operate via rapid 'Trichel' pulses, and ions possess less kinetic energy compared to those present in positive corona discharges under comparable conditions.[49] This provides a viable explanation for why surface charging occurs less readily in the case of negative voltage SPM probe tip corona discharges.

The correlation observed between positive and negative charging thresholds for a range of different polymers indicates that surface charging thresholds are not governed by the presence of charge trap sites (which are specifically unique to either positive or negative poling),[52,53,54] Table 5.1.1 and Figure 5.1.1. Rather, the measured thresholds are more likely to be attributable to relative charge dissipation rates, and previous studies involving contact mode SPM charge injection onto polymer surfaces have consistently shown that greater water adsorption at higher relative humidity enhances the spreading and dissipation of charge in insulators, due to improved surface conductance.[55] Spreading of charge with increasing period of charging was indeed observed in the present non-contact mode SPM charge deposition study. For instance in the case of polystyrene, surface charging indicates that some mobility of charge even occurs across this relatively hydrophobic polymer (contact angle 92 ± 1°). Furthermore, the charging thresholds measured are found to display correlation to polymer surface wettability, Figure 5.1.9. Therefore, one plausible explanation might be that surface charge retention is in fact limited by rapid charge dissipation, which in turn is governed by the level of water adsorption from the ambient.

Finally, further improvements in feature size and charge dissipation can be envisaged by selecting sharper SPM probe tips and choosing suitably hydrophobic polymer substrates in order to inhibit surface charge spreading mechanisms.

5.1.5 CONCLUSIONS

Spatially localised surface electrification and detection has been accomplished by using an SPM probe tip to firstly create a corona discharge, and then to observe the deposited surface charge. The feature resolution of surface charge patterning is found to be governed by tip-to-substrate separation, period of charging, threshold voltage, and polymer wettability.

5.1.6 REFERENCES

(1) Barrett, R. C.; Quate, C. F. *J. Appl. Phys.* **1991**, *70*, 2725.

(2) Stark, R. W.; Naujoks, N.; Stemmer, A. *Nanotechnology* **2007**, *18*, 065502.

(3) McCarty, L. S.; Winkleman, A.; Whitesides, G. M. *J. Am. Chem. Soc.* **2007**, *129*, 4075.

(4) Naujoks, N.; Stemmer, A. *Microelectron. Eng.* **2005**, *78*, 331.

(5) Seemann, L.; Stemmer, A.; Naujoks, N. *Nano Lett.* **2007**, *7,* 3007.

(6) Saito, N.; Maeda, N.; Sugimura, H.; Takai, O. *Langmuir* **2004**, *20,* 5182.

(7) Brogueira, P.; Melo, L. V. *Mater. Sci. Eng. C* **2003**, *23*, 1103.

(8) Wright, W. M. D.; Chetwynd, D. G. *Nanotechnology* **1998**, *9*, 133.

(9) Blanco, E. M.; Nesbitt, S. A.; Horton, M. A.; Mesquida, P. *Adv. Mater.* **2007**, *19,* 2469.

(10) Zdrojek, M.; Mélin, T.; Diesinger, H.; Stiévenard, D.; Gebicki W.; Adamowicz, L. *J. Appl. Phys.* **2006**, *100*, 114326.

(11) Diesinger, H.; Mélin, T.; Deresmes, D.; Stiévenard, D.; Baron, T. *Appl. Phys. Lett*. **2004**, *85*, 3546.

(12) Jiao, Z.; Wan, X.; Guo, H.; Wang, J.; Zhao, B.; Wu, M. *Ultramicroscopy* **2008**, *108*, 1371.

(13) Knorr, N.; Rosselli, S.; Miteva, T.; Nelles, G. *J. Appl. Phys.* **2009**, *105*, 114111.

(14) Saurenbach, F.; Terris, B. D. *IEEE Trans. Ind. Appl.* **1992**, *28*, 256.

(15) Marchi, F.; Dianoux , R.; Smilde, H. J. H.; Mur, P.; Comin, F.; Chevrier, J. *J. Electrostat.* **2008**, *66*, 538.

(16) Stevens, G. C.; Baird, P. J. *IEEE Trans. Dielectr. Electr. Insul.* **2005**, *12*, 979.

(17) Stern, J. E.; Terris, B. D.; Mamin, H. J.; Rugar, D. *Appl. Phys. Lett.* **1988**, *53,* 2717.

(18) Schönenberger, C. *Phys. Rev. B* **1992**, *45*, 3861.

(19) Schönenberger, C.; Alvarado, S. F. *Phys. Rev. Lett.* **1990**, *65*, 3162.

(20) Tipler, P. A. *College Physics*, Worth: New York, 1987; pp467.

(21) Rigden, J. S. *Macmillan Encyclopedia of Physics*, Simon & Shushter

Macmillan: New York, 1996; pp353.

(22) Capella, B.; Dietler, G. *Surf. Sci. Rep.* **1999**, *34*, 1.

(23) Yang, C.-W.; Hwang, I.-S.; Chen, Y. F.; Chang, C. S.; Tsai, D. P. *Nanotechnology* **2007**, *18*, 084009.

(24) Martin, Y.; Williams C. C.; Wickramasinghe, H. K. *J. Appl. Phys.* **1987**, *61*, 4723.

(25) Zavala, G. *Colloid Polym. Sci.* **2008**, *286*, 85.

(26) García, R.; Pérez, R. *Surf. Sci. Rep*. **2002**, *47*, 197.

(27) Chiang, D.-M.; Liu, W.-L.; Chen J.-L.; Susuki, R. *Chem. Phys. Lett*. **2005**, *412*, 50.

(28) Qiu, X. H.; Qi, G. C.; Yang, Y. L.; Wang, C. *J. Solid State Chem.* **2008**, *181*, 1670.

(29) Riedel, C.; Arinero, R,; Tordjeman, Ph.; Ramonda, M.; Lévêque, G.; Schwartz, G. A.; de Oteyza, D. G.; Alegria, A.; Colmenero, J. *J. Appl. Phys.* **2009**, *106*, 024315.

(30) Cherniavskaya, O.; Chen, L.; Islam, M. A.; Brus, L. *Nano Lett.* **2003**, *3*, 497.

(31) Patrício, P. S. O.; Cury, L. A.; Silva, G. G.; Neves, B. R. A. *Ultramicroscopy* **2008**, *108*, 302.

(32) Takano, H.; Wong, S.-S.; Harnisch, J. A.; Porter, M. D. *Langmuir* **2000**, *16*, 5231.

(33) Jiang, J.; Krauss, T. D.; Brus, L. E. *J. Phys. Chem. B* **2000**, *104*, 11936.

(34) Krayev, A. V.; Talroze, R. V. *Polymer* **2004**, *45*, 8195.

(35) Jespersen, T. S.; Nygård J. *Appl. Phys. Lett*. **2007**, *90*, 183108.

(36) Belaidi, S.; Girard, P.; Leveque, G. *J. Appl. Phys.* **1997**, *81*, 1023.

(37) Lei, C. H.; Das, A.; Elliott, M.; Macdonald, J. E. *Appl. Phys. Lett.* **2003**, *83*, 482.

(38) Hölscher, H.; Schwarz, U. D. *Int. J. Non-Linear Mech.* **2007**, *42*, 608.

(39) Ebbens, S. J.; Badyal, J. P. S. *Langmuir* **2001**, *17*, 4050.

(40) Fedosov, S. N.; Sergeeva, A. E. *J. Electrostat.* **1993**, *30*, 327.

(41) Reagan, M. A.; Kashyn, D.; Juhl, S.; Vaia, R. A.; Lyuksyutov, S. F. *Appl. Phys. Lett.* **2008**, *93*, 033109.

(42) Lyuksyutov, S. F.; Vaia, R. A.; Paramonov, P. B.; Juhl, S.; Waterhouse, L.; Ralich, R. M.; Sigalov, G.; Sancaktar, E. *Nat. Mater.* **2003**, *2*, 468.

(43) Gómez-Moñivas, S.; Sáenz, J. J.; Calleja, M.; García, R. *Phys. Rev. Lett.* **2003**, *91*, 056101.

(44) García, R.; Calleja, M.; Rohrer, H. *J. Appl. Phys.* **1999**, *86*, 1898.

(45) Sacha, G. M.; Verdaguer, A.; Salmeron, M. *J. Phys. Chem. B* **2006**, *110,* 14870.

(46) Shahin, M. M. *Appl. Opt.* **1969**, *8*, 106.

(47) Shahin, M. M. *J. Chem. Phys*. **1966**, *45*, 2600.

(48) Goldman, M.; Goldman, A.; Sigmond, R. S. *Pure Appl. Chem.* **1985**, *57*, 1353.

(49) Lowke, J. J.; Morrow, R. *Pure Appl. Chem.* **1994**, *66*, 1287.

(50) Moreau, E.; Touchard, G. *J. Electrostat.* **2008**, *66*, 39.

(51) Sattari, P.; Gallo, C. F.; Castle, G. S. P.; Adamiak, K. *J. Phys. D: Appl. Phys.* **2011**, *44*, 155502.

(52) Bamji, S. S. *J. Phys. D: Appl. Phys.* **1982**, 15, 911.

(53) Migahed, M. D.; Shaban, A. M.; El-Khodary, A.; Hafiz, H. R. *Polym. Bull.* **1990**, *23*, 61.

(54) Mishra, A. *J. Appl. Polym. Sci.* **1982**, *27*, 1107.

(55) Zaghloul, U.; Bhushan, B.; Pons, P.; Papaioannou, G. J.; Coccetti, F.; Plana, R. *Nanotechnoogy* **2011**, *22*, 035705.

CHAPTER 5

PART 2: NANOPLASMA INDUCED SWELLING AND COLLAPSE OF SURFACE TETHERED POLYMER BRUSHES

5.2.1 INTRODUCTION

'Smart' stimuli-responsive surfaces are of importance for the development of responsive membranes,[1] bioactive surfaces,[2] drug delivery vehicles,[3] molecular motors,[4] and colloidal stabilisers.[5] Within this field, polyelectrolytes comprise a promising class of material which can be swollen or collapsed in response to environmental changes in pH,[6] ionic strength,[7] humidity,[8,9] and electric fields.[10] Furthermore, controlled surface grafting of densely crowded polyelectrolyte brushes has been realised using atom transfer radical polymerization (ATRP).[11,12,13]

Polyelectrolyte brushes may be sub-categorised according to the mode of pendant group disassociation, which dictates the stimulation used to induce swelling and collapse (i.e., variation of pH or ionic strength). Firstly, 'weak' polyelectrolyte brushes are composed of acidic or basic repeat units which dissociate to a degree dependent on the pH of their environment. Pendant group dissociation corresponds to increased intramolecular electrostatic repulsion along polymer chains, and hence an increase in the effective brush length.[14] In contrast, the ionic groups comprising 'strong' polyelectrolyte brushes completely dissociate in an aqueous environment, so that the osmotic pressure provided by condensed counter-ions within the brush layer yields stretched chains.[15] Such brushes are insensitive to pH, but as the ionic strength of the medium is increased, the osmotic pressure within the brush layer is counter-balanced, resulting in layer shrinkage. One alternative stimulus reported for polyelectrolyte swelling is humidity, whereby the brush response is underpinned by the predominately hygroscopic nature of polyelectrolytes.[16,17,18] In this case, increased water uptake from the environment occurs in response to raised humidity, and yields polymer swelling.[19,20] Finally, hydrogels composed of strong polyelectrolytes have been shown to bend in electrolyte under the influence of an electric field, due to the migration of counter-ions.[10,21,22]

For all of the aforementioned techniques, widespread applicability is limited by the nature of the stimulus. Variation of environmental pH or ionic strength requires immersion in solution,[23] and this is also a prerequisite to facilitate the migration of counter-ions under an electric field,[21,22] whereas

variation of environmental humidity is unwieldy. Furthermore, these approaches are only capable of producing a response over the entirety of a brush layer, and cannot readily be localised for application such as fluidics or nanomachines.

Weir *et al* recently reported a novel methodology to induce swelling for weak polybasic brushes grafted onto silicon, where the application of an electric field between the underlying silicon and a distant counter electrode induced enhanced polymer brush swelling (in comparison to using pH as stimulus), as a consequence of electrostatic repulsion between the positively biased substrate and polymer brush segments.[24] Furthermore, simulations confirm that polyelectrolyte brushes are expected to respond to electric fields in this manner.[25,26] Nonetheless, limitations of this technique include the use of an aqueous environment, and a lack of lateral control due to the macroscopic methodology.

Scanning probe microscope (SPM) techniques have routinely been used to apply highly localised electric fields to polymer thin films and write charge onto dielectric layers.[27,28,29] Non-contact surface charging using an SPM probe has been demonstrated to yield localised charge retention or polymer thin film deformation as a result of the dielectric breakdown of air or water between the probe tip and substrate.[28,30,31,32,33] Whilst localised charging in this manner has repeatedly been reported for neutral polymers (as in Chapter 5 Part 1), the only previous report of an attempt to apply such a technique to polyelectrolyte involved contact mode SPM probe charge injection into spin-coated poly(sodium 4-styrenesulfonate).[34] This resulted in the formation of a three-dimensional Lichtenberg discharge figure (i.e., a topographical change).

The purpose of the present study is to investigate the response of strong polyelectrolyte brushes (anionic poly(sodium 4-styrenesulfonate), cationic poly((2-methacryloyloxy)ethyl trimethyl ammonium chloride)) and zwitterionic poly(*N,N*-dimethyl-*N*-(3-methacrylamido)-*N*-(3-sulfopropyl) ammonium betaine) brushes) to non-contact SPM charging. Polyelectrolyte brush layers are grafted by ATRP onto pulsed plasma deposited poly(vinylbenzyl chloride) layers, Scheme 5.2.1. These are then exposed to

corona discharge by the application of potential to an SPM probe held in close proximity to the layers.

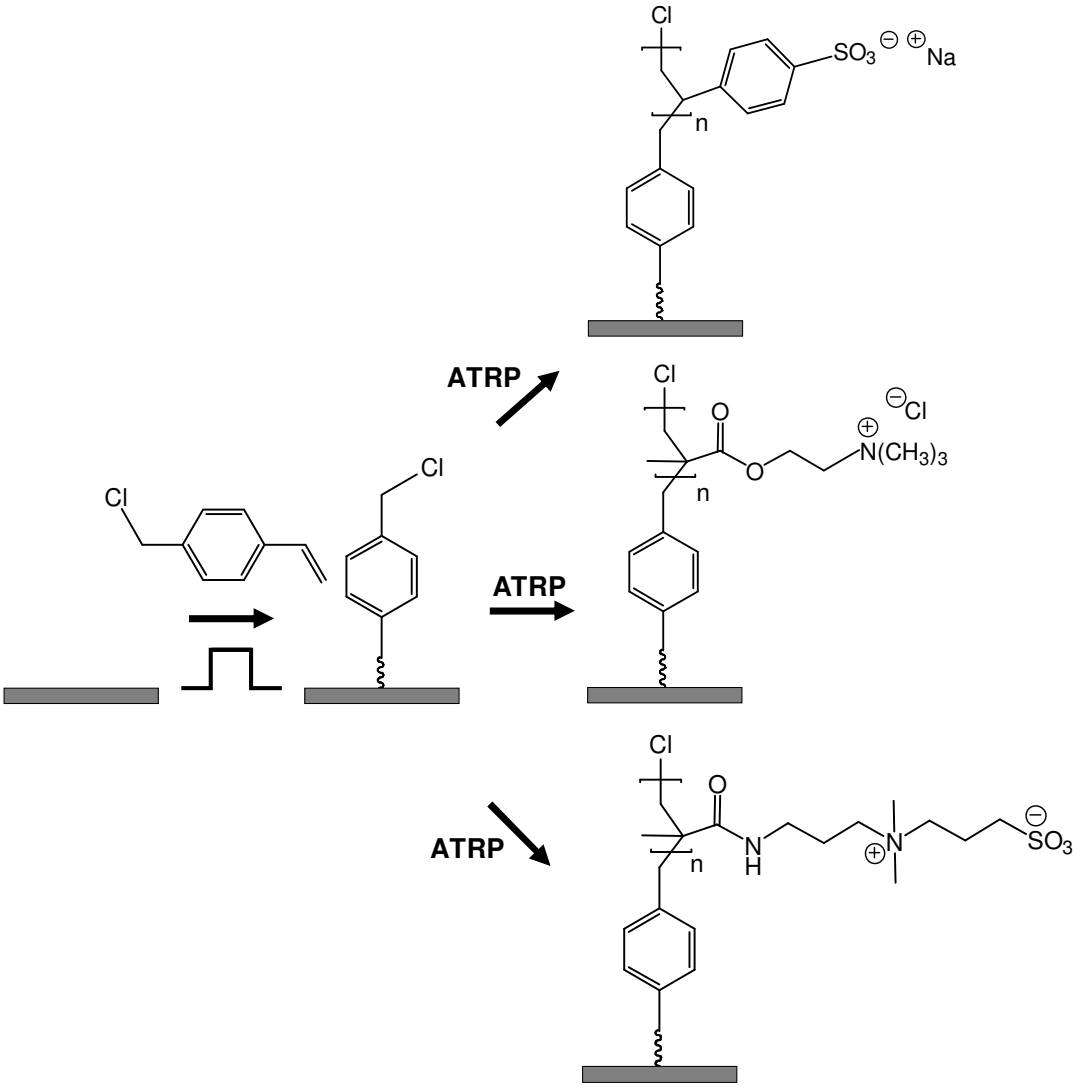

Scheme 5.2.1: ATRP grafting of anionic poly(sodium 4-styrenesulfonate) polyelectrolyte brushes, cationic poly((2-methacryloyloxy)ethyl trimethyl ammonium chloride) polyelectrolyte brushes and zwitterionic poly(*N,N*-dimethyl-*N*-(3-methacrylamido)-*N*-(3-sulfopropyl) ammonium betaine) brushes onto pulsed plasma deposited poly(vinylbenzyl chloride) ATRP initiator layers.

5.2.2 EXPERIMENTAL

5.2.2.1 Pulsed Plasmachemical Deposition

Plasma deposition of poly(vinylbenzyl chloride) ATRP initiator layers were performed as described in Chapter 2, Section 2.2.1.

5.2.2.2 Surface Initiated ATRP

The solvent and catalyst systems used for ATRP are given in Table 5.2.1. The ATRP grafting protocol comprised removal of trapped gases from solutions consisting of 5 mmol monomer and 4 mL solvent, using a minimum of four freeze-pump-thaw cycles. The catalyst system was then added to the solution whilst it was frozen, together with pulsed plasma functionalised initiator samples, followed by evacuation of the sealed vessel. Reaction vessels were subsequently immersed into an oil bath set to 50 °C for a predetermined grafting time. Upon removal, substrates were thoroughly rinsed in high purity water to remove any physisorbed polymer and allowed to dry in air.

Table 5.2.1: ATRP conditions for grafting onto pulsed plasma poly(vinylbenzyl chloride) functionalised samples.

Monomer	***CuBr : $CuBr_2$: bpy*** *(mmol)*	***Solvent***
Sodium 4-styrenesulfonate (+90 %, Aldrich)	0.05 : 0.04 : 0.18	H_2O
(2-methylacryloyloxy)ethyl trimethyl ammonium chloride (80 wt % solution, Aldrich)	0.05 : 0.01 : 0.12	3 : 1 H_2O : MeOH
N,N-dimethyl-*N*-(3-methacrylamido)-*N*-(3-sulfopropyl) ammonium betaine (+97 %, Aldrich)	0.05 : 0.01 : 0.12	3 : 1 H_2O : MeOH

5.2.2.3 Nanolayer Characterisation

Film thicknesses and infrared spectra were obtained as described in Chapter 2, Section 2.2.3.

5.2.2.4 Corona Discharge Exposure and Electric Force Microscopy

Exposure of polymer coated silicon wafer pieces to SPM corona discharge was achieved using an identical experimental set-up as described in Chapter 5.1, Section 5.1.2.2, where a bias voltage of ±150 V was applied for 1 s between the probe and underlying electrode (sample holder) with a tip-to-surface separation of 30 nm.

Atomic force microscopy and electric force microscopy images were acquired as described in Chapter 5.1, Section 5.1.2.3.

5.2.3 RESULTS

5.2.3.1 Surface Initiated ATRP

XPS analysis of the pulsed plasma deposited poly(vinylbenzyl chloride) ATRP initiator layers yielded elemental compositions and infrared spectroscopy fingerprint features identical to those reported in Chapter 2, thereby indicating good structural retention of the benzyl chloride functionality. Infrared spectroscopy of the ATRP grafted polymer brush layers exhibited spectral fingerprint regions closely resembling those measured for the respective monomers, Figure 5.2.1. Characteristic features identified for poly(sodium 4-styrenesulfonate) brushes include a set of strong absorbances at 1136 cm^{-1}, 1181 cm^{-1} and 1231 cm^{-1} (antisymmetric SO_2 stretches), and 1048 cm^{-1} (symmetric SO_2 stretch).[35] For ATRP grafted poly((2-methylacryloyloxy)ethyl trimethyl ammonium chloride) layers key infrared absorbances for both the monomer and brush layers include 1722 cm^{-1} (C=O ester stretch), 1172 cm^{-1}, (C-O ester stretch), 1456 cm^{-1} and 1479 cm^{-1} (quaternary amine CH_3 asymmetric bending). In the case of ATRP grafted poly(*N,N*-dimethyl-*N*-(3-methacrylamido)-*N*-(3-sulfopropyl) ammonium betaine) layers, there were peaks at 1654 cm^{-1} (C=O ester stretch), 1536 cm^{-1} and 1488 cm^{-1} (amine $(CH_3)_2$ bending doublet), 1171 cm^{-1} (antisymmetric SO_2 stretch), and 1041 cm^{-1} (symmetric SO_2 stretch).[35] For all of these grafted layers, there was the absence of the vinyl C=C stretch absorbance following ATRP (at 1655 cm^{-1}, 1633 cm^{-1} and 1606 cm^{-1} for poly(sodium 4-styrenesulfonate), poly((2-methylacryloyloxy)ethyl trimethyl ammonium chloride), and poly(*N,N*-dimethyl-*N*-(3-methacrylamido)-*N*-(3-sulfopropyl) ammonium betaine) respectively[35]).

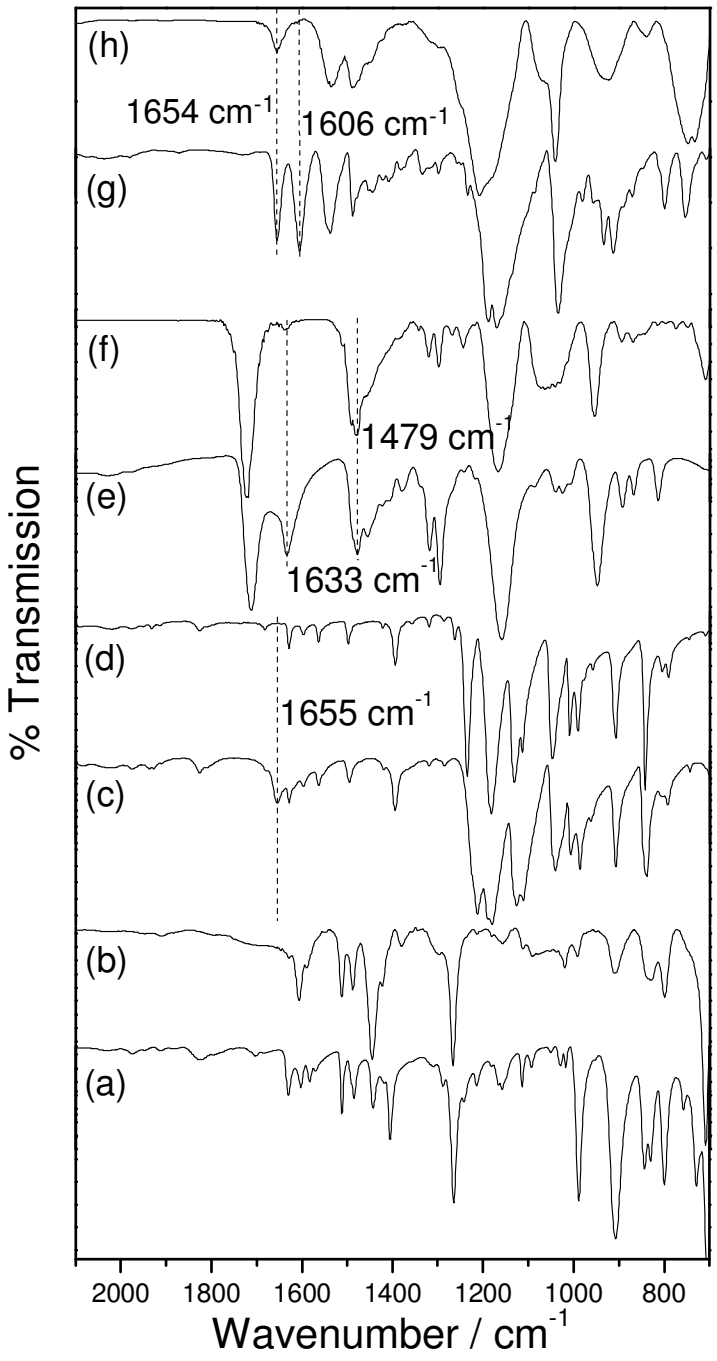

Figure 5.2.1: Infrared spectra of: (a) the vinylbenzyl chloride monomer; (b) pulsed plasma deposited poly(vinylbenzyl chloride); (c) sodium 4-styrenesulfonate monomer; (d) ATRP grafted poly(sodium 4-styrenesulfonate) grown onto pulsed plasma deposited poly(vinylbenzyl chloride); (e) (2-methylacryloyloxy)ethyl trimethyl ammonium chloride monomer; (f) ATRP grafted poly((2-methylacryloyloxy)ethyl trimethyl ammonium chloride) grown onto pulsed plasma deposited poly(vinylbenzyl chloride); (g) *N,N*-dimethyl-*N*-(3-methacrylamido)-*N*-(3-sulfopropyl) ammonium betaine monomer and (h) poly(*N,N*-dimethyl-*N*-(3-methacrylamido)-*N*-(3-sulfopropyl) ammonium betaine) brushes grown onto pulsed plasma deposited poly(vinylbenzyl chloride).

The controlled nature of surface ATRP was confirmed by monitoring the dry polymer brush film thickness versus grafting time, Figure 5.2.2. A linear increase was observed for each system, yielding corresponding growth rates of 31 ± 2 nm h^{-1}, 15 ± 3 nm h^{-1}, and 5 ± 1 nm h^{-1} for poly(sodium 4-styrenesulfonate), poly((2-methylacryloyloxy)ethyl trimethyl ammonium chloride), and poly(*N,N*-dimethyl-*N*-(3-methacrylamido)-*N*-(3-sulfopropyl) ammonium betaine) respectively. For prolonged grafting periods a loss of control was evident for the polyelectrolyte brushes (at 1.5 h and 3 h for poly(sodium 4-styrenesulfonate), and poly((2-methylacryloyloxy)ethyl trimethyl ammonium chloride) respectively), which is attributable to the oxidative breakdown of catalytic species in the aqueous phase.[36]

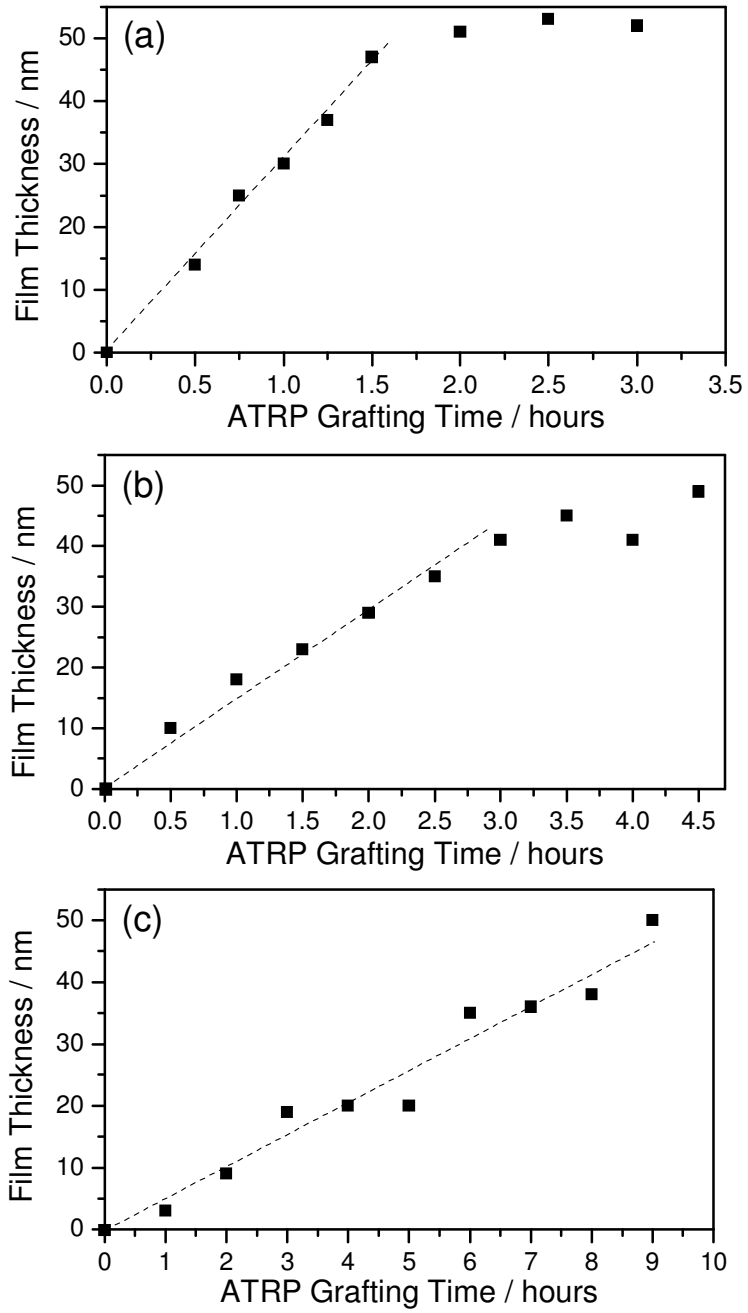

Figure 5.2.2: Variation of polymer brush film thickness grown onto pulsed plasma deposited poly(vinylbenzyl chloride) ATRP initiator layer as a function of ATRP grafting period for: (a) anionic poly(sodium 4-styrenesulfonate) brushes; (b) cationic poly((2-methylacryloyloxy)ethyl trimethyl ammonium chloride) brushes and (c) zwitterionic poly(*N,N*-dimethyl-*N*-(3-methacrylamido)-*N*-(3-sulfopropyl) ammonium betaine) brushes.

5.2.3.2 SPM Corona Discharge onto Polyelectrolyte Brush Layers

SPM corona discharge onto surface tethered polyelectrolyte brushes was investigated by application of ±150 V to the SPM probe tip for 1 s using a probe tip-to-sample separation of 30 nm. Featureless EFM micrographs (acquired immediately after this bias voltage application), confirmed the absence of any charge retention by the anionic poly(sodium 4-styrenesulfonate) brushes, Figure 5.2.3. Tapping mode height images collected alongside these EFM micrographs revealed that the polyelectrolyte brush layer had selectively retracted in response to the application of a +150 V probe tip potential, yielding a depressed region directly beneath the SPM probe tip (diameter approximately 250 nm and a maximum depth of 27 nm) whereas no topographical changes were observed following the application of -150 V to the probe tip. To ensure height images were not affected by residual charge on the SPM probe tip, identical height images were also gathered using a grounded probe operating in conventional tapping mode.

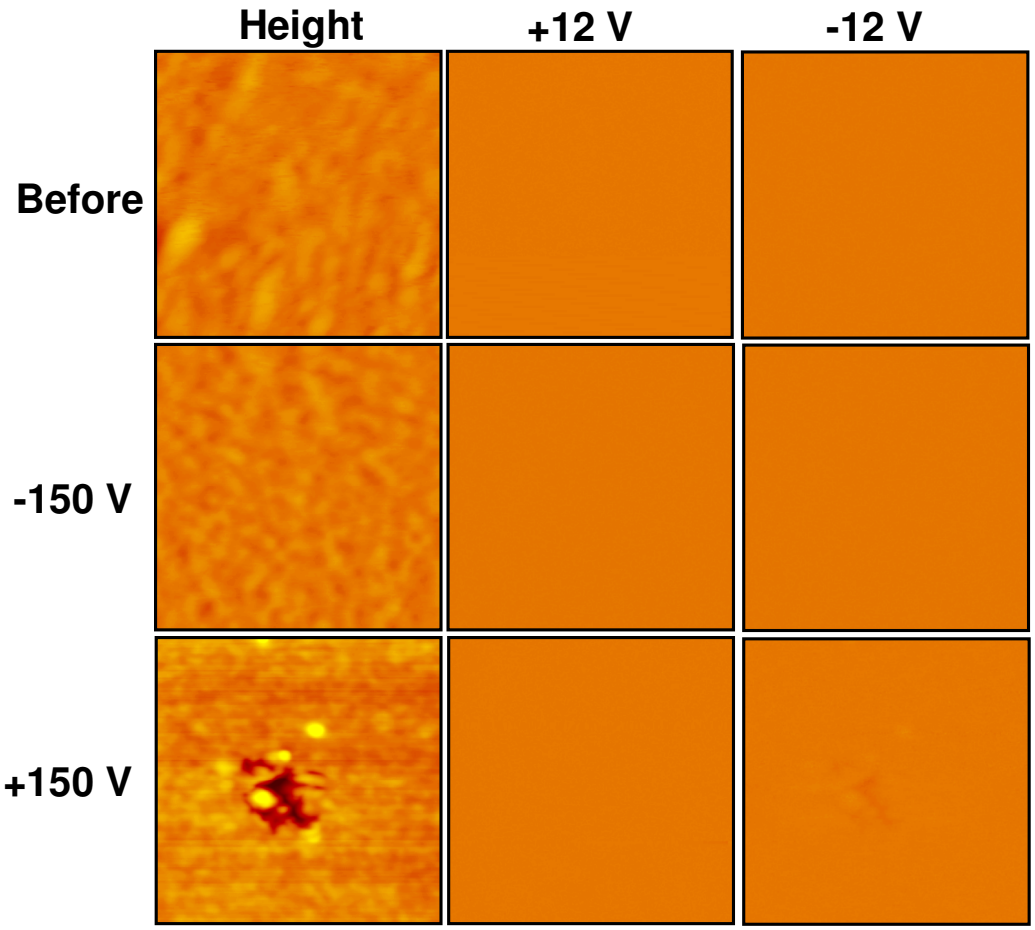

Figure 5.2.3: 1 µm x 1 µm AFM height images and EFM micrographs of anionic poly(sodium 4-styrenesulfonate) prior to, and following, the application of ±150 V to the SPM probe tip held 30 nm above the surface. EFM images were acquired immediately afterwards using an imaging bias voltage of ±12 V and a probe tip-to-sample separation of 100 nm. Z scale is 50 nm for height images and 15° for EFM lift mode phase images.

Similarly, cationic poly((2-methylacryloyloxy)ethyl trimethyl ammonium chloride) brush layers were found to collapse following the application of -150 V to the SPM probe tip, yielding a line-of-sight depression (diameter approximately 520 nm, maximum depth 24 nm), whereas no topographical changes were noted following +150 V application, Figure 5.2.4. Featureless EFM micrographs once again discounted the possibility of any charge retention by the polyelectrolyte brush layers.

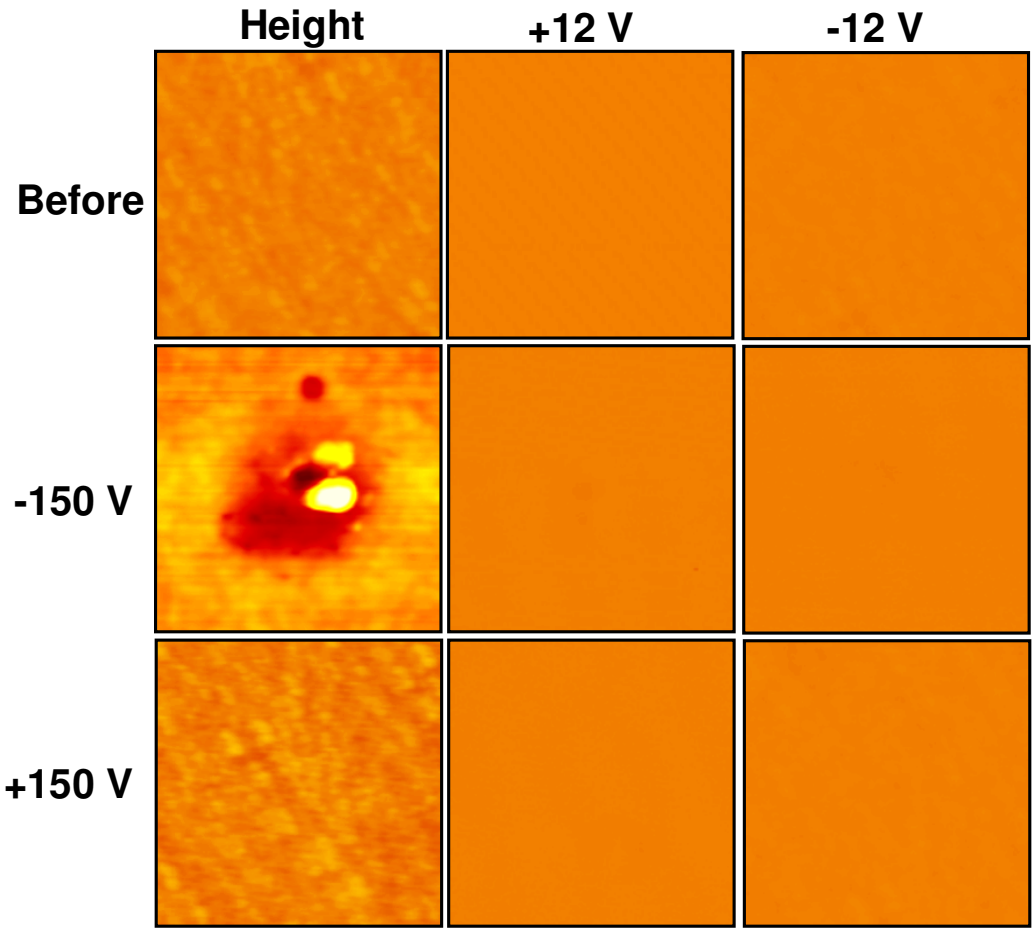

Figure 5.2.4: 1 µm x 1 µm AFM height images and EFM micrographs of cationic poly((2-methylacryloyloxy)ethyl trimethyl ammonium chloride) prior to and following the application of ±150 V to the SPM probe tip held 30 nm above the surface. EFM images were acquired immediately afterwards using 100 nm probe tip-to-sample separation with ±12 V applied to the probe tip. Z scale is 50 nm for height images and 15° for EFM lift mode phase images.

In the case of zwitterionic poly(*N,N*-dimethyl-*N*-(3-methacrylamido)-*N*-(3-sulfopropyl) ammonium betaine) brush layers, the application of both positive and negative bias voltage (±150 V) to the SPM probe tip resulted in localised *swelling* of the brush layer, (corresponding to maximum swelling diameters/heights of 600 nm/43 nm and 1350 nm/93 nm for –150 V and +150 V respectively), Figure 5.2.5. EFM micrographs taken of the more swollen regions for the +150 V applied tip potential revealed an inversion of phase images, indicating some positive charge retention by the zwitterionic polymer

brushes in this case, whereas those taken of swollen regions following the application of -150 V display responses to the feature height.

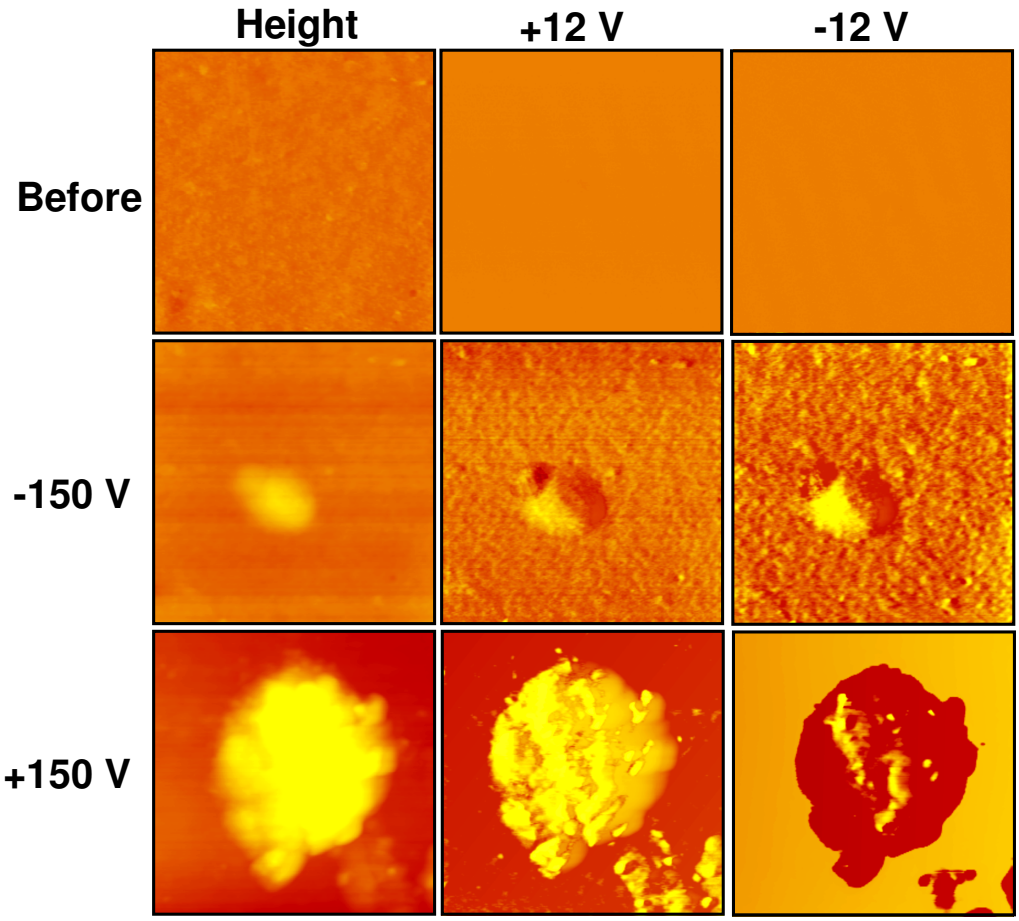

Figure 5.2.5: 2 µm x 2 µm AFM height images and EFM micrographs of zwitterionic poly(*N,N*-dimethyl-*N*-(3-methacrylamido)-*N*-(3-sulfopropyl) ammonium betaine) brushes prior to and following the application of ±150 V to the SPM probe tip held 30 nm above the surface. EFM images were acquired immediately afterwards using 100 nm probe tip-to-sample separation with ±12 V applied to the SPM probe tip. Z scale is 200 nm for height images and 15° for EFM lift mode phase images.

5.2.4 DISCUSSION

Responsive polyelectrolyte brushes comprise an important class of nanoactuator, although their application is limited by the nature of stimuli ordinarily used, e.g., variation of the ionic strength or pH of a contacting solution.[23] Besides the drawback of sequential immersion in solution (or alternately changing the composition of a contacting solution), this approach is only capable of producing a response over the entirety of a brush layer and cannot readily be localised. In the case of strong polyelectrolyte brushes, (such as those examined in the present study) collapse is ordinarily triggered by increasing the ionic strength of a contacting solution beyond a threshold value, whereupon the osmotic pressure from condensed counter-ions within the brush layer is counter-balanced.[37] In contrast, the present study demonstrates that swelling and collapse of such brushes can be laterally confined to sub-micron regions by the application of potential to a nearby SPM probe, where a further significant advantage is found in the electrically controlled nature of the stimulus.

As discussed in the preceding part of this chapter (Section 5.1.4), the application of high bias voltage to a sharp SPM probe results in the localised breakdown of air, leading to corona discharge.[31,32,33] Whilst macroscopic corona charging has previously been demonstrated to produce topographical changes on polymer surfaces, this has consistently been attributed to non-selective mechanisms such as chain scission,[38] oxidation,[39] or heating.[40] It was demonstrated in Chapter 5.1 that non-ionic, spin-coated polymer thin films exhibit no surface deformation after exposure to corona discharge from an SPM probe tip under identical conditions, discounting these mechanisms as an explanation for the observed results. Moreover, the observed polarity-dependence of polyelectrolyte retraction supports an alternative mode of action.

Control experiments for poly(methyl methacrylate) brushes grafted by ATRP onto pulsed plasma deposited poly(vinylbenzyl chloride) revealed that surface charge retention occurred for applied SPM probe tip bias voltages exceeding +35 V and -90 V for a polymer brush thickness of 28 nm. No change in polymer topography was noted for the poly(methyl methacrylate) brushes, thus indicating that the swelling or collapse of polyelectrolyte

brushes occurs as a consequence of their ionic nature. This follows reported topographical changes for spin-coated poly(sodium 4-styrenesulfonate) in response to contact-mode SPM charging, whilst non-ionic polymers investigated remained featureless following charge writing.[34]

In Chapter 5.1 the efficacy of SPM corona charging was shown to be governed by charge dissipation by adsorbed water. It follows that no charge retention is to be expected for poly(vinylbenzyl chloride) films decorated with polyelectrolyte brushes. Strong polyelectrolytes, particularly those containing quaternary ammonium or sulfonate groups, are known to be extremely hygroscopic.[16] Water has been identified within nominally dry poly(sodium 4-styrenesulfonate) brushes using FTIR,[41] and some reports estimate water content exceeding 80 % within 'blown dry' poly((2-methylacryloyloxy)ethyl trimethyl ammonium chloride) brushes under ambient humidity.[42] Indeed, no surface charge was detected by EFM immediately after SPM corona discharge for these polyelectrolyte brushes. The ionic nature of these brush layers can, however, allow the transportation of corona ions to the underlying poly(vinylbenzyl chloride), leading to a temporary build up of charge at the interface. Evidence for ionic mobility within polyelectrolyte hydrogels is found in their reported bending under an electric field,[10,20,21] and ion conduction is also required for the application of polyelectrolyte films in humidity sensors and capacitators.[43,44] Thus, the conveyance of corona ions through the polyelectrolyte brush layer towards the counter electrode (the metal sample holder disc) under applied electric field is feasible. In contrast, static charge is detectable on as-deposited poly(vinylbenzyl chloride) film surfaces following the application of +30 V and -80 V to the SPM probe tip, thereby demonstrating that pulsed plasma deposited poly(vinylbenzyl chloride) is not amenable to ionic mobility. Consequently, ions are expected to build up at the polyelectrolyte brush - pulsed plasma deposited poly(vinylbenzyl chloride) interface during bias voltage application.

Retraction of poly(sodium 4-styrenesulfonate) brushes occurred selectively in response to positive corona charging. This is explained by a localised build-up of positive corona ions at the interface with poly(vinylbenzyl chloride) during bias voltage application, followed by electrostatic attraction of anionic chain segments towards this region. The same argument can be

made for the selective retraction of poly((2-methylacryloyloxy)ethyl trimethyl ammonium chloride) towards negative corona charging. A recent report of poly(2-(dimethylamino)ethyl methacrylate) brush swelling in response to electric fields provides corroboration for this mechanism.[24] For the weakly polybasic brush layers examined therein, the degree of swelling observed under aqueous conditions in response to positively biased substrates exceeded that achievable by pH variation or counter-ion migration, leading the authors to conclude that electrostatic repulsion of the polymer segments away from the substrate was responsible.[24] In addition, polymer brush de-swelling towards the substrate was described upon application of negative bias, although this was found to be within experimental error.[24] The timeframes predicted for polyelectrolyte swelling/collapse by electric fields in this manner have been calculated as being in the order of 10^{-8} s.[25] By comparison, it has been reported that charged regions on polystyrene thin films (injected using contact-mode SPM charge writing) decreased by only 80 % upon 20 s immersion in water.[29] Therefore, given the high water content of polyelectrolyte brushes under ambient conditions, it is reasonable to conclude that in the present study, charge is retained at the poly(vinylbenzyl chloride)-polyelectrolyte brush interface for a sufficient period to induce polyelectrolyte brush movement, but dissipates prior to detection by electric force microscopy. Furthermore, polymer relaxation under ambient conditions is slow in comparison to the aforementioned timeframes for brush swelling or collapse and charge dissipation. For example, compressed polyelectrolyte multilayer films have been reported to show no recovery for several months during storage under dry conditions.[45] Because the time period required to capture EFM micrographs is approximately three minutes, the microscopy images reported herein display the actuated polymers prior to relaxation, but after the dissipation of detectable surface charge.

A recent report has demonstrated that for hydrated polyelectrolyte brushes, collapse results in the expulsion of water.[46] Furthermore, cationic poly((2-methylacryloyloxy)ethyl trimethyl ammonium chloride) brushes were found to incorporate higher water content than anionic sulfonated polyelectrolytes, and their collapse therefore led to the highest volume of ejected water.[46] In the present case of localised polyelectrolyte retraction,

water is expected to be squeezed out of the partially swollen brushes upon collapse, and forced towards the periphery of the retracted region. This is supported by swelling observed at the perimeter of the retracted region for cationic poly((2-methylacryloyloxy)ethyl trimethyl ammonium chloride) following the application of -150 V to the probe tip, Figure 5.2.4.

Polyelectrolyte brush swelling was not observed in response to repulsive electrostatic interactions following corona charging. This is attributed to high entropic resistance towards further swelling for densely-grafted polymer brushes (whereas polymer brush compression is entropically favourable[47]). Since conventional water vapour induced swelling of polyelectrolyte brushes is reported to become restricted with increasing grafting density (due to the pre-existence of steric stretching)[18], it is unsurprising that in the present study swelling is not observed for densely grafted polyelectrolyte brushes under ambient conditions.

In contrast to the polyelectrolyte brushes examined, however, swelling was observed for both positive and negative corona discharge exposure of zwitterionic poly(*N,N*-dimethyl-*N*-(3-methacrylamido)-*N*-(3-sulfopropyl) ammonium betaine) brushes. This is because zwitterionic brushes are well-known to exhibit *anti-polyelectrolyte* behaviour in solution, where brushes exist in a collapsed state due to intramolecular electrostatic attraction between anionic and cationic units.[48,49] In this case, brush layers are expected to exist in a collapsed conformation when removed from solution, so that stretching is more entropically favourable. A degree of swelling was therefore observed upon bias voltage application to the SPM probe tip, and this is explained by electrostatic repulsion of the polymeric sub-units carrying the same charge as the corona-generated ions which build up at the interface with poly(vinylbenzyl chloride) during electric field application. The detection of surface charge on poly(*N,N*-dimethyl-*N*-(3-methacrylamido)-*N*-(3-sulfopropyl) ammonium betaine) brushes following only positive bias application to the SPM probe tip is in line with the comparatively lower degree of absorbed water predicted to exist within the collapsed brushes, (free polymers containing sulfobetaine moieties are frequently insoluble in water[50]), and the enhanced efficacy of positive corona discharge formation in comparison to negative corona discharge, as discussed in Section 5.1.4.

5.2.5 CONCLUSIONS

A complex responsive behaviour has been reported for ATRP grafted polyelectrolyte and polyzwitterionic brushes, where corona discharge from an SPM probe tip is used as the stimulus. Localised swelling and retraction of polymer brushes was observed, where the nature of the response is dependent on the ionic constituents within the brush and the polarity of the bias voltage applied to the probe tip.

5.2.6 REFERENCES

(1) Calvo, A.; Yameen, B.; Williams, F. J.; Azzaroni, O.; Soler-Illia, G. J. A. A. *Chem. Commun.* **2009**, 2553.

(2) Zhang, Z.; Vaisocherová, H.; Cheng, G.; Yang, W.; Xue, H.; Jiang, S. *Biomacromolecules* **2008**, *9,* 2686.

(3) Malay, Ö.; Batıgün, A.; Bayraktar, O. *Int. J. Pharm.* **2009**, *380*, 120.

(4) Ryan, A. J.; Crook, C. J.; Howse, J. R.; Topham, P.; Jones, R. A. L.; Geoghegan, M.; Parnell, A. J.; Ruiz-Pérez, L.; Martin, S. J.; Cadby, A.; Menelle, A.; Webster, J. R. P.; Gleeson, A. J.; Bras, W. *Faraday Discuss.* **2005**, *128*, 55.

(5) Golas, P. L.; Louie, S.; Lowry, G. V.; Matyjaszewski, K.; Tilton, R. D. *Langmuir* **2010**, *26*, 16890.

(6) Fulghum, T. M.; Estillore, N. C.; Vo, C.-D.; Armes, S. P.; Advincula, R. C. *Macromolecules* **2008**, *41,* 429.

(7) Lego, B.; Skene, W. G.; Giasson, S. *Macromolecules* **2010**, *43*, 4384.

(8) Sua, P.-G.; Tseng, J.-Y.; Huanga, Y.-C.; Pan H.-H.; Li, P.-C. *Sens. Act. B*, **2009**, *137*, 496.

(9) Sakai, Y.; Sadaoka, Y.; Matsuguchi, M.; Rao, V. L.; Kamigaki, M. *Polymer* **1989**, *30*, 1068.

(10) Osada, Y.; Okuzaki, H.; Hori, H. *Nature* **1992**, *355*, 242.

(11) Sankhe, A. Y.; Husson, S. M.; Kilbey, S. M. *J. Polym. Sci. A* **2007**, *45*, 566.

(12) Kong, H.; Luo, P.; Gao, C.; Yan D. *Polymer* **2005**, *46*, 2472.

(13) Tugulu, S.; Barbey, R.; Harms, M.; Fricke, M.; Volkmer, D.; Rossi, A.; Klok, H.-A. *Macromolecules* **2007**, *40,* 168.

(14) Ayres, N.; Boyes, S. G.; Brittain, W. J. *Langmuir* **2007**, *23,* 182.

(15) Sanjuan, S.; Perrin, P.; Pantoustier, N.; Tran, Y. *Langmuir* **2007**, *23,* 5769.

(16) Sakai, Y. *Sens. Actuators, B* **1993***, 13-14,* 82.

(17) Thijs, H. M. L.; Becer, C. R.; Guerrero-Sanchez, C.; Fournier, D.; Hoogenboom, R.; Schubert, U. S. *J. Mater. Chem.* **2007**, *17*, 4864.

(18) Biesalski, M.; Rühe, J. *Langmuir* **2000**, *16,* 1943.

(19) Kim M.-J.; Gong, M.-S. *Analyst* **2012**, *137*, 1487.

(20) Kaltbeitzel, A.; Schauff, S.; Steininger, H.; Bingöl, B.; Brunklaus G.; Meyer, W. H.; Spiess, H. W. *Solid State Ionics* **2007**, *178*, 469.

(21) Lin, J.; Tang, Q.; Hu, D.; Sun, X.; Li, Q.; Wu, J. *Colloids Surf., A* **2009**, *346*, 177.

(22) Asaka, K.; Oguro, K. *J. Electroanalytical Chem.* **2000**, *480*, 186.

(23) Ballauff, M.; Borisov, O. *Curr. Opin. Colloid Interface Sci.* **2006**, *11*, 316.

(24) Weir, M. P.; Heriot, S. Y.; Martin, S. J.; Parnell, A. J.; Holt, S. A.; Webster, J. R. P.; Jones, R. A. L. *Langmuir* **2011**, *27*, 11000.

(25) Ouyang, H.; Xia, Z.; Zhe, J. *Nanotechnology* **2009**, *20***,** 195703.

(26) Migliorini, G. *Macromolecules* **2010**, *43*, 9168.

(27) Knorr, N.; Rosselli, S.; Nelles, G. *J. Appl. Phys*. **2010**, *107*, 054106.

(28) Reagan, M. A.; Kashyn, D.; Juhl, S.; Vaia, R. A.; Lyuksyutov, S. F. *Appl. Phys. Lett.* **2008**, *93*, 033109.

(29) Blanco, E. M.; Horton, M. A.; Mesquida, P. *Langmuir* **2008**, *24*, 2284.

(30) Xie, X. N.; Chung, H. J.; Sow, C. H.; Adamiak, K.; Wee, A. T. S. *J. Am. Chem. Soc.* **2005**, *127*, 15562.

(31) Stern, J. E.; Terris, B. D.; Mamin, H. J.; Rugar, D. *Appl. Phys. Lett.* **1988**, *53,* 2717.

(32) Schönenberger, C. *Phys. Rev. B* **1992**, *45*, 3861.

(33) Schönenberger, C.; Alvarado, S. F. *Phys. Rev. Lett.* **1990**, *65*, 3162.

(34) Knorr, N.; Rosselli, S.; Miteva, T.; Nelles, G. *J. Appl. Phys.* **2009**, *105*, 114111.

(35) Lin-Vien, D.; Colthrup, N. B.; Fateley, W. G.; Grasselli, J. G. *The Handbook of Infrared and Raman Characteristic Frequencies of Organic Molecules*; Academic Press: Boston, 1991.

(36) Iddon, P. D.; Robinson, K. L.; Armes, S. P. *Polymer* **2004**, *45*, 759.

(37) Guo, X.; Ballauff, M. *Phys. Rev. E* **2001**, *64*, 051406.

(38) Boyd, R. D.; Kenwright, A. M.; Badyal, J. P. S.; Briggs, D. *Macromolecules* **1997**, *30,* 5429.

(39) Földes, E.; Tóth, A.; Kálmán, E.; Fekete, E.; Tomasovszky-Bobák, A. *J. Appl. Polym. Sci*. **2000**, *76*, 1529.

(40) Foerch, R.; Izawa, J.; Spears, G. *J. Adhes. Sci. Technol.* **1991**, *5*, 549.

(41) Kong, H.; Luo, P.; Gao, C.; Yan, D. *Polymer* **2005**, *46*, 2472.

(42) Dunlop, I. E.; Thomas, R. K.; Titmus, S.; Osborne, V.; Edmondson, S.; Huck, W. T. S.; Klein, J. *Langmuir* **2012**, *28*, 3187.

(43) Wee, G.; Larsson, O.; Srinivasan, M.; Berggren, M.; Crispin, X.; Mhaisalkar, S. *Adv. Funct. Mater.* **2010**, *20*, 4344.

(44) Lee, C.-W.; Joo, S.-W.; Gong, M.-S. *Sens. Actuators, B* **2005**, *105*, 150.

(45) Ladhari, N.; Hemmerlé, J.; Haikel, Y.; Voegel, J.-C.; Schaaf, P.; Ball, V. *Appl. Surf. Sci.* **2008**, *255*, 1988.

(46) Ramos, J. J. I.; Moya, S. E. *Macromol. Rapid Commun.* **2011**, *32,* 1972.

(47) Tranchida, D.; Sperotto, E.; Chateauminois, A.; Schönherr, H. *Macromolecules* **2011**, *44*, 368.

(48) Zhang, Z.; Chao, T.; Jiang, S. *J. Phys. Chem. B* **2008**, *112,* 5327

(49) Zhao, Y.-H.; Wee, K.-H.; Bai, R. *ACS Appl. Mater. Interfaces* **2010**, *2*, 203.

(50) Umar, Y.; Abu-Sharkh, B. F.; Ali, Sk. A. *Polymer* **2005**, *46*, 10709.

CHAPTER 6

CONCLUSIONS

6. CONCLUSIONS

Tailored surface functionality is of key importance for development in fields such as smart surfaces, microfluidics, data storage, fuel cells and biotechnology. In this thesis, the plasmachemical deposition of nanofilms has been successfully combined with controlled living polymerization (ATRP) to produce polymer brush decorated surfaces. Using this methodology the substrate-independent nature of plasmachemical deposition is effectively coupled with the precise control over chain length (and therefore surface functionality) associated with ATRP.

By using controlled polymerization, the macromolecular architecture of polymer brushes can be manipulated to further enhance surface functionality. This was demonstrated using graft copolymer layers constructed by sequential ATRP from pulsed plasma deposited poly(vinylbenzyl chloride) nanofilms. These were found to yield enhanced surface lubricity as a direct result of their bottle-brush structure.

A second approach to surface modification is found in the lateral positioning of polymer brushes to generate multifunctional surfaces. The fabrication of nanopatterned surfaces was achieved using localised ATRP grafting onto initiator sites patterned using the 'molecular scratchcard' technique. This entailed plasmachemical bilayering to produce a stack comprising 100 nm poly(vinylbenzyl chloride) covered by a 20 nm poly(*N*-acryloylsarcosine methyl ester) barrier film. ATRP initiating sites were then selectively exposed using an AFM probe tip to remove the inert overlayer. Three dimensional polymeric nanostructures were assembled by ATRP grafting from these sites.

Patterned poly(methyl methacrylate) and poly(glycidyl methacrylate) nanostructures were found to be actuated by selective solvent exposure. Lateral spreading of the polymer structures was induced by exposure to poor solvent and effectively provides the means to selectively cover and unveil the underlying surface. Such lateral spreading may be useful for the fabrication of nanomachines and microfluidic valves, where further embodiments can be envisaged to include thermo- or pH-responsive polymer brushes. Furthermore, the solvent responsive nature of ATRP grafted poly(glycidyl methacrylate) brushes was exploited to actuate pore size within macroporous

scaffolds. These scaffolds were assembled by exposure of pulsed plasma deposited poly(vinylbenzyl chloride) to amphiphilic species, followed by spontaneous emulsion formation at elevated temperatures. The demonstrated ability of pulsed plasma deposited poly(vinylbenzyl chloride) to form open cell macroporous structures provides a further advantage for its use as a versatile ATRP initiator layer.

In the case of ATRP grafted polyelectrolyte brushes, swelling or retraction was triggered by exposure to corona discharge emanating from a metallised AFM probe. This corona charging approach was also shown to generate regions of static charge in conventional spin coated polymer films and comprises a novel method for charge writing.

CHAPTER 7

SUGGESTIONS FOR FUTURE WORK

7. SUGGESTIONS FOR FUTURE WORK

The work outlined in this thesis demonstrates that plasmachemical deposition can be coupled to atom transfer radical polymerization to provide a substrate-independent methodology for polymer brush grafting. Organic phase ATRP from pulsed plasma deposited poly(vinylbenzyl chloride) was found to proceed at a greater rate, and yield thicker brush layers than comparable reactions reported for ATRP from self-assembled monolayers. Further investigations into the efficacy of pulsed plasma deposited poly(vinylbenzyl chloride) layers for ATRP could involve in-situ monitoring of polymerization using AFM, ellipsometry or QCM to evaluate whether substrate swelling yields initiation from within the layer.

Sequential surface-initiated ATRP was utilised for the generation of lubricating bottle-brush co-polymer films. Future experiments in this area could include further clarification of the frictional response for these brush layers by e.g., measuring macroscale lubrication with a conventional pin-on-disk or sliding ball tribometer, or else using a surface force balance to precisely measure symmetrical friction responses between two brush layers grafted onto a well-defined substrate such as mica. The substrate-independent nature of plasma deposition may also be exploited to generate ATRP initiator layers on soft substrates such as hydrogels and porous scaffolds for further improvements in lubrication.

The ‘molecular scratchcard’ lithography technique was used to pattern ATRP-initiating poly(vinylbenzyl chloride) regions against a functional resist background, followed by amplification of the generated pattern by ATRP grafting of poly(methyl methacrylate) brushes. Future optimisation of this lithography method should involve quantification of normal forces applied to the SPM probe when puncturing the resist layer, and its relationship to the generated scratch depth. This could potentially allow a tri-layered plasmachemical stack to be pierced to varying depths in order to pattern more complex regions of differing functionalities. Furthermore, an extension of the ATRP grafting technique can be envisaged involving capping active polymer brush ends using sodium azide and a second scratching/ATRP step to produce surfaces patterned with multiple three-dimensional polymer brush functionalities. It may also be of interest to experiment with alternative resist

layers to elucidate the effect on the apparent enhanced ATRP rate, and the subsequent lateral spreading of the brushes upon exposure to solvents.

Macroporous structures were generated from pulsed plasma deposited poly(vinylbenzyl chloride) by seeding the polymer film with amphiphilic species, followed by spontaneous emulsion formation in de-ionised water at 60 °C. Further experiments to clarify the mechanism of this phenomenon could include investigations into the effect of surfactant structure and its concentration upon pore dimensions, the effects of added salts within the aqueous phase (increasing its density), or else varying the degree of cross-linking within the poly(vinylbenzyl chloride) film by e.g., varying plasma deposition parameters, annealing, or argon plasma treatment (this should lower the flexibility of the film and hence retard pore formation). Future work could also include extension of the technique to alternative plasma deposited films, most obviously poly(styrene) which is predicted to behave in a similar manner with higher temperatures required to induce pore formation (as a consequence of its higher Tg). Further embodiments can also be envisaged using hydrophilic polymer films and emulsification with organic non-solvents.

Finally, the generation of corona discharge from a conducting SPM probe was shown to yield regions of localised surface charge on spin coated polymers. This technique may find further application in the precise positioning of proteins, carbon nanotubes or microspheres on surfaces, as has been demonstrated for contact-mode charge writing. The technique was applied in Chapter 5.2 to induce localised collapse or swelling of ATRP grafted polyelectrolyte brushes. Such a localised swelling/collapse response could be used in concert with macroporous poly(vinylbenzyl chloride) films to open/close individual pores grafted with polyelectrolyte brush layers, or else to create electrically stimulated valves within microfluidic devices, or even within nanofluidic channels constructed using e.g., the ‘molecular scratchcard’ technique.